





Universitat Autònoma de Barcelona

ADVERTIMENT. L'accés als continguts d'aquesta tesi queda condicionat a l'acceptació de les condicions d'ús establertes per la següent llicència Creative Commons:  http://cat.creativecommons.org/?page_id=184

ADVERTENCIA. El acceso a los contenidos de esta tesis queda condicionado a la aceptación de las condiciones de uso establecidas por la siguiente licencia Creative Commons:  <http://es.creativecommons.org/blog/licencias/>

WARNING. The access to the contents of this doctoral thesis it is limited to the acceptance of the use conditions set by the following Creative Commons license:  <https://creativecommons.org/licenses/?lang=en>

Controlling static magnetic fields with positive and negative permeability metamaterials

Ph.D. Thesis in Physics of
Rosa Mach Batlle

Directors

Dr. Nuria Del Valle Benedí

and

Dr. Jordi Prat Camps

Tutor

Dr. Gemma Garcia Alonso

Physics Department

Universitat Autònoma de Barcelona

Bellaterra, June 2019

*Per a en Dani,
els meus pares i el meu germà.*

Agraïments

Escric aquestes paraules contenta per estar arribant al final d'una etapa plena de reptes científics i personals. En aquest espai, intentaré donar les gràcies a totes les persones que m'han acompanyat i guiat durant aquests dos anys i mig.

M'agradaria començar agraint a en Dani tot el suport i els ànims que m'ha donat des que ens vam conèixer. Li vull donar les gràcies per animar-me a escollir la carrera de física i per donar-me la força i la confiança que necessitava per començar el doctorat. Gràcies per la paciència i la calma que m'ha transmès totes les vegades que hem assajat classes i presentacions, i per escoltar-me sempre que li volia explicar els meus petits avenços científics. El record del dia que em va acompanyar a fer la meva primera classe és un dels més bonics que tinc com a estudiant de doctorat. Em fa molt feliç haver perdut la por de parlar en públic al seu costat. La seva positivitat, valentia, amor i comprensió han estat essencials per a mi, sobretot durant l'últim any de la tesi.

Seguidament, voldria donar les gràcies a les persones de la UAB amb qui he compartit aquesta etapa. Em sento molt afortunada d'haver pogut acabar la tesi amb uns directors excel·lents, la Nuria i en Jordi. Els vull donar les gràcies per la seva dedicació en la tesi i per totes les discussions científiques, però sobretot per la seva guia més personal. Moltes gràcies per animar-me i ajudar-me a recuperar la confiança en mi mateixa i la il·lusió per dedicar-me a la recerca. També agraeixo molt sincerament tota l'ajuda de la meva tutora, la Gemma, que m'ha animat a seguir amb el doctorat. El suport dels meus companys de despatx, l'Albert, en Sergi, en Josep i en Leo, ha estat molt important per a mi. Moltes gràcies per totes les converses, els dinars, les bromes, OT, els dies al SAF... Espero que puguem conservar l'amistat que hem format aquests anys. També vull donar les gràcies al Carles per les discussions científiques i als companys de departament d'electromagnetisme Joan, Fernando i Jordi, ja que ha estat un plaer compartir amb ells les meves primeres classes com a professora. El suport proporcionat per l'observatori per a la igualtat de la UAB ha estat també clau per la finalització d'aquesta tesi. Moltes gràcies pel seu suport a l'Arantxa, la Laura, l'Alex i en Jordi.

Finalment, agraeixo a la meva família i veïns de Tapis tota la força i l'alegria que em transmeten. El suport dels meus pares i germà, així com el dels pares d'en Dani, ha estat especialment important per a mi al final de la tesi. També agraeixo molt sincerament el suport dels meus amics i amigues de Maçanet de Cabrenys, de la Jonquera i de la carrera. Les converses amb la Nerea, l'Aida, l'Anna, la Valeria, en Sergi i en Roger m'han animat i ajudat molt. Moltes gràcies també a totes aquelles persones que no anomeno però que han format part d'aquesta experiència i han posat el seu granet de sorra per fer-me créixer.

Rosa Mach Batlle
Bellaterra, març del 2019.

Magnetism, arising from electric currents and magnetic moments of elementary particles, is a physical phenomenon present in our day-to-day life. The Earth magnetic field, for example, is crucial for our survival, since it protects the planet and its organisms from the charged particles of the solar wind and cosmic rays. In the last couple of centuries, the scientific and technological advances in controlling magnetic fields have ignited the development of a wide range of technologies based on magnetism, including turbines, transformers, data storage systems, biomedical equipment and sensors. In this context, research on how to manipulate magnetic fields is not only essential for improving a wide range of current technologies but also because it could lead to new applications of magnetism.

Magnetic fields are shaped and controlled by magnetic materials. The way each material responds to an applied magnetic field depends on its magnetic permeability. Traditionally, most of the devices for controlling magnetic fields included ferromagnetic materials, which strongly attract magnetic fields due to their extremely large permeability. In the last decade, the design of magnetic metamaterials exhibiting unconventional properties has widened the toolbox for controlling magnetic fields, enabling the development of intriguing devices such as invisibility magnetic cloaks that can make objects magnetically undetectable, or magnetic hoses that can transfer and route magnetic fields. These metamaterials consist of arrangements of natural materials, typically combinations of ferromagnets and their antagonistic material, perfect diamagnets, which strongly expel the magnetic field due to their extremely low permeability.

In this thesis, we present different strategies for controlling static magnetic fields. We start by deriving some general features of conventional materials with extreme permeability, continue by designing and deriving the properties of novel devices based on magnetic metamaterials and, finally, introduce the concept of negative static permeability. Similar to negative indexes of refraction, which have enabled effects such as perfect lensing, negative static permeability is shown to bring new possibilities for shaping static magnetic fields. The content of the thesis is organized as follows.

Chapter 1 is an introduction to some concepts on electromagnetism that will be used throughout this work. We start by briefly reviewing the Maxwell equations, giving special attention to the limit of static magnetic fields and the magnetic boundary conditions. Then, we present transformation optics, a mathematical technique that has enabled the design of several novel devices for controlling electromagnetic fields, and metamaterials, artificial structures exhibiting the unconventional permittivity and permeability tensors required for developing most of the devices derived from the transformation optics theory. Finally, we describe some properties of the most common types of magnetic materials: diamagnetic, paramagnetic, and ferromagnetic materials.

In Chapter 2, we study in detail how materials with extremely low and extremely large linear, homogeneous, and isotropic magnetic permeability interact with static magnetic fields. These results are directly derived from Maxwell equations and magnetic boundary conditions and, thus, can be applied to different geometries. With this study, we do not only recover some well-known properties of both perfect diamagnetic ($\mu \rightarrow 0$) and ideal ferromagnetic ($\mu \rightarrow \infty$) materials, such as their ability to shield magnetic fields, but also demonstrate some unexploited features of perfect diamagnetic materials enclosing free current densities.

In Chapter 3, we present different strategies for shaping magnetic fields with magnetic metamaterials. To start with, we apply transformation optics and Maxwell equations to derive the properties of two-dimensional shells with arbitrary cross-section and three-dimensional spherical shells able to concentrate magnetic fields inside their holes. Then, we study which is the effect of covering magnetic materials with these concentrators and demonstrate that their magnetic response is magnified in such a way that the material appears as an enlarged material. As a possible application of these ideas, our concentrators could help improve current sensing techniques. We show that the concentrators could enhance the sensitivity of a sensor at the cost of increasing its detectability, which may benefit some applications, but may be an issue when non-invasive sensing is required. Lastly, we present a different metamaterial device that, opposite to the concentrating shells, can make magnetic sensors magnetically undetectable at the cost of reducing their sensitivity.

In Chapter 4, we introduce the concept of negative permeability in magnetostatics. Even though negative values of the permeability have not been found in naturally occurring materials, we theoretically and experimentally demonstrate that their properties can be effectively emulated in practice by arrangements of currents. Two devices requiring negative values of the permeability are presented to illustrate the potential of negative-permeability materials. First, we demonstrate the possibility of transforming the magnetic signature of an object into that of a different one (magnetic illusion). Second, we present the analogy of a perfect lens for the case of static magnetic fields, which could eventually lead to the emulation and cancellation of magnetic sources remotely.

The global conclusions of the thesis are presented in Chapter 5. Finally, additional analytic derivations are included as an Appendix.

1	Introduction to essential concepts	5
1.1	Maxwell equations	5
1.1.1	Static magnetic regime	6
1.1.2	Magnetic boundary conditions	7
1.2	Transformation optics and metamaterials	8
1.2.1	Transformation optics	8
1.2.2	Metamaterials	9
1.3	Magnetic materials	10
2	Shaping magnetic fields with extreme permeabilities	13
2.1	Shielding externally applied magnetic fields	14
2.1.1	Perfect diamagnetic materials	15
2.1.2	Ferromagnetic materials	16
2.2	Enclosing magnetic field sources	17
2.2.1	Shielding irrotational fields	17
2.2.2	Enclosing free currents with zero-permeability media	19
2.2.3	Wire superposition with zero-permeability media	22
2.2.4	Enclosing free currents with infinite-permeability media	24
2.2.5	Analogy between perfect diamagnets and electric conductors	24
2.3	Chapter summary and conclusions	25
3	Shaping magnetic fields with positive-permeability metamaterials	27
3.1	Magnetic field concentration	28
3.1.1	Long concentrators with arbitrary geometry	29
3.1.2	Spherical concentrators	32
3.1.3	Realizing magnetic concentrators with metamaterials	35
3.2	Magnifying magnetic materials	38

3.2.1	Magnetic field expulsion	38
3.2.2	Surrounding magnetic materials by magnetic concentrators . . .	41
3.2.3	Surrounding short magnetic materials by short concentrators . .	43
3.2.4	Realizing magnification shells with metamaterials	46
3.3	Cloaking shells to make magnetic sensors undetectable	48
3.3.1	Cloaking spherical sensors in uniform fields	49
3.3.2	Generalization to non-spherical sensors and inhomogeneous fields	52
3.3.3	Realizing the cloaking shell with metamaterials	54
3.4	Chapter summary and conclusions	55
4	Shaping magnetic fields with negative permeability	57
4.1	Static negative permeability	58
4.1.1	Ellipsoids with negative permeability	58
4.1.2	Hollow ellipsoids with negative permeability	61
4.1.3	Negative-permeability emulation with active metamaterials . . .	66
4.1.4	Experimental realization of a negative-permeability material . . .	68
4.2	Illusion: disguising an object as another object	70
4.2.1	Derivation of illusion in magnetostatics	71
4.2.2	Emulating illusion devices with active metamaterials	74
4.2.3	Experimental realization of illusion in magnetostatics	76
4.3	Perfect magnetic lenses: emulating sources remotely	79
4.3.1	Derivation of a perfect magnetic lens with transformation optics	80
4.3.2	Study of perfect magnetic lenses with Maxwell equations	85
4.3.3	Creating and cancelling magnetic sources with perfect lenses . .	88
4.4	Chapter summary and conclusions	93
5	Conclusions	95
A	Uniqueness theorems in magnetostatics	97
A1	Magnetic scalar potential	97
A2	Magnetic vector potential	98
	Bibliography	101

Introduction to essential concepts

In this chapter, we build the theoretical framework of this thesis. We start with a review of Maxwell equations, pointing out the simplifications that will be made throughout this work for static magnetic fields. We continue with an introduction to the transformation optics technique and the concept of metamaterials. Finally, magnetic materials are introduced as a tool for controlling static magnetic fields.

1.1 Maxwell equations

Electromagnetic phenomena are governed by the four Maxwell equations [1, 2, 3],

$$\nabla \cdot \mathbf{D} = \rho_f, \quad (1.1)$$

$$\nabla \cdot \mathbf{B} = 0, \quad (1.2)$$

$$\nabla \times \mathbf{E} = -\frac{\partial \mathbf{B}}{\partial t}, \quad (1.3)$$

$$\nabla \times \mathbf{H} = \mathbf{J}_f + \frac{\partial \mathbf{D}}{\partial t}, \quad (1.4)$$

where \mathbf{D} is the displacement field, \mathbf{B} is the magnetic induction, \mathbf{E} is the electric field, \mathbf{H} is the magnetic field, ρ_f is the free charge density and \mathbf{J}_f is the free current density. The constitutive equations relate the fields \mathbf{D} and \mathbf{E} and the fields \mathbf{B} and \mathbf{H} . In absence of a dielectric or a magnetic material they can be written as $\mathbf{D} = \varepsilon_0 \mathbf{E}$ and $\mathbf{B} = \mu_0 \mathbf{H}$, where ε_0 and μ_0 are the vacuum permittivity and permeability, respectively. In the presence of a material, the constitutive equations become

$$\mathbf{D} = \varepsilon_0 \mathbf{E} + \mathbf{P} = \varepsilon \varepsilon_0 \mathbf{E}, \quad (1.5)$$

$$\mathbf{B} = \mu_0(\mathbf{H} + \mathbf{M}) = \mu\mu_0\mathbf{H}, \quad (1.6)$$

where \mathbf{P} is the electric polarization, \mathbf{M} is the magnetization, and ε and μ are the relative permittivity and permeability of the material, respectively. When a field is applied to a medium made up of a large number of atoms or molecules, each molecule creates a multipolar response, dominated by the dipolar term. The polarization and the magnetization give the distribution of electric and magnetic dipole moments per unit volume. By means of the constitutive relations, \mathbf{D} and \mathbf{H} can be eliminated from Eqs. (1.1) and (1.4), which become

$$\nabla \cdot \mathbf{E} = \frac{1}{\varepsilon_0}(\rho_f - \nabla \cdot \mathbf{P}), \quad (1.7)$$

$$\nabla \times \mathbf{B} = \mu_0(\mathbf{J}_f + \varepsilon_0 \frac{\partial \mathbf{E}}{\partial t} + \frac{\partial \mathbf{P}}{\partial t} + \nabla \times \mathbf{M}). \quad (1.8)$$

These equations indicate that electromagnetic materials in the presence of electromagnetic fields can be effectively emulated by an equivalent distribution of charge of density $-\nabla \cdot \mathbf{P}$, and an equivalent distribution of current of density $\partial \mathbf{P} / \partial t + \nabla \times \mathbf{M}$ [4].

1.1.1 Static magnetic regime

In static conditions, the time derivatives of the electromagnetic fields are zero and electric and magnetic fields decouple. Static magnetic fields are described by the two magnetostatic Maxwell equations,

$$\nabla \cdot \mathbf{B} = 0, \quad (1.9)$$

$$\nabla \times \mathbf{B} = \mu_0(\mathbf{J}_f + \nabla \times \mathbf{M}). \quad (1.10)$$

One of the most important consequences of these equations is that static magnetic fields always decay with the distance from the sources, which contrasts with the long-distance propagation of time-dependent electromagnetic waves. This example illustrates how different the physics behind the static case is from that of the electromagnetic waves case. Therefore, the physical results obtained in magnetostatics cannot always be derived as the zero-frequency limit of the results for the full-wave case and the study of static magnetic fields has a deep interest on its own.

Equation (1.10) shows that the magnetic induction due to a magnetized body is exactly the same as the one produced by a volume, \mathbf{J}_M , and a surface, \mathbf{K}_M , magnetization current densities

$$\mathbf{J}_M = \nabla \times \mathbf{M}, \quad (1.11)$$

$$\mathbf{K}_M = \mathbf{M} \times \mathbf{n}, \quad (1.12)$$

where \mathbf{n} is the unitary vector pointing outwards the material surface. This result is valid both for points at the interior and at the exterior of the magnetic material.

The magnetization of a magnetic material is related to the magnetic field through the constitutive equation (1.6). This equation involves the magnetic permeability, which is the tensor relating the magnetic field and the magnetic induction inside a material and may depend on the magnetic field magnitude and direction, and on the position in the material. When the material can be assumed linear, isotropic, and homogeneous the permeability becomes a constant scalar magnitude and Eq. (1.6) leads to

$$\mathbf{M} = (\mu - 1)\mathbf{H} = (\mu - 1)(\mathbf{H}_a + \mathbf{H}_d), \quad (1.13)$$

where \mathbf{H} is the field inside the material and can be regarded as the superposition of the applied magnetic field, \mathbf{H}_a , plus the demagnetizing field, $\mathbf{H}_d = -N\mathbf{M}$. The demagnetizing field strongly depends on the sample permeability and geometry through the demagnetizing factor N , which is, in general, a tensor [5].

1.1.2 Magnetic boundary conditions

When there is a boundary between two media of different electromagnetic nature, the fields must satisfy some boundary conditions in order to fulfill the four Maxwell equations in all space. In the case of static magnetic fields, the magnetic field and the magnetic induction must satisfy the magnetostatic boundary conditions,

$$\mathbf{n}_{12} \cdot (\mathbf{B}_2 - \mathbf{B}_1) = 0, \quad (1.14)$$

$$\mathbf{n}_{12} \times (\mathbf{H}_2 - \mathbf{H}_1) = \mathbf{K}_f, \quad (1.15)$$

which arise from the Maxwell equations (1.9) and (1.10) and the constitutive equation (1.6). The subscripts 1 and 2 refer to the mediums 1 and 2 in the interface, \mathbf{n}_{12} is a unit vector pointing from the medium 1 towards the medium 2, and \mathbf{K}_f is the free surface current density.

Equations (1.15) and (1.14) show that the component of the magnetic field tangential to the boundary between two media must be continuous unless there are free currents flowing on the interface and that the component of the magnetic induction perpendicular to the boundary between two media must always be continuous. Equation (1.10) gives the boundary condition for the tangential component of the magnetic induction. It depends on the free surface current density, \mathbf{K}_f , and on the magnetization surface current density, \mathbf{K}_M , as

$$\mathbf{n}_{12} \times (\mathbf{B}_2 - \mathbf{B}_1) = \mu_0(\mathbf{K}_f + \mathbf{K}_M), \quad (1.16)$$

where

$$\mathbf{K}_M = \mathbf{n}_{12} \times (\mathbf{M}_2 - \mathbf{M}_1). \quad (1.17)$$

Equation (1.17) reduces to Eq. (1.12) for the case of a material in vacuum, $\mathbf{M}_2 = 0$.

1.2 Transformation optics and metamaterials

Transformation optics is a mathematical technique that enables the design of novel devices to control and manipulate electromagnetic fields [6, 7, 8]. These devices usually require inhomogeneous and anisotropic permittivity and permeability tensors that are not found in naturally occurring materials. In consequence, the development of metamaterials with unconventional effective permittivity and permeability tensors has been crucial [9].

1.2.1 Transformation optics

Transformation optics provides a visual intuitive way of describing how electromagnetic fields interact with materials. Based on space transformations, this technique offers a recipe for controlling electromagnetic fields almost at will [6].

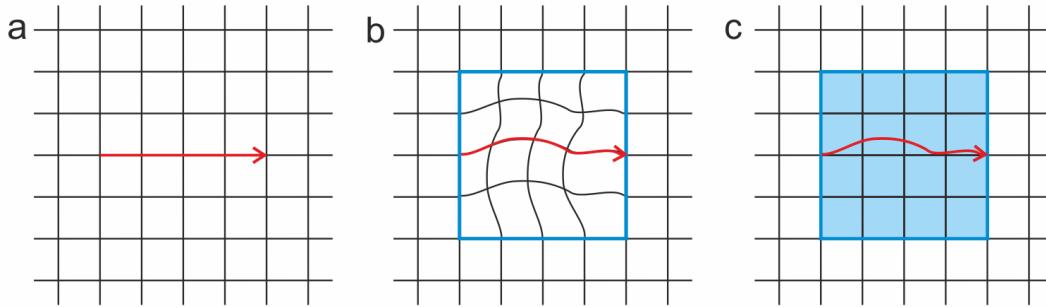


Figure 1.1: Sketch of the transformation optics technique. Field propagating in (a) an original cartesian space, (b) a distorted space, and (c) the original cartesian space with a properly designed material in the blue region. The material properties obtained by transformation optics guarantee that the field propagation in (c) is the same as in (b).

To understand how transformation optics works, imagine a uniform magnetic field in free space. One can record the field lines location on a system of coordinates, as in Fig. 1.1a. If the field lines are fixed to the coordinates, the coordinate system carries the field lines with it under a distortion. Then, the trajectories of the field can be shaped by simply distorting the coordinates, as shown in Fig. 1.1b. Maxwell equations keep their form under coordinate transformations provided that the permittivity and permeability tensors in the transformed region are modified as follows [6, 7, 8, 10, 11]

$$\varepsilon'(\mathbf{x}') = \frac{\Lambda \cdot \varepsilon(\mathbf{x}) \cdot \Lambda^T}{\det(\Lambda)}, \quad (1.18)$$

$$\mu'(\mathbf{x}') = \frac{\Lambda \cdot \mu(\mathbf{x}) \cdot \Lambda^T}{\det(\Lambda)}, \quad (1.19)$$

where \mathbf{x} and \mathbf{x}' refer to the coordinates in the original and in the transformed space, respectively, $\varepsilon(\mathbf{x})$ and $\mu(\mathbf{x})$ are the permittivity and permeability distributions in the original cartesian space, and Λ is the Jacobian transformation matrix, with elements

$$\Lambda_{ij} = \frac{\partial x'_i}{\partial x_j}. \quad (1.20)$$

The transformed permittivity and permeability tensors ensure that Maxwell equations are obeyed by the new configuration of the field lines, which means that one can place a material with $\varepsilon'(\mathbf{x}')$ and $\mu'(\mathbf{x}')$ in the original space and the field will propagate as if the space had been distorted, as shown in Fig. 1.1c.

The electric and the magnetic field distributions in the transformed space are related to the field distributions in the initial undistorted space through the Jacobian transformation matrix as [6, 7, 8, 10, 11]

$$\mathbf{E}'(\mathbf{x}') = (\Lambda^T)^{-1} \mathbf{E}(\mathbf{x}), \quad (1.21)$$

$$\mathbf{H}'(\mathbf{x}') = (\Lambda^T)^{-1} \mathbf{H}(\mathbf{x}). \quad (1.22)$$

This shows that, starting from some initial fields $\mathbf{E}(\mathbf{x})$ and $\mathbf{H}(\mathbf{x})$, one can achieve any desired field distribution by constructing the adequate Jacobian transformation matrix Λ . Once this matrix is known, one can use Eqs. (1.18) and (1.19) to find the material properties required to shape the fields as intended.

A possible way of achieving the cumbersome permittivity and permeability distributions that usually arise from transformation optics is by means of metamaterials, artificially engineered media that can be designed to exhibit effective electromagnetic properties difficult or impossible to find in naturally occurring materials.

1.2.2 Metamaterials

Metamaterials are artificial media made from assemblies of multiple materials, usually arranged in repeating patterns, at scales that are smaller than the wavelength of the field they are tackling. They differ from conventional materials because their properties derive from the structure of their constituent units rather than from their constituent atoms [12, 13]. Because of this property, metamaterials can be engineered to interact with the fields beyond what is possible with conventional materials.

The advent of metamaterials has brought new opportunities to the physics, optics, and engineering communities, enabling the realization of physical phenomena that were previously only theoretical exercises. One of the first evidences of the potential of metamaterials was the realization of a structure shown to have a frequency band over which ε and μ were both negative [14]. In the 60's, Victor Veselago had reexamined some well-known electromagnetic phenomena assuming the hypothetical existence of materials with negative ε and μ [15]. Since no known naturally occurring material exhibits both $\varepsilon < 0$ and $\mu < 0$, for many years this work was regarded as a theoretical

curiosity. However, the experimental realization of metamaterials with negative μ and ε showed that Veselago's hypothesis could be realized and ignited the interest in the field of negative index materials [16]. This field has experienced a rapid development during the last decade, enabling intriguing phenomena such as negative refraction, for which light rays are refracted at an interface in the reverse direction to that normally expected, or perfect lenses, which can go beyond the diffraction limit of conventional lenses [17, 18].

When the field of transformation optics was born, metamaterials became a paradigm for controlling and manipulating electromagnetic fields in unprecedented ways [19]. One of the most exciting applications of metamaterials and transformation optics is the possibility of making an object invisible by means of an invisibility cloak [7, 20, 21]. Other applications of metamaterials and transformation optics include electromagnetic concentrators, which could play an important role in the harnessing of light in solar cells [22, 23, 24, 25]; illusion devices, which can make an object appear as if it was another one [26, 27]; rotators, which change the direction of the applied field [28]; anti-cloaks, which cancel the effect of a cloak [29, 30]; and many others.

Transformation optics and metamaterials have been applied to a wide range of physical areas [31, 32, 33], enabling the control and manipulation not only of electromagnetic fields but also of thermal radiation [34, 35, 36, 37], acoustic waves [38, 39], and elastomechanical waves [40, 41], for example. The control of static magnetic fields, which is covered in this thesis, has also benefited from both transformation optics and metamaterials [42, 43, 44, 45].

1.3 Magnetic materials

Magnetic fields are shaped and controlled by magnetic materials, which can be classified according to their magnetic permeability. The three most common types of magnetic materials are diamagnetic, paramagnetic, and ferromagnetic materials.

Diamagnetic materials exhibit a relative permeability lower than 1. The atoms in their volume do not show a net magnetic moment when there is no applied magnetic field. Under the influence of a magnetic field, diamagnetic materials produce a magnetization in the opposite direction to that of the magnetic field. Thus, the fields \mathbf{M} and \mathbf{H} in their volume tend to cancel out, which results in low magnetic inductions, as can be seen from the constitutive equation $\mathbf{B} = \mu_0(\mathbf{H} + \mathbf{M})$ [Eq. (1.6)]. Diamagnetic materials achieve this behaviour by expelling magnetic induction field lines towards their exterior. In the case of perfect diamagnetic materials, which exhibit a permeability $\mu \rightarrow 0$, all the magnetic induction field lines are expelled from the material volume, and the magnetic induction inside the material is $\mathbf{B} \rightarrow 0$. An example of perfect diamagnetic materials are superconductors, which exhibit $\mu \rightarrow 0$ under certain conditions (low temperatures, low applied magnetic fields, and low transport currents) [46, 47, 48].

The behaviour of paramagnetic materials, which exhibit a relative permeability slightly larger than 1, is very different. When there is no applied magnetic field, the atoms in these materials have the magnetic moments randomly oriented due to thermal agitation. Applied magnetic fields tend to align these magnetic moments, resulting in materials magnetized in the same direction as the magnetic field. Different from diamagnetic materials, which expel magnetic induction field lines, paramagnetic materials slightly attract magnetic induction field lines towards their volume.

Similar to paramagnetic materials, ferromagnetic materials are magnetized in the same direction as the magnetic field [49, 50]. However, ferromagnetic materials exhibit large permeabilities and their ability to attract magnetic fields is much stronger than that of paramagnetic materials. Most ferromagnets retain part of the magnetization even when the magnetic field is removed, which is known as remanent magnetization or residual magnetism M_r . The field that has to be applied to achieve $\mathbf{M} = 0$ in the ferromagnet is known as coercive field. The behaviour of ferromagnetic materials is described by hysteresis loops, which show how the response of the material to an applied field depends on its previous magnetizations. According to the shape of their hysteresis loop, ferromagnetic materials can be classified as *hard* and *soft* ferromagnets. In hard ferromagnets, the coercive field is high while in soft ferromagnets it is low. At temperatures above the Curie temperature, the ferromagnetism is lost and the material becomes paramagnetic due to thermal agitation. In this work we will only deal with soft ferromagnetic materials in small applied magnetic fields, which have a linear relation between \mathbf{M} and \mathbf{H} and their permeability can be assumed constant and very large, $\mu \rightarrow \infty$.

Soft ferromagnetic and perfect diamagnetic materials, which can exhibit effective permeabilities tending to $\mu \rightarrow \infty$ and $\mu \rightarrow 0$, respectively, are particularly interesting for shaping static magnetic fields because of their extreme and antagonistic magnetic responses. Some general features of these extreme-permeability materials are presented in Chapter 2.

Shaping magnetic fields with extreme permeabilities

Media with near-zero index of refraction (NZI) interacts with electromagnetic waves in an unusual manner [51]. In these media, electric and magnetic fields decouple at non-zero frequencies: the fields exhibit a nearly constant phase distribution but continue to dynamically oscillate in time [52, 53]. One of the first consequences of this wave-dynamics was found when analysing the ability of NZI materials to guide electromagnetic waves [54]. Typically, light propagating within waveguides or optical fibers is partially backscattered when encountering an obstacle such as a sharp bent in the waveguide. In contrast, materials with NZI can be bent and deformed without introducing any reflection, which enables an unusual full transmission of light through distorted channels with obstacles [55, 56, 57]. NZI media was also shown to lead to highly directive emitters that could radiate light with tailored phases and magnitudes [58]. These novel possibilities ignited the interest in the field of NZI, which has led to novel strategies for controlling the scattering [59], guiding [54], emission [60], concentration [61], and trapping [62, 63, 64, 65] of light, and is still a very active line of research [66, 60].

Inspired by these works, in this chapter we present some features of materials with near-zero (or zero) magnetic permeability in the presence of static magnetic fields. For comparison, we also study the case of materials with extremely large magnetic permeability, $\mu \rightarrow \infty$, which apparently show an antagonistic behaviour to that of $\mu \rightarrow 0$ materials. We start by considering externally applied magnetic fields and continue with the case of magnetic sources embedded in the material volume. While near-zero indexes of refraction are not typically found in natural occurring materials, $\mu \rightarrow 0$ and $\mu \rightarrow \infty$ are readily available in the static limit thanks to superconducting and soft ferromagnetic materials, respectively.

2.1 Shielding externally applied magnetic fields

Consider a linear, homogeneous, and isotropic perfect diamagnetic (PD, $\mu \rightarrow 0$) or ideal ferromagnetic (FM, $\mu \rightarrow \infty$) material with arbitrary three-dimensional geometry bounded by the surface S^{EXT} , as sketched in Fig. 2.1a, in an arbitrary externally applied magnetic field. Because there are not free currents involved, $\nabla \times \mathbf{H} = 0$, the magnetic field can be written in terms of a magnetic scalar potential ϕ ,

$$\mathbf{H} = -\nabla\phi, \quad (2.1)$$

everywhere in space. In linear, isotropic and homogeneous media, Eqs. (1.9) and (1.6) lead to $\nabla \cdot \mathbf{H} = 0$. Therefore, the magnetic scalar potential in all space is a solution of the Laplace equation $\nabla^2\phi = 0$. In particular, the magnetic scalar potential in the external region corresponds to the superposition of the applied magnetic scalar potential plus the response of the material, which depends on its permeability and geometry.

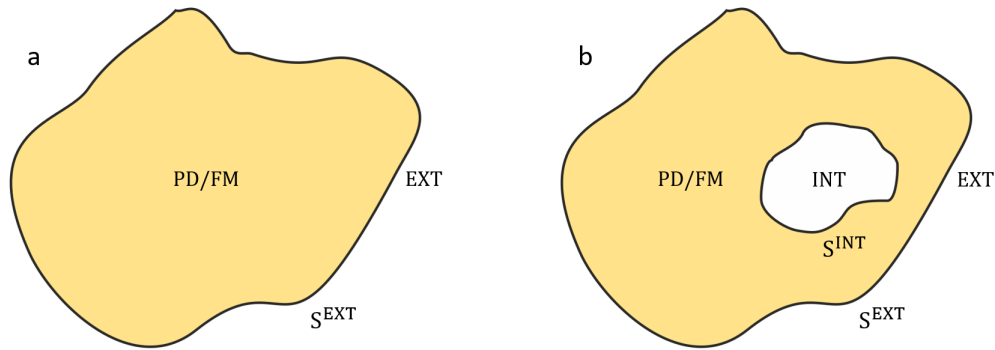


Figure 2.1: Sketches of (a) a solid perfect diamagnetic (PD) or ferromagnetic (FM) material with external surface S^{EXT} and (b) the PD/FM material with an empty hole of surface S^{INT} . The external region is denoted by EXT, the material region (yellow) by PD/FM, and the hole region by INT.

Consider now that the material has a hole of arbitrary geometry bounded by the surface S^{INT} , as sketched in Fig. 2.1b. Same as for the solid material, the magnetic field in all space can be derived from a magnetic scalar potential fulfilling the Laplace equation. In general, the field both in the exterior of the material and inside its hole depends on the hole geometry and position. In this section, we apply magnetostatic boundary conditions to demonstrate that this does not occur in materials with extreme permeability. The field distribution in the hole and outside perfect diamagnetic and ferromagnetic materials does not depend on the geometry nor on the position of the hole.

2.1.1 Perfect diamagnetic materials

Let us start with the case of a hollow perfect diamagnetic material. For finite externally applied magnetic fields, the magnetic fields in the material, \mathbf{H}^{PD} and \mathbf{B}^{PD} , must be finite to fulfill the magnetostatic boundary conditions. Therefore, the magnetic induction inside a material with $\mu \rightarrow 0$ tends to zero, $\mathbf{B}^{\text{PD}} = \mu\mu_0\mathbf{H}^{\text{PD}} \rightarrow 0$. Since the component of the magnetic induction normal to a material boundary must be continuous [Eq. (1.14)], the magnetic induction in the external region fulfills the boundary condition $B_n^{\text{EXT}}|_{S^{\text{EXT}}} = B_n^{\text{PD}}|_{S^{\text{EXT}}} \rightarrow 0$. This indicates that the external magnetic induction field lines always reach perfect diamagnetic materials tangential to their surfaces, as illustrated in Fig. 2.2. As $B_n^{\text{EXT}}|_{S^{\text{EXT}}} = 0$, the normal derivative of the magnetic scalar potential in the external region along the surface S^{EXT} fulfills [Eqs. (1.6) and (2.1)]

$$\left. \frac{\partial \phi^{\text{EXT}}}{\partial n} \right|_{S^{\text{EXT}}} = -H_n^{\text{EXT}}|_{S^{\text{EXT}}} = -\frac{1}{\mu_0} B_n^{\text{EXT}}|_{S^{\text{EXT}}} = -\frac{1}{\mu_0} B_n^{\text{PD}}|_{S^{\text{EXT}}} \rightarrow 0, \quad (2.2)$$

which sets a Neumann boundary condition for ϕ^{EXT} (see Appendix A1). The solution of the Laplace equation for ϕ^{EXT} is therefore uniquely determined: for each applied potential, there is a single solution for ϕ^{EXT} (apart from an arbitrary additive constant) that fulfills the boundary condition in Eq. (2.2). For this reason, the magnetic field distribution in the external region can only depend on the applied field and on the external surface S^{EXT} ; there is not a solution for each hole configuration (Fig. 2.2).

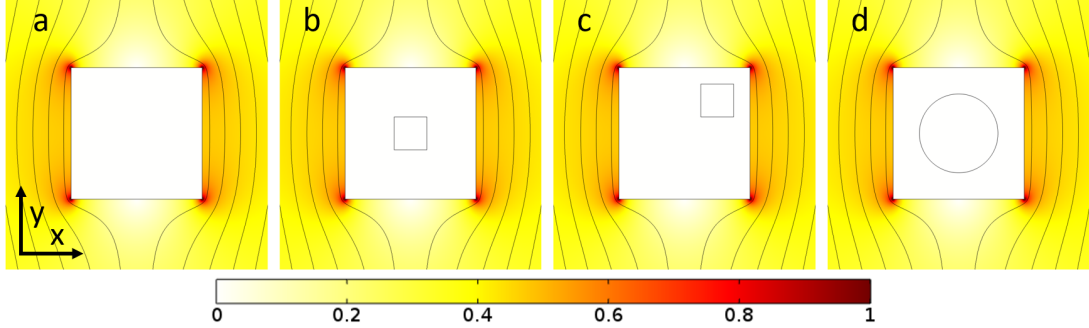


Figure 2.2: Numerical finite-elements calculations of the magnetic induction field lines and (in colors) the modulus of the magnetic induction in arbitrary units for four long (along the z -direction) perfect diamagnetic materials with squared cross-section and relative permeability $\mu = 10^{-5}$ in a uniform field applied along the y -direction. In (a) the material is solid, in (b) it has a long centered hole of squared cross-section, in (c) the material has the same hole as in (b) but it is not centered, and in (d) the material has a centered cylindrical hole.

The continuity of the normal component of \mathbf{B} also sets a Neumann boundary condition for the magnetic scalar potential inside the hole,

$$\left. \frac{\partial \phi^{\text{INT}}}{\partial n} \right|_{S^{\text{INT}}} = -H_n^{\text{INT}}|_{S^{\text{INT}}} = -\frac{1}{\mu_0} B_n^{\text{INT}}|_{S^{\text{INT}}} = -\frac{1}{\mu_0} B_n^{\text{PD}}|_{S^{\text{INT}}} \rightarrow 0. \quad (2.3)$$

Therefore, the solution of the Laplace equation for ϕ^{INT} is also unique. Since a uniform magnetic scalar potential fulfills the condition in Eq. (2.3) and is a solution of the Laplace equation, ϕ^{INT} must be uniform. Thus, according to Eq. (2.1), the magnetic field inside the hole is zero, which demonstrates that perfect diamagnetic materials always shield their holes from externally applied magnetic fields. This result is also observed in Fig. 2.2. These and all the finite-elements numerical calculations presented throughout this thesis are performed with Comsol Multiphysics.

2.1.2 Ferromagnetic materials

Consider now the case of hollow ferromagnetic materials. As above, for finite externally applied magnetic fields the magnetic fields in the material \mathbf{H}^{FM} and \mathbf{B}^{FM} must be finite. Thus, for $\mu \rightarrow \infty$ the magnetic field tends to zero, $\mathbf{H}^{\text{FM}} = \mathbf{B}^{\text{FM}}/(\mu\mu_0) \rightarrow 0$. The component of the magnetic field \mathbf{H} tangential to the ferromagnetic boundary must be continuous because there are not free surface current densities [Eq. (1.15)]. Therefore, the magnetic field in the external region fulfills the boundary condition $H_t^{\text{EXT}}|_{S^{\text{EXT}}} = H_t^{\text{FM}}|_{S^{\text{EXT}}} \rightarrow 0$, indicating that the magnetic field lines always enter the ferromagnetic volume perpendicular to the surface S^{EXT} , as shown in Fig. 2.3.

Since the gradient of the magnetic scalar potential is zero, $\mathbf{H}^{\text{FM}} = -\nabla\phi^{\text{FM}} = 0$, the potential inside the ferromagnetic material must be uniform, $\phi^{\text{FM}} = a^{\text{FM}}$, where a^{FM} is a constant. Due to the continuity of the scalar potential, the potential along both the external and the internal surfaces of the material is found to be

$$\phi^{\text{EXT}}|_{S^{\text{EXT}}} = \phi^{\text{FM}}|_{S^{\text{EXT}}} = a^{\text{FM}}, \quad (2.4)$$

$$\phi^{\text{INT}}|_{S^{\text{INT}}} = \phi^{\text{FM}}|_{S^{\text{INT}}} = a^{\text{FM}}. \quad (2.5)$$

These equations set two Dirichlet boundary conditions (see Appendix A1), which uniquely determine the solution of the magnetic scalar potential in the external region and in the internal region, respectively [67, 68]. Given an applied magnetic scalar potential, there is only a solution for ϕ^{EXT} and ϕ^{INT} fulfilling Eqs. (2.4) and (2.5), respectively. Similar to the case of perfect diamagnetic materials, since $\phi^{\text{INT}} = a^{\text{FM}}$ is a solution of the Laplace equation and fulfills the boundary condition in Eq. (2.5), ϕ^{INT} must be uniform. Thus, the magnetic field inside the hole of a ferromagnetic material is zero, which demonstrates that ferromagnetic materials shield their holes from any externally applied magnetic field (Fig. 2.3). This result leads to a property of the magnetic induction inside the ferromagnetic volume \mathbf{B}^{FM} . Since the component of \mathbf{B} normal to any interface must be continuous and the magnetic induction inside the ferromagnetic hole is zero, the magnetic induction field lines reach the ferromagnetic holes tangential to their surfaces, $B_n^{\text{FM}}|_{S^{\text{INT}}} = B_n^{\text{INT}}|_{S^{\text{INT}}} \rightarrow 0$ (Fig. 2.3).

Let us consider now a ferromagnetic material with the same external surface but a different hole. The magnetic scalar potential in the material must still be uniform but, in general, its magnitude can be different from a^{FM} . If that was the case, the magnetic scalar potential in the external region would be the same as that for the initial configuration except for an additive constant. Because the magnetic field cannot depend on this constant [Eq. (2.1)], the external field distribution does not depend on the hole geometry nor on its position; it only depends on the applied potential and on the material external surface S^{EXT} (Fig. 2.3).

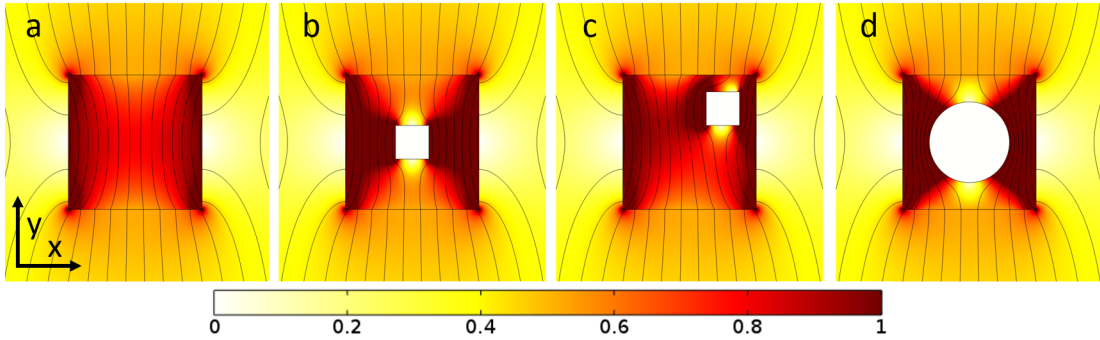


Figure 2.3: Numerical calculations of the magnetic induction field lines and (in colors) the modulus of the magnetic induction in arbitrary units when a uniform field is applied along the y -direction to (a) a long (along z) solid ferromagnetic material ($\mu = 10^5$), (b) the material in (a) with a long centered hole of squared cross-section, (c) the material in (a) with a long non-centered hole, and (d) the material in (a) with a centered long cylindrical hole.

2.2 Enclosing magnetic field sources

Once the case of externally applied magnetic fields has been analysed, a question arises as to whether these extreme-permeability materials also shield the external region from magnetic fields generated by sources located inside a hole in their volume. Interestingly, the shielding ability of these materials depends on the nature of the enclosed magnetic field sources. Here we demonstrate that perfect diamagnetic and ferromagnetic materials can shield irrotational or conservative magnetic fields, $\nabla \times \mathbf{H} = 0$, but are unable to shield rotational fields, $\nabla \times \mathbf{H} \neq 0$, which arise from enclosed free current densities.

2.2.1 Shielding irrotational fields

Consider a hollow material with arbitrary three-dimensional shape, as sketched in Fig. 2.1b, with a magnetic field source located inside its hole. To start with, we assume there are not free current densities inside the hole, i.e. $\mathbf{J}_f = 0$. The magnetic field source

could be a magnet, for example, which creates an approximately dipolar magnetic field distribution. When $\mathbf{J}_f = 0$, the magnetic field in all space can be written in terms of a magnetic scalar potential ϕ which, in turn, can be derived from the Laplace equation and the magnetostatic boundary conditions.

In perfect diamagnetic materials, the property $\mathbf{B}^{\text{PD}} \rightarrow 0$ allows to specify the normal derivative of the magnetic scalar potential (Neumann boundary condition) both at the material internal [Eq. (2.3)] and external [Eq. (2.2)] surfaces. Same as for the case of externally applied magnetic fields, these conditions determine the solution for ϕ^{INT} and ϕ^{EXT} , which leads to two general properties. First, the magnetic field inside the hole only depends on the sources it encloses and on the hole surface S^{INT} ; it does not depend on the surface S^{EXT} nor on the position of the hole inside the material (Figs. 2.4a-c). Second, because a uniform potential is found to fulfill the boundary condition in Eq. (2.2) and is a solution of the Laplace equation, the magnetic scalar potential in the external region ϕ^{EXT} must be uniform and, thus, the magnetic field reaching the external region must be zero (Figs. 2.4a-d).

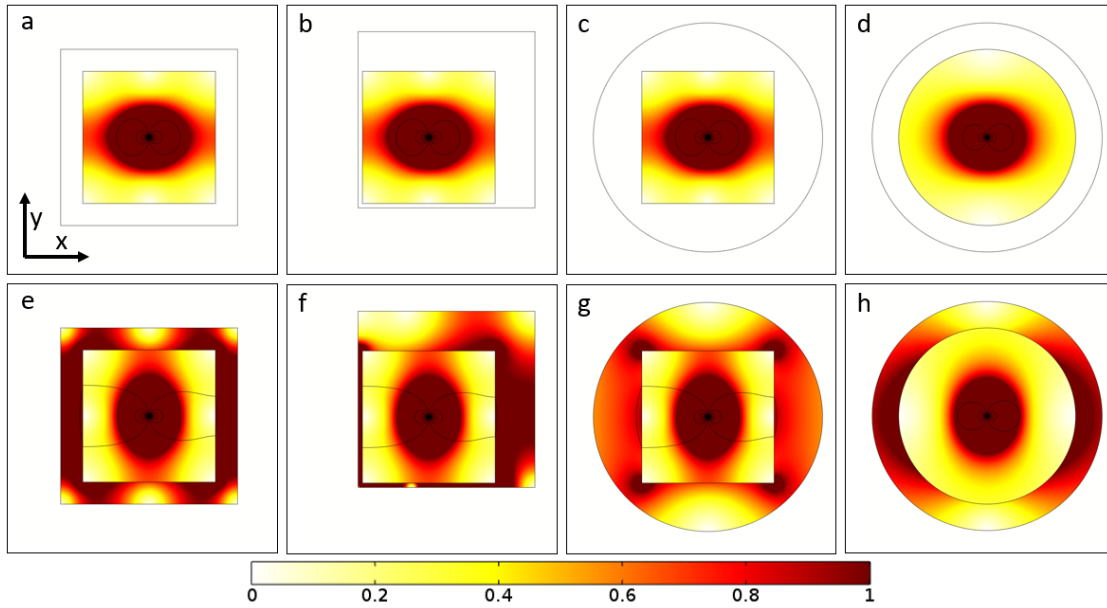


Figure 2.4: Numerical calculations of the magnetic induction field lines and (in colors) the modulus of the magnetic induction in arbitrary units for a long magnetic dipole with magnetic moment per unit length $\mathbf{m} = m\mathbf{u}_y$ placed inside the hole of different long (along z) materials. In (a) a perfect diamagnetic material ($\mu = 10^{-5}$) of squared cross-section with a long concentric hole. In (b) same as in (a) for a non-concentric hole. In (c) a cylindrical material with a centered long hole of squared cross-section. In (d) same as in (c) for a cylindrical hole. Panels (e)-(h) show the same results as panels (a)-(d) for a ferromagnetic material ($\mu = 10^5$).

In ferromagnetic materials, $\mathbf{H}^{\text{FM}} \rightarrow 0$ specifies the magnetic scalar potential (Dirichlet boundary condition) at the material internal [Eq. (2.5)] and external [Eq. (2.4)] surfaces, which uniquely determine the solution for ϕ^{INT} and ϕ^{EXT} , respectively. As a result, the magnetic field inside the hole only depends on the enclosed sources and on the internal surface S^{INT} (Figs. 2.4e-h). Similar to the case of perfect diamagnetic materials enclosing sources, because a uniform magnetic scalar potential is a solution of the Laplace equation and fulfills the boundary condition in Eq. (2.4), the magnetic field reaching the external region is zero (Figs. 2.4e-h).

These results demonstrate that materials with extreme-permeability $\mu \rightarrow 0$ and $\mu \rightarrow \infty$ do not only shield their holes from externally applied fields, but also shield their exterior from irrotational fields generated inside their holes.

2.2.2 Enclosing free currents with zero-permeability media

Consider now that there is a free current density \mathbf{J}_f inside the hole of a perfect diamagnetic material, so that $\nabla \times \mathbf{H} = \mathbf{J}_f \neq 0$. For the sake of simplicity, let us start by assuming a long (along the z -axis) hollow perfect diamagnetic material with a long straight wire of current I placed inside its hole, as sketched in Fig. 2.5.

Because the line integral of the magnetic field along any closed path enclosing the hole must fulfill $\oint \mathbf{H} \cdot d\mathbf{l} = I$, the magnetic field in the material volume, \mathbf{H}^{PD} , and the magnetic field in the external region, \mathbf{H}^{EXT} , must be finite and different from zero. This leads to some general properties of $\mu \rightarrow 0$ materials. First, since \mathbf{H}^{PD} is finite, the magnetic induction inside the material is zero; $\mathbf{B}^{\text{PD}} = \mu\mu_0\mathbf{H}^{\text{PD}} \rightarrow 0$ for $\mu \rightarrow 0$. Second, because $\mathbf{H}^{\text{EXT}} \neq 0$, the magnetic field reaches the external region, indicating that perfect diamagnetic materials cannot shield the field created by a long wire. Because $\mathbf{B}^{\text{PD}} \rightarrow 0$ and the normal component of the magnetic induction must be continuous, the magnetic field induction reaches the external region tangential to S^{EXT} ($B_n^{\text{EXT}}|_{S^{\text{EXT}}} = B_n^{\text{PD}}|_{S^{\text{EXT}}} \rightarrow 0$). Similarly, the magnetic field induction inside the hole reaches the material tangential to S^{INT} ($B_n^{\text{INT}}|_{S^{\text{INT}}} = B_n^{\text{PD}}|_{S^{\text{INT}}} \rightarrow 0$). These properties are illustrated in Fig. 2.6.

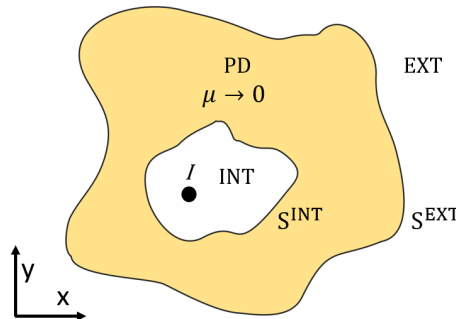


Figure 2.5: Sketch of the cross section of a long (along z) PD material of external surface S^{EXT} enclosing a long straight wire of current I inside a hole of surface S^{INT} .

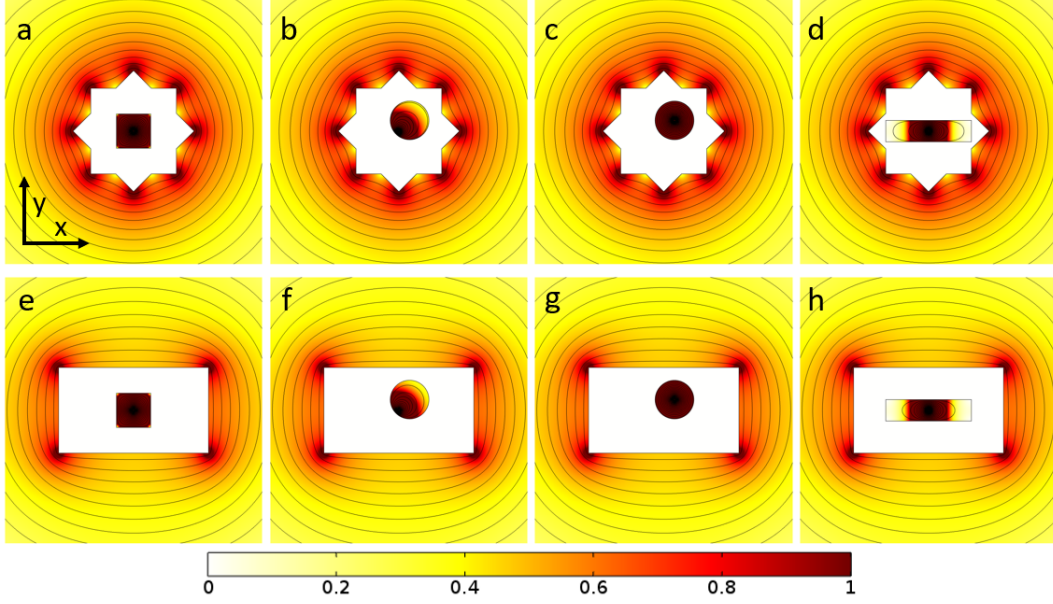


Figure 2.6: Numerical calculations of the magnetic induction field lines and (in colors) the modulus of the magnetic induction in arbitrary units when a long straight wire of current I is surrounded by different long (along z) perfect diamagnetic materials ($\mu = 10^{-5}$). In (a)-(d) the cross section of the external surface of the material is a star, while in (e)-(h) it is a rectangle. In (a) and (e) the wire is centered inside a centered hole with squared cross section. In (b) and (f) the wire position is the same as in (a) and (e) but it is located inside a cylindrical discentered hole. In (c) and (g), the wire is centered inside the cylindrical hole. In (d) and (f) the wire is centered inside a centered hole with rectangular cross section.

In materials with intermediate positive values of μ , the magnetic field distribution both inside the hole and in the external region depends on the hole surface S^{INT} , on the hole position, on the material external surface S^{EXT} , and on the wire position inside the hole. Here we demonstrate that this does not occur in the case of perfect diamagnetic materials with $\mu \rightarrow 0$. For this discussion, we use the magnetic vector potential \mathbf{A} , which is defined as $\nabla \times \mathbf{A} = \mathbf{B}$ and for the chosen symmetry can be written as $\mathbf{A} = A(x, y)\mathbf{u}_z$.

In the volume of a hollow perfect diamagnetic material, since $\mathbf{B}^{\text{PD}} = \nabla \times \mathbf{A}^{\text{PD}} \rightarrow 0$, the magnetic vector potential must be uniform, $A^{\text{PD}} = a^{\text{PD}}$, where a^{PD} is a constant. Due to the continuity of the vector potential, the moduli of the magnetic vector potential along the internal and the external boundaries of the material, respectively, are

$$A^{\text{INT}}|_{S^{\text{INT}}} = A^{\text{PD}}|_{S^{\text{INT}}} = a^{\text{PD}}, \quad (2.6)$$

$$A^{\text{EXT}}|_{S^{\text{EXT}}} = A^{\text{PD}}|_{S^{\text{EXT}}} = a^{\text{PD}}. \quad (2.7)$$

These equations set a Dirichlet boundary condition for A^{INT} and for A^{EXT} , respectively (see Appendix A2). The constant a^{PD} may depend on the chosen material configuration but this dependence, similar to the arbitrary choice of the reference magnetic vector potential, only contributes to A^{INT} and A^{EXT} as an additive constant that does not have an effect on the field distribution in these regions ($\mathbf{B} = \nabla \times \mathbf{A}$). Therefore, the conditions in Eqs. (2.6) and (2.7) uniquely determine both \mathbf{B}^{INT} and \mathbf{B}^{EXT} . On the one hand, the magnetic field induction inside the hole only depends on \mathbf{J}_f and on the surface S^{INT} ; it does not depend on the material outer surface (Fig. 2.6). On the other hand, the magnetic field induction in the external region only depends on the total current enclosed by the material and on the external surface S^{EXT} . For this reason, the field reaching the exterior of a perfect diamagnetic material does not depend on the wire position inside the hole, nor on the hole position or geometry (Fig. 2.6).

In this section, we have discussed the case of a long straight wire inside a long perfect diamagnetic material, but similar ideas apply to other geometries. We now briefly discuss the case of a circular loop carrying a current I embedded inside the hole of a perfect diamagnetic volume with axial symmetry, as sketched in Fig. 2.7.

As above, the property $\mathbf{B}^{\text{PD}} \rightarrow 0$ uniquely determines the magnetic induction distribution both inside the material hole and in the external region by requiring the magnetic vector potential both at S^{INT} and S^{EXT} to be a constant. Consider first the geometry in Fig. 2.7a. Since the net free current enclosed by the material external surface S^{EXT} is zero, the material can shield the external region from the field created by the wire, as occurred for irrotational fields. This is shown in Fig. 2.8a. Consider now the toroidal geometry in Fig. 2.7b. In this case, one can think of closed paths in the external region that enclose a total free current different from zero. Thus, in order for the Maxwell equation $\nabla \times \mathbf{H} = \mathbf{J}_f$ to be fulfilled, the field created by the current loop must exit the toroid. As illustrated in the examples in Figs. 2.8b-d, the external field distribution only depends on the current I and on the geometry of the surface S^{EXT} .

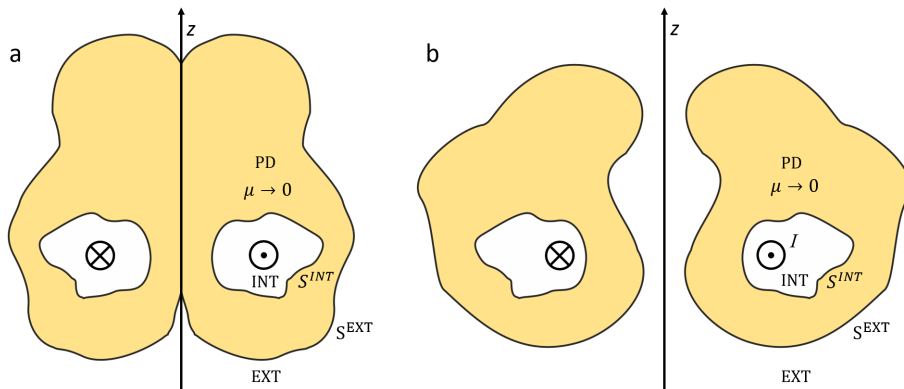


Figure 2.7: Sketch of the cross-section of two hollow perfect diamagnetic materials with a circular loop carrying a current I inside the hole. In (a) the axis of revolution crosses the material, while in (b) there is a space between the axis and the material.

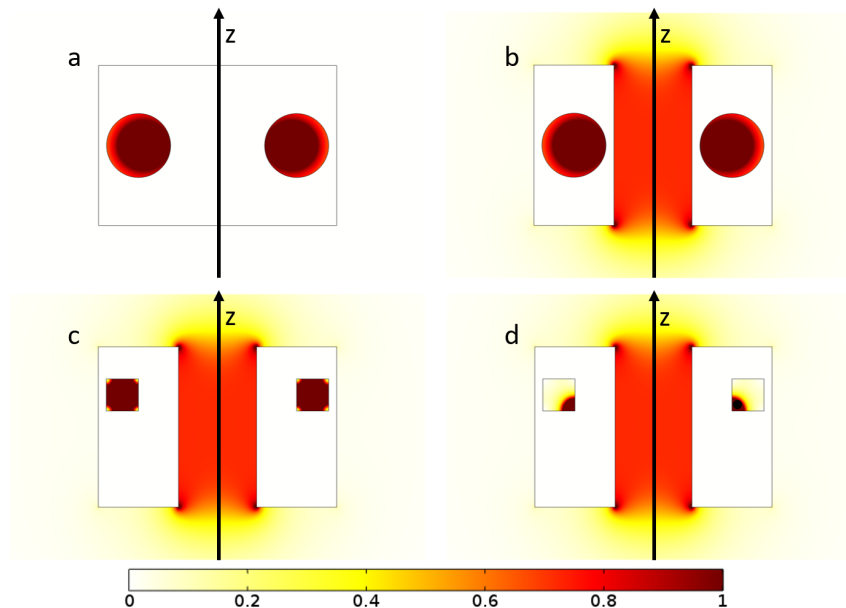


Figure 2.8: Numerical calculations of the modulus of the magnetic induction in arbitrary units when a circular loop of current I is enclosed by different perfect diamagnetic materials with $\mu = 10^{-5}$. In (a) the wire is covered by a cylindrical material with a circular toroidal hole. In (b), (c) and (d) the wire is covered by a cylindrical shell with a toroidal hole of (b) circular and (c) and (d) squared cross-section. In (a), (b), and (c) the wire is centered inside the toroidal hole, while in (d) it is decentered.

The results presented in this section show that perfect diamagnetic materials can reshape the magnetic field created by a wire in novel ways. Since the magnetic field exiting the material is always tangential to the material surface ($B_n^{\text{EXT}}|_{S^{\text{EXT}}} = B_n^{\text{PD}}|_{S^{\text{EXT}}} \rightarrow 0$), one can design the adequate material shape to meet specific needs. For example, a cylindrical shell enclosing a single circular current loop provides a uniform magnetic field distribution similar to that of a solenoid (Figs. 2.8b-d). This is reminiscent of the results obtained for epsilon-near-zero media embedding free currents, which have been used to derive highly directive emitters with tailored phases [52, 58].

2.2.3 Wire superposition with zero-permeability media

Once the features of perfect diamagnetic media enclosing a wire have been studied, a question arises as what is the collective effect of several wires enclosed in different cavities. Imagine a long perfect diamagnetic material with arbitrary cross-section bounded by the surface S^{EXT} that has not only one but n holes of arbitrary cross-section, each of them limited by the surface S_i^{INT} , $i = 1, 2, \dots, n$. There is a long straight wire of current I inside one of these holes, for example inside the hole j . In the material volume, $\mathbf{B}^{\text{PD}} \rightarrow 0$ leads to a uniform A^{PD} , which sets a Dirichlet boundary condition for the magnetic vector potential at every material boundary.

First, because the free current enclosed by any hole $i \neq j$ is zero, a constant vector potential A_i^{INT} is found to fulfill the Laplace equation $\nabla^2 A_i^{\text{INT}} = 0$ and the Dirichlet boundary condition $\forall i$. Therefore, the magnetic field inside the holes $i \neq j$, $\mathbf{B}_i^{\text{INT}} = \nabla \times \mathbf{A}_i^{\text{INT}}$, is zero, indicating that perfect diamagnetic materials shield their cavities from the field generated inside other cavities, as illustrated in the example in Fig. 2.5a. Second, the wire creates a field different from zero inside the cavity j , which is in general modified due to the presence of the material. Because A_j^{INT} also fulfills a Dirichlet boundary condition, the field distortion inside the hole j only depends on the hole surface S_j^{INT} ; it does not depend on the presence of other cavities nor on the external surface of the material. Third, since the magnetic vector potential in the external surface of the material is also specified, the external field distribution can only depend on the current enclosed by S^{EXT} and on the geometry of the surface S^{EXT} . For example, in the case of a cylindrical external surface enclosing a long wire of current I , the external field corresponds to that of a long wire of current I in the center of the cylindrical surface, as shown in Figs. 2.9a and b.

From these results, the case of N wires placed in different cavities in the material is straightforward. The field inside each cavity only depends on its surface and on the free current it is enclosing, while the field in the external region depends on the external surface as well as on the total current enclosed by S^{EXT} . For example, if there are N wires of current I enclosed by the material (located in the same or in different cavities), the external field is the same as if a wire of current NI was placed inside one of the cavities. In the case of a circular external surface, it corresponds to the field created by a centered wire of current NI (Figs. 2.9c and d). If the total current enclosed by S^{EXT} is zero, the shielding property of perfect diamagnetic materials is recovered.

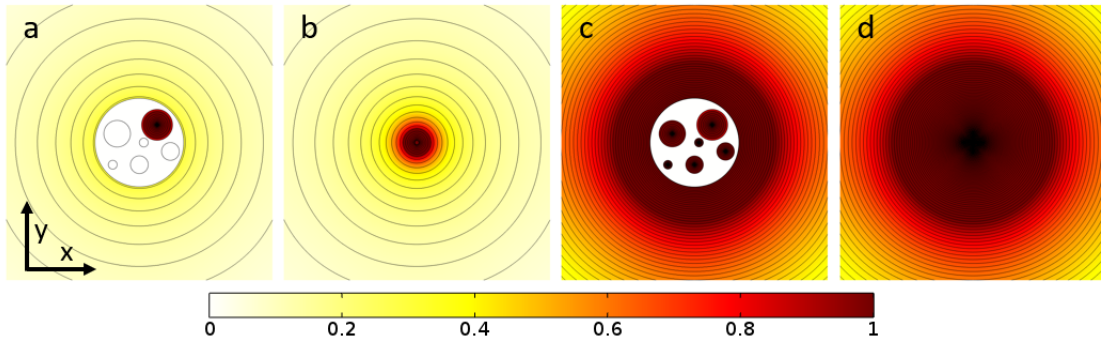


Figure 2.9: Numerical calculations of the magnetic induction field lines and (in colors) the modulus of the magnetic induction in arbitrary units in four different cases. In (a) a long cylindrical perfect diamagnetic material ($\mu = 10^{-5}$) with a straight wire of current I embedded in one of its holes. In (c) the same material as in (a) with six straight wires of current I , each of them in a different hole. In (b) and (d) a straight wire of current I and $6I$, respectively, located at the geometric center of the external surface of the material in (a) and (c).

Therefore, perfect diamagnetic materials enable the overlapping of the field created by several wires located at different positions; the external field distribution is the same as if all the wires were located at the same point. This may offer new possibilities for current technologies where several wires are used to provide strong magnetic fields, as in superconducting magnets. In most of these applications, the consideration of the strong Lorentz forces the wires must withstand is crucial. Because wires located in different cavities inside a perfect diamagnetic material would be isolated, the forces between the wires would be zero, which could help reduce the extremely large forces that appear in some practical applications. In these cases, however, the internal compressive forces that perfect diamagnetic materials enclosing wires must stand should be considered.

2.2.4 Enclosing free currents with infinite-permeability media

Consider now a ferromagnetic material with $\mu \rightarrow \infty$ surrounding a free current density \mathbf{J}_f . For simplicity, consider the same geometry as that in Fig. 2.5: a long hollow material with a long straight current wire of intensity I placed inside its hole.

The magnetostatic Maxwell equation $\nabla \times \mathbf{H} = \mathbf{J}_f$ shows that, same as perfect diamagnetic materials, ferromagnets cannot shield rotational fields created by internal sources. If the field in the external region was zero, the line integral of the magnetic field along paths in the external region that enclose the wire would not fulfill $\oint \mathbf{H} \cdot d\mathbf{l} = I$. In the ferromagnetic material volume, different from the cases studied above, in which $\mu \rightarrow \infty$ led to $\mathbf{H}^{\text{FM}} \rightarrow 0$, the equation $\nabla \times \mathbf{H} = \mathbf{J}_f$ also forces the magnetic field to be different from zero. A first consequence of having $\mathbf{H}^{\text{FM}} \neq 0$ inside the ferromagnetic volume is that both the magnetic induction and the magnetization of the material tend to infinity, $\mathbf{B}^{\text{FM}} = \mu\mu_0\mathbf{H}^{\text{FM}} \rightarrow \infty$ and $\mathbf{M}^{\text{FM}} = (\mu - 1)\mathbf{H}^{\text{FM}} \rightarrow \infty$ for $\mu \rightarrow \infty$.

This reveals that ferromagnetic materials surrounding free currents cannot be considered linear materials with permeability $\mu \rightarrow \infty$. In practice, ferromagnetic materials with a large magnetization exhibit a non-linear behaviour, experience saturation and their relative magnetic permeability is dramatically reduced; instead of $\mu \rightarrow \infty$ their permeability becomes $\mu \rightarrow 1$. Therefore, when enclosing a current with a ferromagnetic material, the material permeability cannot be assumed to be $\mu \rightarrow \infty$ because the material magnetization \mathbf{M}^{FM} would tend to infinity and it would become saturated even for low values of \mathbf{H}^{FM} . Because the discussion of non-linear phenomena in ferromagnetic materials falls beyond the scope of this thesis, we leave this discussion here.

2.2.5 Analogy between perfect diamagnets and electric conductors

The derived results for perfect diamagnetic media in magnetostatics can be regarded as an analogy to the well-known properties of conducting media in electrostatics. Here we explore this analogy by taking into account that the response of conducting media can be explained in terms of induced electric charges and the response of perfect diamagnetic media in terms of magnetization currents.

In electrostatics, the electric field in the volume of a hollow electric conductor must be zero, $\mathbf{E}^C \rightarrow 0$. In the presence of an applied electrostatic field, the material achieves this property by inducing some electric charges at its surfaces. In a similar way, magnetization currents are induced at the surfaces of perfect diamagnetic materials in the presence of magnetostatic fields in order to provide a zero magnetic induction $\mathbf{B}^{PD} \rightarrow 0$ in the material volume. For externally applied fields, these surface charge and current densities appear at the material external surface, S^{EXT} and only depend on the applied field distribution and on the geometry of S^{EXT} . Because the fields cannot reach the volume of conductors and perfect diamagnets, their cavities are shielded from electrostatic and magnetostatic fields, respectively.

When the source of electrostatic and magnetostatic fields is located in a cavity inside the material, induced charges and magnetization currents appear at the surface of the cavity, S^{INT} , to provide $\mathbf{E}^C = 0$ and $\mathbf{B}^{PD} = 0$, for conductors and perfect diamagnets, respectively. From Maxwell equations, one finds that the net charge induced at the surface S^{INT} of a conductor must be equal and with opposite sign to the total charge Q enclosed by the cavity. In an analogous way, the net magnetization current induced at the surface S^{INT} of a perfect diamagnet must be equal and with opposite sign to the total current I enclosed by the cavity. Because the total net induced charge in the conductor and the total net magnetization current in the perfect diamagnetic volume must be zero, when $Q \neq 0$ and $I \neq 0$, some surface charges and magnetization currents must appear at S^{EXT} to compensate for the excess of charges and currents at S^{INT} . These charges and currents must be distributed along S^{EXT} in such a way that the conditions $\mathbf{E}^C = 0$ and $\mathbf{B}^{PD} = 0$ are maintained. The charge and the current density induced at S^{EXT} create an electrostatic and a magnetostatic field different from zero outside the material volume, respectively. This shows that conductors and perfect diamagnetic materials only shield their exterior from the electrostatic and magnetostatic fields generated inside their volume when the total free charge or the total free current they enclose, respectively, is zero.

In spite of this similarities, the way in which conductors and perfect diamagnetic materials shape the electrostatic and the magnetostatic fields, respectively, is very different. Because $\mathbf{E}^C = 0$ and the Maxwell equations require the tangential component of \mathbf{E} to be continuous at any interface, electrostatic fields \mathbf{E} always enter and exit conductors perpendicularly. In contrast, magnetostatic fields \mathbf{B} are always tangential to the perfect diamagnetic surfaces because $\mathbf{B}^{PD} = 0$ and it is the component of \mathbf{B} normal to an interface the one that has to be continuous.

2.3 Chapter summary and conclusions

The formulation of the magnetic field distribution in terms of a magnetic scalar/vector potential fulfilling the magnetostatic boundary conditions has enabled the derivation of some interesting general features of materials with extreme permeabilities.

First, both perfect diamagnetic and ferromagnetic materials have been shown to shield any cavity in their volume from externally applied magnetic fields as well as their external region from irrotational fields generated inside their volume. The shielding ability of these materials was already known, but it had only been derived for some particular fields and geometries. In contrast, the formulation of Neumann and Dirichlet problems has enabled the generalization of the shielding property to any applied field distribution and material geometry. Second, we have demonstrated that perfect diamagnetic and ferromagnetic materials cannot shield their exterior from rotational magnetic fields generated by free current densities located inside their volume.

For the case of perfect diamagnetic materials enclosing free currents, the external field distribution has been shown to depend solely on the geometry of the material external surface and on the total current enclosed by the material. This property could be exploited to find novel ways of shaping and controlling static magnetic fields. For example, we have shown that cylindrical shells made of perfect diamagnetic material with a toroidal hole enclosing a circular current loop achieve a uniform magnetic field inside its hole that is even more uniform than the field achieved by a solenoid of the same length. Also, interesting collective effects arise when considering a perfect diamagnetic material surrounding several wires located in different cavities, as the wires do not interact with each other but the field in the exterior of the material appears as if all the wires were located at the same point.

The properties derived for perfect diamagnetic materials could be explored in practice using superconducting materials. For low temperatures and applied magnetic fields, superconductors exhibit an effective uniform, isotropic, and linear magnetic permeability $\mu \rightarrow 0$. However, when the applied magnetic field becomes larger than a certain field, the property $\mu \rightarrow 0$ is lost and the superconducting material does not longer behave as a perfect diamagnet. This may be a drawback specially in the case of surrounding one or several wires with perfect diamagnetic materials, since the field close to the wires could be very strong.

Shaping magnetic fields with positive-permeability metamaterials

The toolbox for controlling static magnetic fields has recently been enriched thanks to the development of magnetic metamaterials. In the static limit, metamaterials can be defined as combinations of existing materials that result in novel effective permeability tensors [42, 43, 44, 45]. This concept was introduced in 2007 by Wood and Pendry, who examined the possibility of creating metamaterials at near-zero frequencies and designed a magnetic metamaterial able to render magnetic objects undetectable to dc magnetic fields [42]. Prior to this work, metamaterials had been discussed only at microwave frequencies and above, and were defined as assemblies of materials smaller than the wavelength of the field. In the static limit, since the wavelength associated to the magnetic field tends to infinite, metamaterials can be constructed at any scale.

The introduction of static magnetic metamaterials was crucial for realizing several magnetic devices derived from transformation optics. The magnetic permeability resulting from the space transformations, which is usually inhomogeneous and anisotropic and can seldom be found in naturally occurring materials, can be effectively emulated by magnetic metamaterials. The building blocks that constitute these metamaterials are usually superconducting ($\mu \rightarrow 0$) and soft ferromagnetic materials ($\mu \rightarrow \infty$). The natural existence of these materials with extreme permeabilities makes the magnetostatic regime particularly interesting for exploiting transformation optics and metamaterials.

Magnetic metamaterials have enabled the realization of a wide range of devices for shaping magnetic fields. Among them, one finds magnetic invisibility cloaks that make objects magnetically undetectable [69, 70, 71, 72, 73]; concentrators that focus magnetic fields [74, 75, 76, 77, 78]; hoses that route and transfer magnetic field to long distances [79, 80, 81]; and even magnetic wormholes that magnetically connect two regions in space through an undetectable path [82].

In this chapter, some novel devices for controlling static magnetic fields that can be realized with magnetic metamaterials with positive permeability are presented. First, in Sec. 3.1, we show that two-dimensional and three-dimensional shells with extremely anisotropic permeabilities (very large in the radial direction and small in the angular one) are able to concentrate externally applied magnetic fields inside their holes [83]. In Sec. 3.2, we demonstrate that these shells do not only concentrate external fields, but also expel towards the exterior the magnetic field created by magnetic sources located inside their holes. When surrounding a magnetic material with these shells, this expulsion property results in a magnification of the response the material creates to an applied field, which corresponds to that of an enlarged material. The proposed extremely anisotropic concentrating shells could be used as a general strategy for enhancing the sensitivity of a magnetic sensor, which could benefit applications requiring the detection of low magnetic fields. However, these shells enhance the sensor sensitivity at the cost of increasing their detectability; the shell magnifies the distortion of the probing field created by the sensor, which can be a major drawback when non-invasive sensing is required. To tackle this issue, in Sec. 3.3, we present a cloaking shell that can render a magnetic sensor undetectable. Even though the sensitivity of a sensor is reduced by the cloaking shell, the sensor is still able to measure the applied field [84].

3.1 Magnetic field concentration

The first theoretical proposals for concentrating static magnetic fields using metamaterials were derived using transformation optics [74, 85]. It was demonstrated that long cylindrical shells with extremely anisotropic permeability achieve large concentrations of magnetic fields [74]. These ideas have been experimentally verified both for static [86] and quasistatic magnetic fields [87]. Magnetic concentrators could benefit a wide range of technologies working with zero and low-frequency magnetic fields, including magnetic sensors [83], biomedical techniques such as magnetic resonance imaging or transcranial magnetic stimulation [74], and wireless power transfer [87].

Here we extend the results for concentrating magnetic fields with long cylindrical shells to the cases of long shells with arbitrary cross-section and spherical shells. In this way, the shape of the concentrator could be tailored according to its application. As an example, consider a magnetic sensor that is covered by a concentrating shell with the goal of enhancing its sensitivity [83]. The possibility of adapting the shape of the concentrator to the shape of the sensor allows a more efficient use of space, which enables a more dense packaging of sensors. As another example, imagine two coils covered by two cylindrical concentrating shells that enhance the coupling between them [87]. Concentrators designed according to the shape of the coils they enclose may give the same coupling enhancement as cylindrical concentrators with a much larger air gap between the shells, which is an important parameter in wireless power transfer [87].

3.1.1 Long concentrators with arbitrary geometry

We start by extending the results for long cylindrical concentrators [74] to the case of arbitrarily shaped long concentrators. Their properties can be derived using transformation optics. For electromagnetic waves, similar transformations have been employed to derive arbitrarily shaped cloaks [88, 89] and concentrators [23, 90].

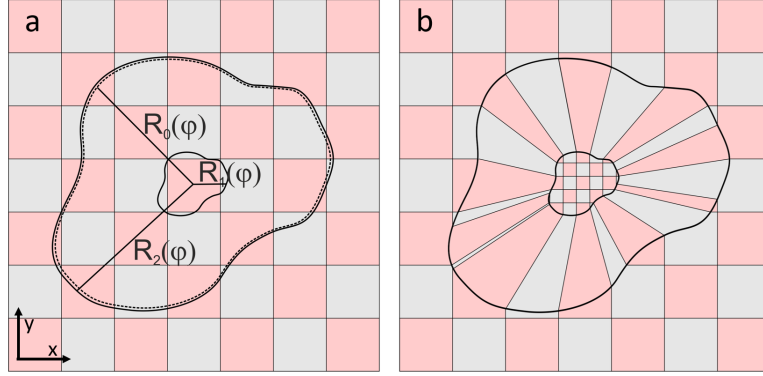


Figure 3.1: (a) Sketch of the original space. (b) Sketch of the transformed space. The space $\rho < R_0(\varphi)$ is compressed into the region $\rho' < R_1(\varphi)$ and the space $R_0(\varphi) < \rho < R_2(\varphi)$ is expanded to fill the region $R_1(\varphi) < \rho' < R_2(\varphi)$.

Consider three infinitely long (along the z -direction) surfaces with arbitrary cross-section. The radial distance between each surface and the origin of coordinates depends on φ and can be denoted as $R_1(\varphi)$, $R_0(\varphi) > R_1(\varphi)$, and $R_2(\varphi) > R_0(\varphi)$ (Fig. 3.1a). To simplify the derivation, we consider conformal surfaces. In this case, $R_0(\varphi)$ and $R_2(\varphi)$ can be written in terms of $R_1(\varphi)$ as $R_0(\varphi) = (r_0/r_1)R_1(\varphi)$ and $R_2(\varphi) = (r_2/r_1)R_1(\varphi)$, where r_0 , r_1 , and r_2 are positive parameters fulfilling $r_2 > r_0 > r_1 > 0$. Inspired by the transformation in [74] for the cylindrical case, we transform the space as illustrated in Fig. 3.1b. First, the space in the region $0 < \rho < R_0(\varphi)$ is radially compressed through the transformation,

$$\begin{cases} \rho' = \left(\frac{r_1}{r_0}\right)\rho, \\ \varphi' = \varphi, \\ z' = z, \end{cases} \quad \rho \in [0, R_0(\varphi)], \quad (3.1)$$

where ρ , φ and z are the coordinates in the original physical space and ρ' , φ' and z' are the coordinates in the transformed virtual space. Second, to guarantee that the space is continuous, the space in the region $R_0(\varphi) < \rho < R_2(\varphi)$ is expanded as

$$\begin{cases} \rho' = R_2(\varphi) \left(\frac{\rho}{R_2(\varphi)}\right)^k, \\ \varphi' = \varphi, \\ z' = z, \end{cases} \quad \rho \in [R_0(\varphi), R_2(\varphi)], \quad (3.2)$$

where the parameter $k \in (1, \infty)$ is related to the parameters r_0 , r_1 , and r_2 through

$$r_0 = r_2(r_1/r_2)^{1/k}. \quad (3.3)$$

Finally, the space in the region $\rho \in (R_2(\varphi), \infty)$ is not transformed. If one assumes cylindrical surfaces, $R_1(\varphi) = R_1$, $R_0(\varphi) = R_0$, and $R_2(\varphi) = R_2$, the transformation in [74] is recovered.

The magnetic permeability required to shape the magnetic field in the same way as the proposed space transformation would, can be obtained from Eqs. (1.19) and (1.20) of the transformation optics theory. The permittivity is not discussed because we are assuming static magnetic fields, which are decoupled from electric fields. Expressed in the cylindrical basis, the calculated relative permeability tensors are

$$\boldsymbol{\mu}' = \begin{pmatrix} \mu_{\rho\rho} & \mu_{\rho\varphi} & \mu_{\rho z} \\ \mu_{\varphi\rho} & \mu_{\varphi\varphi} & \mu_{\varphi z} \\ \mu_{z\rho} & \mu_{z\varphi} & \mu_{zz} \end{pmatrix} = \begin{pmatrix} 1 & 0 & 0 \\ 0 & 1 & 0 \\ 0 & 0 & \left(\frac{r_1}{r_2}\right)^{2/k-2} \end{pmatrix}, \quad (3.4)$$

in the region $\rho' < R_1(\varphi)$,

$$\boldsymbol{\mu}' = \begin{pmatrix} k + \frac{(k-1)^2}{k} \frac{1}{R_2(\varphi)^2} \left(\frac{dR_2(\varphi)}{d\varphi}\right)^2 & -\frac{(k-1)}{k} \frac{1}{R_2(\varphi)} \frac{dR_2(\varphi)}{d\varphi} & 0 \\ -\frac{(k-1)}{k} \frac{1}{R_2(\varphi)} \frac{dR_2(\varphi)}{d\varphi} & 1/k & 0 \\ 0 & 0 & \frac{1}{k} \left(\frac{\rho'}{R_2(\varphi)}\right)^{2/k-2} \end{pmatrix}, \quad (3.5)$$

in the region $R_1(\varphi) \leq \rho' \leq R_2(\varphi)$, and $\boldsymbol{\mu}' = 1$ in the region, $\rho' > R_2$.

If one considers static magnetic fields independent of the z -coordinate and without z -component, the problem shows translational symmetry along the z -axis. In this case, only the left-upper 2x2 minors of the tensors have physical relevance. This means that the presented space transformation only requires the presence of a linear, inhomogeneous and anisotropic magnetic material with the permeability in Eq. (3.5) placed in the region $R_1(\varphi) < \rho' < R_2(\varphi)$, which, constitutes the magnetic concentrator.

Transformation optics does not only give the required permeability to effectively transform the space as desired, but also how the magnetic field distribution is shaped in the transformed space. The expression for the magnetic field can be found from Eqs. (1.22), (3.1) and (3.2). For our goal of concentrating the magnetic field, we are interested in the magnetic field distribution inside the hole, which can be written as

$$\mathbf{H}'(\rho', \varphi') = \left(\frac{r_1}{r_2}\right)^{1/k-1} \mathbf{H} \left(\left(\frac{r_1}{r_2}\right)^{1/k-1} \rho', \varphi' \right), \quad \rho' \in [0, R_1(\varphi)]. \quad (3.6)$$

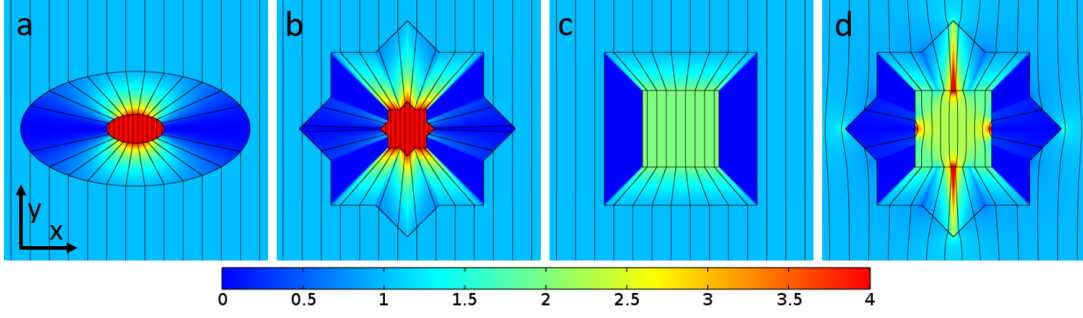


Figure 3.2: Numerical calculations of the magnetic induction field lines and, in colors, the y -component of the magnetic induction normalized to $\mu_0 H_0$ when a uniform magnetic field H_0 is applied along the y -direction to four long (along the z -direction) objects with $\mu_{\rho\rho} = 10^5$, $\mu_{\varphi\varphi} = 10^{-5}$, and $\mu_{\rho\varphi} = \mu_{\varphi\rho} = 0$. The object cross-sections are (a) a hollow ellipsoid with internal and external surfaces $R_1(\varphi)$ and $R_2(\varphi) = 4R_1(\varphi)$, (b) a hollow star with surfaces $R_1(\varphi)$ and $R_2(\varphi) = 4R_1(\varphi)$, (c) a hollow square with surfaces $R_1(\varphi)$ and $R_2(\varphi) = 2R_1(\varphi)$, and (d) a star of surface $R_2(\varphi)$ with a squared hole of surface $R_1(\varphi)$.

For example, if one assumes a uniform applied magnetic field \mathbf{H}_0 , the magnetic field reaching the hole of the concentrator is

$$\mathbf{H}^{\text{INT}} = \left(\frac{r_2}{r_1} \right)^{1-1/k} \mathbf{H}_0, \quad (3.7)$$

which depends on the parameter k . When k is minimum, $k \rightarrow 1$, the field is not concentrated inside the hole, $\mathbf{H}^{\text{INT}} = \mathbf{H}_0$, and when k is maximum, $k \rightarrow \infty$, the field concentration is maximum, $\mathbf{H}^{\text{INT}} = (r_2/r_1) \mathbf{H}_0$. This result can be understood from Eqs. (3.1) and (3.3). When $k \rightarrow 1$, $r_0 \rightarrow r_1$, and there is no space concentration. In contrast, when $k \rightarrow \infty$, $r_0 \rightarrow r_2$, which is the case of maximum concentration; all the space in the region $\rho < R_2(\varphi)$ is compressed into the region $\rho < R_1(\varphi)$. The parameter k controls the amount of space that is compressed inside the hole and, therefore, indicates how strong the magnetic field concentration is.

Because the angular permeability of the shell is found to be directly related to the parameter k as $\mu_{\varphi\varphi} = 1/k$, shells with $\mu_{\varphi\varphi} \rightarrow 0$ are the ones achieving the largest magnetic field concentration. In this case, the components of the concentrator relative permeability can be written as $\mu_{\rho\rho} \rightarrow \infty$, $\mu_{\varphi\varphi} \rightarrow 0$ and $\mu_{\rho\varphi} = \mu_{\varphi\rho} = \frac{1}{R_2(\varphi)} \frac{dR_2(\varphi)}{d\varphi}$. In general, the off-diagonal components of the magnetic permeability change the direction of the magnetic induction: $\mu_{\rho\varphi}$ converts part of the angular field H_φ into a radial magnetic induction B_ρ , and viceversa for $\mu_{\varphi\rho}$. In the case of maximum field concentration, the off-diagonal permeabilities $\mu_{\rho\varphi} = \mu_{\varphi\rho} = \frac{1}{R_2(\varphi)} \frac{dR_2(\varphi)}{d\varphi}$ can be assumed to be zero because, independently of their value, the magnetic induction field lines follow a radial path towards the concentrator hole due to $\mu_{\rho\rho} \rightarrow \infty$. All the performed finite-elements numerical calculations confirm this assumption, even when considering shells with sharp

edges. Some examples are shown in Figs. 3.2a-c, which illustrate that shells of different geometries with permeability $\mu_{\rho\rho} \rightarrow \infty$, $\mu_{\varphi\varphi} \rightarrow 0$, and $\mu_{\varphi\rho} = \mu_{\rho\varphi} = 0$ achieve the ideal concentration ratio resulting from Eq. (3.7).

The field distribution in the external region may also be of interest. Because the space $\rho > R_2$ has not been transformed, the field distribution outside the concentrator is not modified by the presence of the shell. Therefore, the proposed concentrating shells can achieve strong field concentrations inside their holes without distorting the applied magnetic field. Figures 3.2a-c show that the shells achieving the maximum field concentration exhibit this non-distorting property even when the off-diagonal components of their permeability tensor are set to zero.

Figure 3.2d shows that the properties we have obtained for shells with the permeability in Eq. (3.5) do not hold if the inner and the outer surface of the shell have different shapes. Because we have transformed the space considering three conformal surfaces [$R_2(\varphi)/r_2 = R_0(\varphi)/r_0 = R_1(\varphi)/r_1$, Fig. 3.1], shells with surfaces that do not fulfill this condition exhibit different properties to those derived above. In particular, the field inside their holes is not uniform and their presence distorts the applied magnetic field distribution. If the goal was to obtain a shell with inner and outer surfaces with different shapes that was able to uniformly concentrate the field inside its hole without distorting the applied field, different space transformations and permeability tensors would be required.

3.1.2 Spherical concentrators

The long concentrators presented above can only achieve a two-dimensional field concentration. In this section, we explore the possibility of having a three-dimensional concentrator. In this case, transformation optics leads to inhomogeneous permeabilities, which may be difficult to construct in a practical realization, even when considering the simplest geometry of a spherical shell. A different strategy that can be used to derive the properties of homogeneous concentrators is solving the magnetostatic Maxwell equations. However, these equations must be derived for each shell geometry and for each applied field distribution. For simplicity, we consider a spherical shell with internal radius R_1 and external radius R_2 in the presence of a uniform magnetic field, \mathbf{H}_0 , applied along the z -axis [83]. We assume a linear, homogeneous and anisotropic relative permeability fulfilling (in spherical coordinates r, θ, φ) $\mu_{r\theta} = \mu_{\theta r} = \mu_{r\varphi} = \mu_{\varphi r} = \mu_{\theta\varphi} = \mu_{\varphi\theta} = 0$ and $\mu_{\theta\theta} = \mu_{\varphi\varphi}$. To simplify the notation, we define the angular and the radial permeability as $\mu_\theta = \mu_{\theta\theta}$ and $\mu_r = \mu_{rr}$, respectively. Since there are not free currents and the material is homogeneous, the magnetic field can be written in terms of a magnetic scalar potential ϕ that fulfills the Laplace equation. This potential reads

$$\nabla^2 \phi^{\text{SHE}} = \frac{\partial}{\partial r} \left(r^2 \frac{\partial \phi^{\text{SHE}}}{\partial r} \right) + \frac{1}{\sin\theta} \frac{\mu_\theta}{\mu_r} \frac{\partial}{\partial \theta} \left(\sin\theta \frac{\partial \phi^{\text{SHE}}}{\partial \theta} \right) = 0, \quad (3.8)$$

in the shell region (SHE: $R_1 < r < R_2$) and

$$\nabla^2 \phi^{\text{INT,EXT}} = \frac{\partial}{\partial r} \left(r^2 \frac{\partial \phi^{\text{INT,EXT}}}{\partial r} \right) + \frac{1}{\sin \theta} \frac{\partial}{\partial \theta} \left(\sin \theta \frac{\partial \phi^{\text{INT,EXT}}}{\partial \theta} \right) = 0, \quad (3.9)$$

inside the hole (INT: $r \leq R_1$) and in the external region (EXT: $r \geq R_2$). The general solution of these equations is

$$\phi^{\text{INT}} = a^{\text{INT}} r \cos \theta, \quad (3.10)$$

$$\phi^{\text{SHE}} = \left(b^{\text{SHE}} r^{1/2(-1-\sqrt{1+8\mu_\theta/\mu_r})} + c^{\text{SHE}} r^{1/2(-1+\sqrt{1+8\mu_\theta/\mu_r})} \right) \cos \theta, \quad (3.11)$$

$$\phi^{\text{EXT}} = \left(\frac{d^{\text{EXT}}}{r^2} - H_0 r \right) \cos \theta. \quad (3.12)$$

The coefficients a^{INT} , b^{SHE} , c^{SHE} , and d^{EXT} are obtained from the magnetostatic boundary conditions [Eqs. (1.15) and (1.14)]: the angular component of \mathbf{H} and the radial component of \mathbf{B} must be continuous at the material surfaces $r = R_1$ and $r = R_2$.

The magnetic field inside the hole of the spherical shell is uniform and in the direction of the applied magnetic field, $\mathbf{H}^{\text{INT}} = -a^{\text{INT}} \mathbf{u}_z$ [Eq. (3.10)], and can be written as

$$\mathbf{H}^{\text{INT}} = \frac{6\mu_r \alpha (R_2/R_1)^{(3+\alpha)/2}}{-4 - \mu_r - 4\mu_r \mu_\theta + 3\mu_r \alpha + (4 + \mu_r + 4\mu_r \mu_\theta + 3\mu_r \alpha)(R_2/R_1)^\alpha} \mathbf{H}_0, \quad (3.13)$$

where $\alpha^2 = 1 + 8\mu_\theta/\mu_r$. The maximum field that can be concentrated inside the hole of a spherical shell is found in the limit $\mu_r \rightarrow \infty$ and $\mu_\theta \rightarrow 0$ and is

$$\mathbf{H}^{\text{INT}}(\mu_r \rightarrow \infty, \mu_\theta \rightarrow 0) = \frac{3(R_2/R_1)^2}{1 + 2(R_2/R_1)} \mathbf{H}_0. \quad (3.14)$$

The magnetic field distribution outside the spherical shell may also be of interest. Equation (3.12) indicates that the response of the shell is equivalent to the field created by a point dipole centered inside the hole of the spherical shell with dipolar magnetic moment $m = 4\pi d^{\text{EXT}}$ pointing towards the z -direction. Positive values of d^{EXT} indicate that the shell attracts the magnetic field, while negative values of d^{EXT} indicate that it expels the field. When d^{EXT} is zero, the shell does not distort the uniform applied magnetic field. From

$$d^{\text{EXT}} = \frac{-2(-1 - \mu_r + 2\mu_\theta \mu_r) R_2^3 [1 - (R_2/R_1)^\alpha]}{-4 - \mu_r - 4\mu_r \mu_\theta + 3\mu_r \alpha + (4 + \mu_r + 4\mu_r \mu_\theta + 3\mu_r \alpha)(R_2/R_1)^\alpha} H_0, \quad (3.15)$$

one finds that spherical concentrators with $\mu_r \rightarrow \infty$ and $\mu_\theta \rightarrow 0$ slightly expel the magnetic field ($d^{\text{EXT}} < 0$), as shown in Fig. 3.3a. Therefore, the anisotropic shell providing the maximum magnetic field concentration distorts the applied magnetic field.

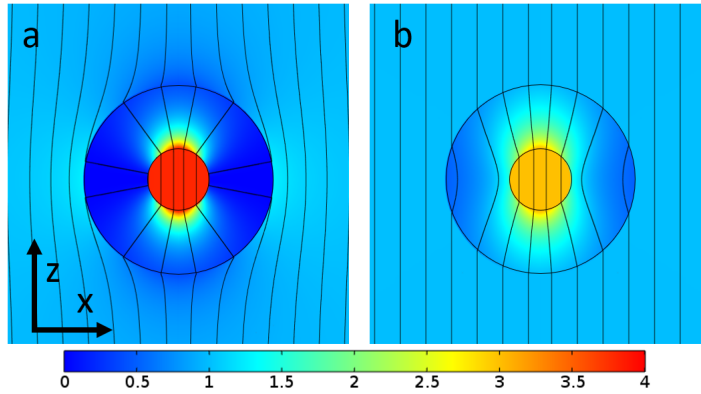


Figure 3.3: Numerical calculations of the magnetic induction field lines and (in colors) the z -component of the magnetic induction normalized to $\mu_0 H_0$ when a uniform magnetic field H_0 is applied along the z -direction to two different spherical concentrators with internal radius R_1 and external radius $R_2 = 3R_1$. The shell relative permeabilities are $\mu_r = 10^5$ and $\mu_\theta = 10^{-5}$ in (a), and $\mu_r = 10^5$ and $\mu_\theta = 1/2$ in (b).

We can now explore which is the maximum magnetic field concentration that a spherical shell that does not distort the external magnetic field can achieve. According to Eq. (3.15), a spherical shell does not distort uniform applied fields ($d^{\text{EXT}} = 0$) when its radial and angular permeability fulfill

$$\mu_\theta = \frac{1 + \mu_r}{2\mu_r}. \quad (3.16)$$

The field inside a non-distorting spherical shell is found as [Eq. (3.13)]

$$\mathbf{H}^{\text{INT}} = \left(\frac{R_2}{R_1}\right)^{1-1/\mu_r} \mathbf{H}_0. \quad (3.17)$$

Therefore, the largest field concentration that can be achieved without distorting the uniform applied field is found in the limit $\mu_r \rightarrow \infty$ and $\mu_\theta \rightarrow 1/2$ and is

$$\mathbf{H}^{\text{INT}}(\mu_r \rightarrow \infty, \mu_\theta \rightarrow 1/2) = \frac{R_2}{R_1} \mathbf{H}_0. \quad (3.18)$$

We can now compare the field concentration provided by a distorting shell with $\mu_r \rightarrow \infty$ and $\mu_\theta \rightarrow 0$ [Eq. (3.14), Fig. 3.3a] to that of a non-distorting shell with $\mu_r \rightarrow \infty$ and $\mu_\theta \rightarrow 1/2$ [Eq. (3.18), Fig. 3.3b]. For small radii ratios, $R_2/R_1 \rightarrow 1$, the two concentrators achieve the same magnetic field concentration ratio, (R_2/R_1) . Interestingly, for large radii ratios, $R_2/R_1 \rightarrow \infty$, the non-distorting shells maintain the same concentration ratio, while the concentration ratio achieved by distorting shells is increased to $(3/2)(R_2/R_1)$.

3.1.3 Realizing magnetic concentrators with metamaterials

The two-dimensional and the three-dimensional shells presented above must exhibit an extremely anisotropic permeability in order to achieve a strong concentration of magnetic field inside their holes. The radial component of the permeability must be large to direct the applied magnetic field lines towards the hole of the shell, whereas the angular component of the permeability must be low to guarantee that once a field line has entered the shell it does not exit without reaching the hole. Such extremely anisotropic permeabilities are not found in natural occurring materials. However, thanks to the recent introduction of magnetic metamaterials, one can adequately combine materials with extremely large permeability $\mu \rightarrow \infty$ (ferromagnetic materials) and materials with extremely low permeability $\mu \rightarrow 0$ (perfect diamagnetic materials) to design a shell that effectively behaves as if it was anisotropic.

The first proposal on how to arrange ferromagnetic and perfect diamagnetic materials to emulate a cylindrical concentrator with permeability $\mu_{\rho\rho} \rightarrow \infty$ and $\mu_{\varphi\varphi} \rightarrow 0$ was theoretically proposed and numerically verified in [74]. It was shown that an alternation of ferromagnetic and perfect diamagnetic rectangular prisms placed radially, as shown in the example in Fig. 3.4b, exhibits practically the same effective properties as the ideal concentrator in Fig. 3.4a; the magnetic field is concentrated inside the hole by a factor r_2/r_1 [Eq. (3.7)] and the applied field is kept undistorted. Figures 3.4c and d illustrate for the case of a long shell with squared cross-section that the same strategy can be applied to effectively emulate the properties of extremely anisotropic long shells with arbitrary cross sections.

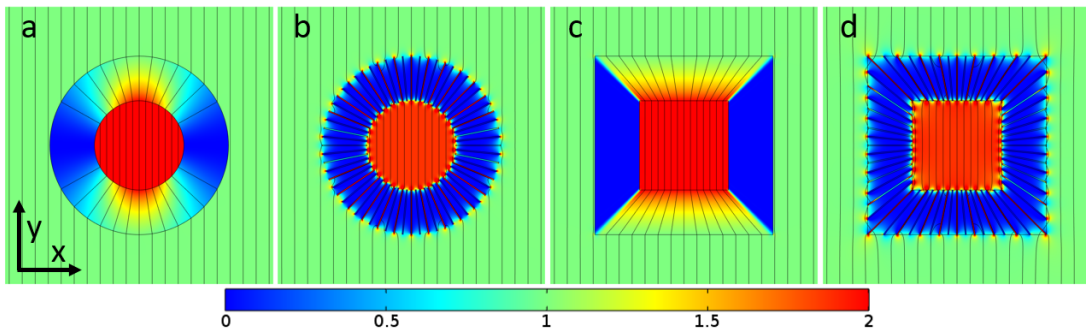


Figure 3.4: Numerical calculations of the magnetic induction field lines and, in colors, the y -component of the magnetic induction (normalized to $\mu_0 H_0$) for a uniform magnetic field H_0 applied along the y -direction to four different devices. In (a) a long cylindrical concentrator with radial and angular relative permeability $\mu_{\rho\rho} = 10^5$ and $\mu_{\varphi\varphi} = 10^{-5}$ with internal and external radii $R_1(\varphi) = R_1$ and $R_2(\varphi) = 2R_1$. In (b) the shell in (a) discretized by a set of 32 soft ferromagnetic ($\mu = 10^5$) and 32 perfect diamagnetic ($\mu = 10^{-5}$) alternating thin bars. Panels (c) and (d) are equivalent to panels (a) and (b), respectively, for a concentrator with squared cross-section.

The concentration properties of cylindrical shells consisting of alternating ferromagnetic and perfect diamagnetic prisms made of μ -metal and superconductors, respectively, was experimentally verified for the first time in [86]. Because superconductors only exhibit the permeability of a perfect diamagnetic material ($\mu \rightarrow 0$) at low temperatures, this metamaterial requires cryogenics to fully function. Interestingly, these experiments showed that the metamaterial can still concentrate magnetic fields at room temperature, where the effective permeability of the superconductors is not longer $\mu \rightarrow 0$ but $\mu \rightarrow 1$. Even though the concentration ratio at room temperature was lower than the achieved at low temperatures, these results demonstrated that strong field concentrations can be achieved using ferromagnetic pieces solely. These results also showed that the properties derived for long cylindrical concentrators hold even when the height of the shell is made of the order of its radii.

Spherical concentrators with radial permeability $\mu_r \rightarrow \infty$ and angular permeability $\mu_\theta \rightarrow 0$ can also be emulated by adequate combinations of ferromagnetic and perfect diamagnetic bars. In a general situation, alternating small bars of ferromagnetic and perfect diamagnetic materials placed radially towards the center of the shell hole would be necessary. However, if the goal is to concentrate a uniform applied field, one can benefit from the axisymmetric symmetry of the problem to construct a simpler metamaterial design [83]. In this case, the spherical shell can be discretized by alternating funnels of ferromagnetic and perfect diamagnetic materials, as illustrated in the example in Fig. 3.5. Similar to the experiments at room temperature for a cylindrical shell discretized with ferromagnetic and superconducting pieces [86], experimental results (Figs. 3.6a and b) demonstrate that spherical shells discretized with ferromagnetic (μ -metal) funnels solely also provide a strong concentration of both uniform and non-uniform applied magnetic fields [83].

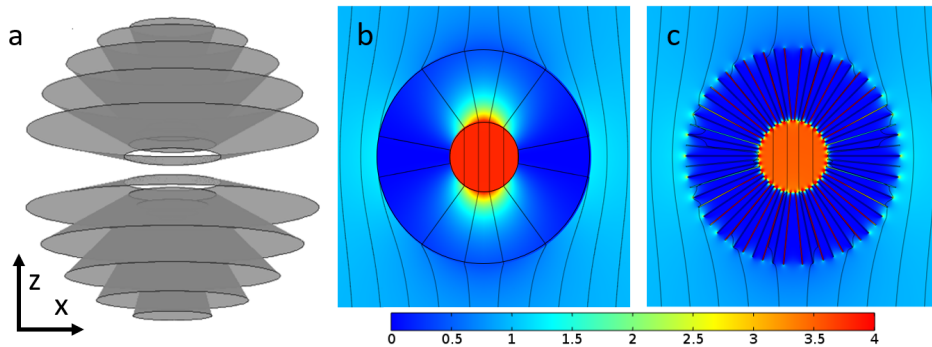


Figure 3.5: (a) Sketch of a spherical concentrator discretized with funnels. (b) Magnetic induction field lines and, in colors, z -component of the magnetic induction normalized to $\mu_0 H_0$ for a uniform field $\mathbf{H}_0 = H_0 \mathbf{u}_z$ applied to a spherical concentrator with internal radius R_1 , external radius $3R_1$, and permeability $\mu_r = 10^5$ and $\mu_\theta = 10^{-5}$. (c) Discretized version of the sphere in (b) consisting of an alternation of 16 ferromagnetic ($\mu = 10^5$) and 15 perfect diamagnetic ($\mu = 10^{-5}$) funnels.

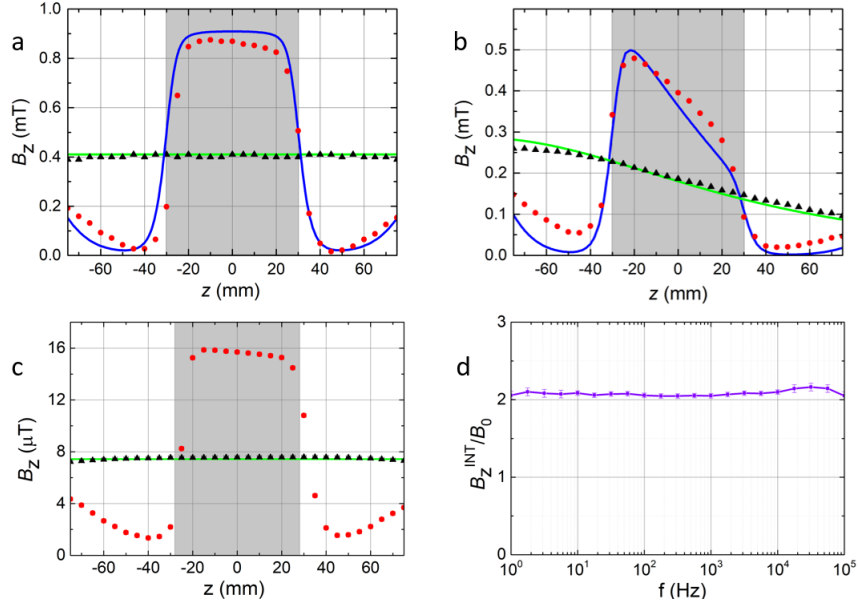


Figure 3.6: Measurements (red dots) of B_z along the z -axis when placing the spherical concentrator in (a) a uniform dc field created by a pair of Helmholtz coils, (b) a non-uniform field created by a single coil, and (c) a uniform field created by a pair of Helmholtz coils excited by a sinusoidal current of 200Hz. Errors bars fit within the symbol size. The analytic applied induction (green line), the measurements of the applied magnetic induction (black triangles) and numerical results obtained assigning a permeability of $\mu = 10^5$ to the μ -metal (blue line) are shown for comparison. The hole region is shadowed in gray. In (d) the concentration ratio at the center of the shell is plotted as a function of the frequency of the current feeding the pair of Helmholtz coils.

In the experiments, a spherical shell with internal radius $R_1 = 30\text{mm}$ and external radius $R_2 = 90\text{mm}$ was discretized into a set of 10 ferromagnetic funnels positioned as shown in the sketch in Fig. 3.5a. The uniform applied field was generated by feeding a dc current $I = 0.5\text{A}$ to a pair of Helmholtz coils, while the inhomogeneous field was generated by feeding the current only to one of the two coils. The z -component of the magnetic induction measured along the z -axis with a Hall probe is plotted in Fig. 3.6a for the uniform field and in Fig. 3.6b for the non-uniform field. Results show that the shell enhances not only the magnitude of the field but also its gradient.

The experimental realization has led to another important result. Even though the theory was derived for static magnetic fields, the shell concentrates not only static but also low-frequency applied magnetic fields [87, 83]. Figure 3.6c shows the measurements obtained when feeding the pair of Helmholtz coils with a sinusoidal current $I_{\text{RMS}} = 10\text{mA}$ and frequency 200Hz, which clearly resemble those for the dc current in Fig. 3.6a. The spherical concentrator keeps its concentrating ability from 1Hz to 100kHz (Fig. 3.6d). The amplitude of the applied magnetic induction along the z -axis is $B_0 = 0.41\text{mT}$ (taking into account the contribution of the Earth magnetic field) for all frequencies.

3.2 Magnifying magnetic materials

The magnetic concentrators presented above have been shown to concentrate magnetic fields inside their holes without distorting externally applied magnetic fields. However, this result is only valid when the concentrator holes do not include magnetic materials. In this section, we demonstrate that a concentrator surrounding a magnetic material has two different effects. First, it concentrates the magnetic field inside the material and, second, it amplifies the magnetic field distortion the material creates as a response to the applied field. As a result, the distortion of the externally applied magnetic field is equivalent to that of an enlarged material. Magnifying a magnetic material could be useful, for example, to save on exotic materials with relevant magnetic properties or to measure properties of a magnetic sample, such as the permeability, with higher precision.

For the following studies we consider long concentrating shells with arbitrary cross-section. Similar results could be derived for the case of spherical concentrators. However, because their properties do not result from transformation optics, their study is more complex and requires the derivation of the solutions of the magnetostatic Maxwell equations for each applied field and for each material geometry. In contrast, in the case of long concentrators with arbitrary cross-section, transformation optics enables the derivation of some general properties of the device that can be applied to any applied field and to any material sample.

3.2.1 Magnetic field expulsion

When the long cylindrical magnetic concentrator was proposed [74], it was demonstrated that the shell was able not only to concentrate inside its hole externally applied magnetic fields, but also to expel towards its exterior the field created by magnetic sources located inside its hole. In this section, we extend this result to demonstrate that the long concentrating shells with arbitrary cross-section presented above are also able to expel toward their exterior magnetic fields generated inside their holes.

First, we apply transformation optics to derive the properties of a shell able to expel magnetic fields towards its exterior. A transformation analogous to that in Eqs. (3.1) and (3.2) and Fig. 3.1 is required. Consider three infinitely long (along the z -direction) surfaces with arbitrary cross-section bounded by $R_1(\varphi)$, $R_0(\varphi)$, and $R_2(\varphi)$, respectively, fulfilling $R_0(\varphi) = (r_0/r_1)R_1(\varphi)$ and $R_2(\varphi) = (r_2/r_1)R_1(\varphi)$, with $r_2 > r_0 > r_1 > 0$, as sketched in Fig. 3.7a. The space is transformed as illustrated in Fig. 3.7b. First, the space in the region $\rho > R_0(\varphi)$ is radially expanded through the transformation

$$\begin{cases} \rho' = \left(\frac{r_2}{r_0}\right)\rho, \\ \varphi' = \varphi, \\ z' = z, \end{cases} \quad \rho \in (R_0(\varphi), \infty), \quad (3.19)$$

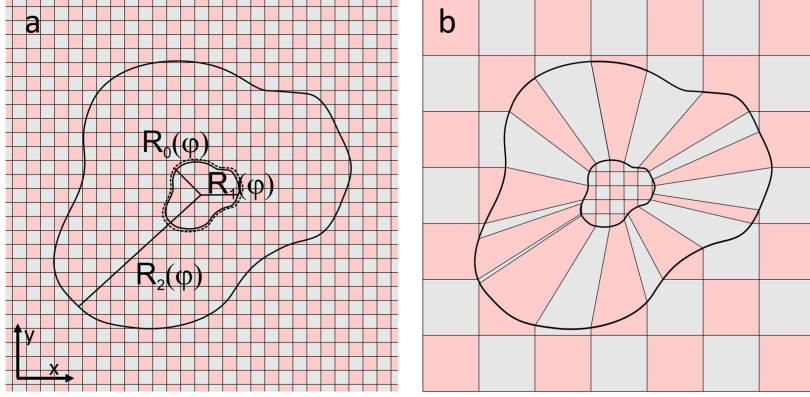


Figure 3.7: (a) Sketch of the original space. (b) Sketch of the transformed space. The space $\rho > R_0(\varphi)$ is expanded into the region $\rho' > R_2(\varphi)$ and the space $R_1(\varphi) < \rho < R_0(\varphi)$ is expanded to fill the region $R_1(\varphi) < \rho' < R_2(\varphi)$.

and, second, the space in the region $R_1(\varphi) < \rho < R_0(\varphi)$ is expanded as

$$\begin{cases} \rho' = R_1(\varphi) \left(\frac{\rho}{R_1(\varphi)} \right)^k, \\ \varphi' = \varphi, \\ z' = z. \end{cases} \quad \rho \in [R_1(\varphi), R_0(\varphi)]. \quad (3.20)$$

The space in the region $\rho < R_1(\varphi)$ is not transformed. In order for the space to be continuous at $\rho = R_0(\varphi)$, the parameters k , r_0 , r_1 , and r_2 must fulfill

$$r_0 = r_1(r_2/r_1)^{1/k}. \quad (3.21)$$

Equations (1.19) and (1.20) give the permeability tensors that shape the field in the same way as this space transformation. One finds $\mu' = 1$ in the region $\rho' < R_1(\varphi)$,

$$\mu' = \begin{pmatrix} k + \frac{(k-1)^2}{k} \frac{1}{R_1(\varphi)^2} \left(\frac{dR_1(\varphi)}{d\varphi} \right)^2 & -\frac{(k-1)}{k} \frac{1}{R_1(\varphi)} \frac{dR_1(\varphi)}{d\varphi} & 0 \\ -\frac{(k-1)}{k} \frac{1}{R_1(\varphi)} \frac{dR_1(\varphi)}{d\varphi} & 1/k & 0 \\ 0 & 0 & \frac{1}{k} \left(\frac{\rho'}{R_1(\varphi)} \right)^{2/k-2} \end{pmatrix}, \quad (3.22)$$

in the region $R_1(\varphi) \leq \rho' \leq R_2(\varphi)$, and

$$\mu' = \begin{pmatrix} 1 & 0 & 0 \\ 0 & 1 & 0 \\ 0 & 0 & \left(\frac{r_2}{r_1} \right)^{2/k-2} \end{pmatrix}, \quad (3.23)$$

in the region $\rho' > R_2(\varphi)$.

In cases with translational symmetry along the z -axis, only the left-upper 2x2 minors of the permeability tensors have to be considered. Thus, the effect of the space transformation presented in Fig. 3.7b can be achieved by a single magnetic material with the relative magnetic permeability given by Eq. (3.22) placed in the region $R_1(\varphi) < \rho' < R_2(\varphi)$. Interestingly, since the shell boundaries $R_1(\varphi)$ and $R_2(\varphi)$ fulfill $R_2(\varphi) = (r_2/r_1)R_1(\varphi)$, the left-upper 2x2 minor of the permeability in Eq. (3.22) is equivalent to that in Eq. (3.5) for the concentrating shell. This indicates that a long shell with the permeability designed for concentrating external magnetic fields inside its hole also expels towards its exterior magnetic fields created inside its hole. This property, known for cylindrical concentrating shells [74], is therefore extended to the case of arbitrarily shaped long concentrators.

The shell achieving the maximum field concentration, which according to Eqs. (3.7) and (3.5) was found to be the shell with $k \rightarrow \infty$, is also the shell exhibiting the maximum field expulsion. This result can be intuitively understood by analysing the space transformation in Eqs. (3.19) and (3.20) bearing in mind the relation between the parameter k and the shell radii [Eq. (3.21)]. When k is minimum, $k \rightarrow 1$, $R_0(\varphi) \rightarrow R_2(\varphi)$ and the space is barely expanded. In contrast, when $k \rightarrow \infty$, $R_0(\varphi) \rightarrow R_1(\varphi)$ and all the space in the shell region is expanded towards its exterior. Because the transformation with $k \rightarrow \infty$ is the one expelling the largest amount of space, it is also the one resulting in the largest field expulsion.

One can apply the transformation optics theory to find out which is the field distribution outside a shell with $k \rightarrow \infty$ when there is a magnetic source located inside its hole. According to Eqs. (1.22), (3.19) and (3.21), the magnetic field in the external region is transformed as

$$\mathbf{H}'(\rho', \varphi') = \left(\frac{r_2}{r_1}\right)^{1/k-1} \mathbf{H}\left(\left(\frac{r_2}{r_1}\right)^{1/k-1} \rho', \varphi'\right), \quad \rho' \in [R_2(\varphi), \infty). \quad (3.24)$$

As an example, consider a long dipole of magnetic moment \mathbf{m} placed inside the shell hole; at $\rho = \rho_0 < R_1$ and $\varphi = \varphi_0$. The field in the external region exactly corresponds to the field created by another magnetic dipole, with magnetic moment

$$\mathbf{m}' = \left(\frac{r_2}{r_1}\right)^{1-1/k} \mathbf{m}, \quad (3.25)$$

located at

$$\rho'_0 = \left(\frac{r_2}{r_1}\right)^{1-1/k} \rho_0, \quad \varphi'_0 = \varphi_0. \quad (3.26)$$

Since $r_2 > r_1$, the field outside the shell corresponds to the field of a magnified dipole. Some examples of this result are illustrated in Fig. 3.8 assuming a shell with $k \rightarrow \infty$. In this limit, the components of the shell relative permeability tend to $\mu_{\rho\rho} \rightarrow \infty$, $\mu_{\varphi\varphi} \rightarrow 0$ and $\mu_{\rho\varphi} = \mu_{\varphi\rho} \rightarrow \frac{1}{R_1(\varphi)} \frac{dR_1(\varphi)}{d\varphi}$. Same as for the concentrating shell with $k \rightarrow \infty$ (Fig. 3.2), numerical calculations show that the off-diagonal components of the permeability can be neglected.

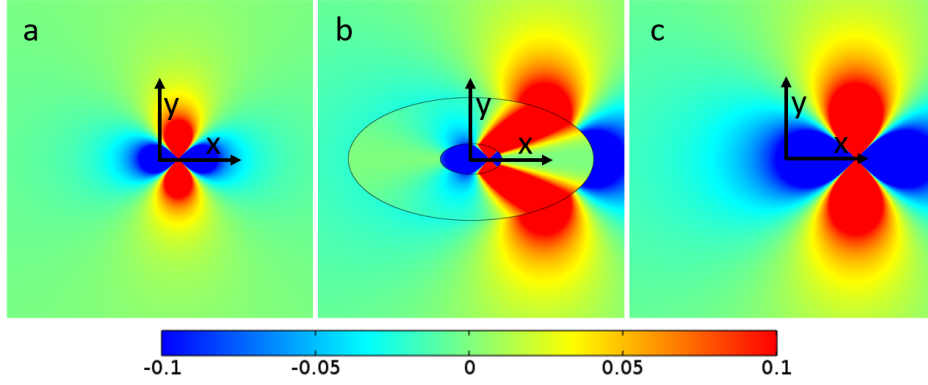


Figure 3.8: Numerical calculations of B_y normalized to $\mu_0 m/a^2$ in three different configurations. (a) A long (along the z -direction) magnetic dipole with magnetic moment per unit length $\mathbf{m} = m\mathbf{u}_z$. (b) The dipole in (a) surrounded by a long shell with elliptic cross-section with relative permeability $\mu_{\rho\rho} = 10^5$, $\mu_{\varphi\varphi} = 10^{-5}$, and $\mu_{\rho\varphi} = \mu_{\varphi\rho} = 0$. The inner and the outer axes of the elliptic shell are a and $a/2$, and $4a$ and $2a$, respectively. The distance between the dipole and the center of the shell is $\rho_0 = 3a/5$. (c) A long magnetic dipole with magnetic moment $\mathbf{m} = 4m\mathbf{u}_y$ placed at a distance $4\rho_0$ from the center of the shell in (b).

3.2.2 Surrounding magnetic materials by magnetic concentrators

Consider a magnetic material of linear, isotropic, and homogeneous permeability μ in the presence of an applied magnetic field. The applied field magnetizes the material, which responds to the field creating a magnetic field distortion that depends on its permeability and geometry and on the applied field. In this section, we demonstrate that surrounding a magnetic material with a concentrating shell results in an amplification of the material response. One could foresee this result by bearing in mind the concentration and expulsion properties of the shell. Interestingly, by applying the transformation optics technique, one does not only find that the material response is amplified by the shell, but also that the amplified response is equivalent to the response of an enlarged magnetic material with the same permeability and shape as the original one. Similar devices have been derived for electromagnetic waves, usually involving materials with negative constitutive parameters [9, 91, 92, 93, 94, 95].

For this study, consider a long shell of arbitrary cross-section with internal boundary $R_1(\varphi)$ and external boundary $R_2(\varphi)$ with the anisotropic permeability tensor in Eq. (3.5). The shell shapes the applied magnetic field as if the space had been transformed according to Eqs. (3.1) and (3.2). A sketch of the transformed space due to the use of a concentrating shell with $k \rightarrow \infty$ is shown in Fig. 3.9a. Consider now a magnetic material of permeability μ and cross-section area S_M placed inside the shell hole (blue object in Fig. 3.9a). If the origin of coordinates is set at the center of the hole, the position of the center of the material is defined by $\rho = \rho_M$ and $\varphi = \varphi_M$.

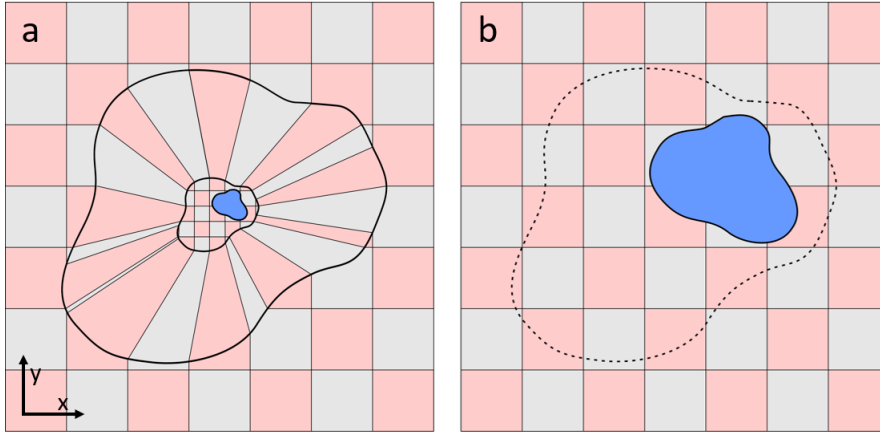


Figure 3.9: (a) Sketch of a magnetic material (blue) in the region $\rho' < R_1(\varphi)$ when the space is transformed according to Eqs. (3.1) and (3.2) with $k \rightarrow \infty$. The shell effectively increases the size of the material, as sketched in (b).

Using the space transformation in Eq. (3.1), one finds that the material surrounded by the concentrating shell (Fig. 3.9a) shapes externally applied magnetic fields in the same way as a material with cross-section

$$S'_M = \left(\frac{r_2}{r_1}\right)^{1-1/k} S_M, \quad (3.27)$$

with its center at

$$\rho'_M = \left(\frac{r_2}{r_1}\right)^{1-1/k} \rho_M, \quad \varphi'_M = \varphi_M, \quad (3.28)$$

as illustrated in Fig. 3.9b. According to the transformation optics theory, because the space occupied by the material is effectively transformed by the concentrating shell, the material permeability has to be transformed as indicated by Eq. (3.4). However, when only the first 2x2 minor of the permeability tensor has physical relevance, as occurs in magnetostatics for applied fields with translational symmetry along the z -axis, the transformed permeability is equivalent to the original one. This demonstrates that magnetic concentrators can be employed to effectively enlarge magnetic materials without modifying their magnetic properties. The magnification is always bounded: the magnified object cannot reach the shell external region $\rho > R_2(\varphi)$. Shells with $k \rightarrow \infty$ achieve the largest material magnification. Some examples of the magnification provided by concentrators with $\mu_{\rho\rho} \rightarrow \infty$ and $\mu_{\varphi\varphi} \rightarrow 0$ are presented in Fig. 3.10. The magnetic field outside a concentrator covering a magnetic material (Figs. 3.10a and c) corresponds to the field that an uncovered material with the same properties as the covered material but enlarged cross-section would create (Figs. 3.10b and d). The field distributions are only equivalent in the region $\rho > R_2(\varphi)$. Also, the magnetic field in the volume of the coated material is larger than the field in the volume of the enlarged materials due to the shell ability to concentrate magnetic fields.

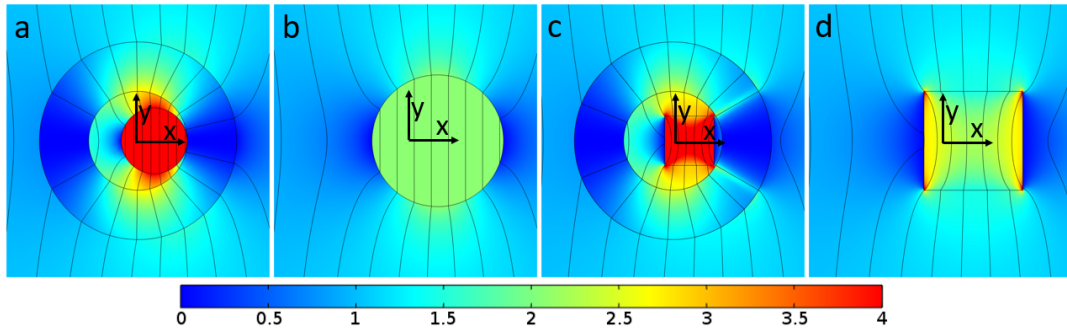


Figure 3.10: Numerical calculations of the magnetic induction field lines and, in colors, $B_y/(\mu_0 H_0)$ for a uniform magnetic field H_0 applied along the y -direction to four long (along z) objects. (a) A ferromagnetic ($\mu = 10^5$) cylinder of radius R surrounded by a cylindrical shell with internal radius $R_1 = 1.5R$, external radius $R_2 = 2R_1$, and permeability $\mu_{\rho\rho} = 10^5$ and $\mu_{\varphi\varphi} = 10^{-5}$. The cylinder is displaced a distance $R/2$ from the center of the shell (origin). In (b) a ferromagnetic cylinder of radius $R(R_2/R_1)$ at a distance $(R/2)(R_2/R_1)$ from the origin. In (c) and (d), same as in (a) and (b), respectively, for a long ferromagnetic material with squared cross-section.

3.2.3 Surrounding short magnetic materials by short concentrators

Long magnetic materials with arbitrary cross-section surrounded by long concentrators have been shown to respond to perpendicularly applied fields in the same way as magnified materials with the same permeability and larger cross-section. In this section, these results are extended to the case of short cylinders surrounded by short cylindrical concentrators. As sketched in Fig. 3.11, we consider a uniform magnetic field \mathbf{H}_0 applied along the cylinder plane. Numerical calculations demonstrate that the concentration provided by short cylindrical shells is lower than that for the infinitely long shells [86, 87], but this does not considerably worsen the concentrators ability to magnify ferromagnetic materials.

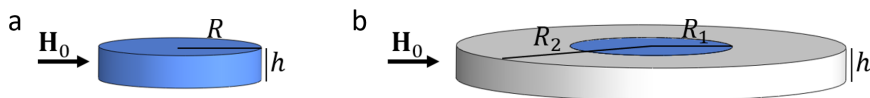


Figure 3.11: Sketches of (a) a disk of radius R and height h in a uniform field \mathbf{H}_0 and (b) the disk in (a) surrounded by a cylindrical concentrator with internal radius $R_1 = R$, external radius R_2 , and height h .

Consider first a long (along the z -direction) ferromagnetic cylinder of radius R surrounded by a long concentrator with internal radius $R_1 = R$, external radius R_2 , and relative permeability $\mu_{\rho\rho} \rightarrow \infty$ and $\mu_{\varphi\varphi} \rightarrow 0$ in a uniform field \mathbf{H}_0 applied in the y -direction. Results in Figs. 3.12a-c show that the magnetic response of the material is equivalent to that of a radially enlarged long cylinder with radius R_2 .

Consider now a ferromagnetic cylinder of radius R and height h surrounded by a cylindrical concentrating shell with internal radius $R_1 = R$, external radius R_2 , and height h , as sketched in Fig. 3.11b. Figures 3.12d-i show that even though the concentrator height h is finite, the magnification ability demonstrated for long concentrators is maintained. The field distribution in the exterior of the coated disk (Figs. 3.12e and h) approximates well the field distribution outside a magnified disk of radius R_2 and height h (Figs. 3.12f and i). Thus, short concentrators can radially enlarge magnetic materials without modifying their height.

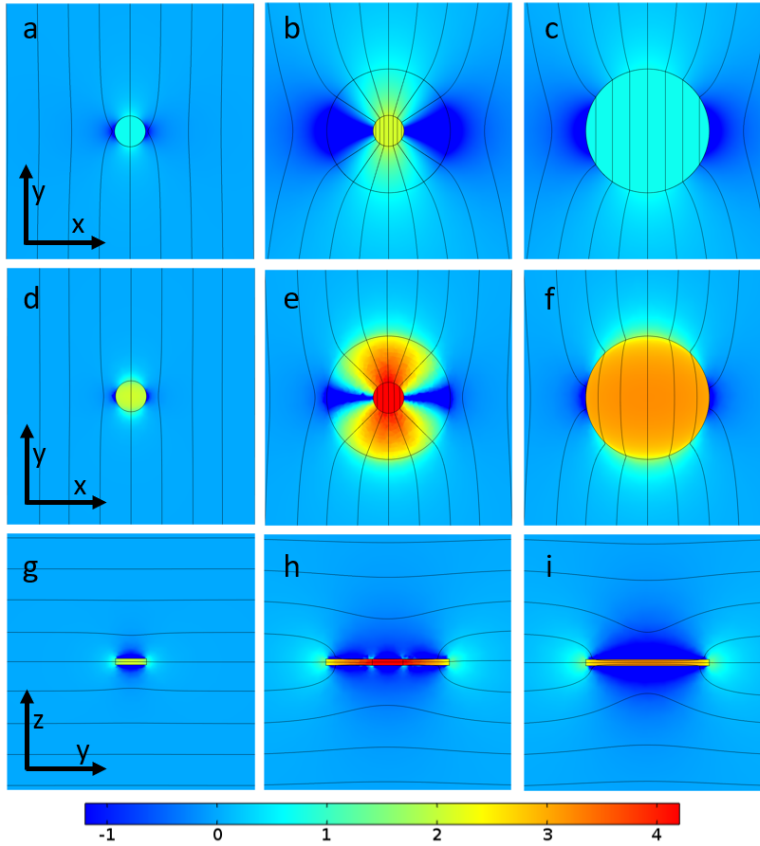


Figure 3.12: Numerical calculations of the magnetic induction field lines and, in colors, $\log[B_y/(\mu_0 H_0)]$ for a uniform magnetic field H_0 applied along the y -direction. In (a) a long (along z , $h \rightarrow \infty$) ferromagnetic ($\mu = 10^5$) cylinder of radius R . In (b) the cylinder in (a) surrounded by a long cylindrical concentrator with internal radius $R_1 = R$, external radius $R_2 = 4R$, and permeability $\mu_{\rho\rho} = 10^5$ and $\mu_{\varphi\varphi} = 10^{-5}$. In (c) a long ferromagnetic cylinder of radius $4R$. Panels (d)-(f) show the same results as panels (a)-(c) for cylinders of finite height $h = 0.4R$. Images are taken at the cylinders mid-plane ($z = 0$). Panels (g)-(i) show the field distributions corresponding to the cylinders in (d)-(f) in the plane $x = 0$. The magnetic induction averaged over the ferromagnetic cylinder volume, $B_y^{\text{vol}}/(\mu_0 H_0)$, is (a) 2, (b) 8.12, (c) 2.03, (d) 7.09, (e) 71.9, and (f) 20.63.

For some applications, such as for enhancing the sensitivity of sensors including ferromagnetic elements, it may be interesting to compare the magnetic induction in the volume of a ferromagnetic cylinder when covered by a concentrator to the magnetic induction in the volume of the same cylinder when uncovered. Since the magnetic induction in the volume of short ferromagnetic cylinders is not uniform, we consider the magnetic induction averaged over the cylinder volume, which can be written as [96]

$$B^{\text{vol}} = \frac{\mu_0 H_0}{N_m}. \quad (3.29)$$

N_m is the magnetometric demagnetizing factor, defined as $N_m = -H_d^{\text{vol}}/M^{\text{vol}}$, where H_d^{vol} and M^{vol} are the demagnetizing field \mathbf{H}_d and the magnetization \mathbf{M} averaged over the entire volume of the ferromagnetic cylinder. N_m and, thus, B^{vol} strongly depend on the cylinder aspect ratio. In the limit of long cylinders, $h/R \rightarrow \infty$, $N_m \rightarrow 1/2$ and $B^{\text{vol}} \rightarrow 2\mu_0 H_0$ (Figs. 3.12a and c). The lower the material aspect ratio h/R , the lower N_m , which results in a larger B^{vol} [96]. For example, a cylinder of aspect ratio $h/R = 0.4$ exhibits $B^{\text{vol}} \approx 7.1\mu_0 H_0$ (Fig. 3.12d) and a cylinder of aspect ratio $h/R = 0.1$ $B^{\text{vol}} \approx 20.7\mu_0 H_0$ (Fig. 3.12f).

Consider the case of a ferromagnetic cylinder surrounded by a cylindrical concentrator. In the limit of long materials, the concentrator magnifies the cylinder radius, but the aspect ratio h/R and N_m are barely reduced because $h \rightarrow \infty$. Therefore, the average magnetic induction in the volume of a long magnified cylinder, B_M^{vol} , is the same as that of the original cylinder, B_0^{vol} (compare Figs. 3.12c and a). In contrast, when the material is short, the radius enlargement leads to a substantial reduction of the aspect ratio h/R and therefore $B_M^{\text{vol}} > B_0^{\text{vol}}$ (compare Figs. 3.12f and d). The magnetic induction averaged over the whole volume occupied by the ferromagnetic cylinder surrounded by a concentrator is equivalent to B_M^{vol} because the magnetic field attraction achieved by the coated cylinder is the same as that of the magnified cylinder (compare Figs. 3.12b, e, and h to Figs. 3.12c, f and i, respectively).

Bearing in mind these properties, we can finally compare the average magnetic induction in the volume of a ferromagnetic cylinder covered by a concentrator, B_C^{vol} , to the average magnetic induction in the volume of the same cylinder when uncovered, B_0^{vol} . Long concentrators radially direct all the magnetic induction field lines that reach their volume towards their hole, achieving $B_C^{\text{vol}}/B_M^{\text{vol}} = R_2/R_1$ [Eq. (3.7), Figs. 3.12b and c]. This is approximately maintained when considering short concentrators (Figs. 3.12e and f). Because long concentrators fulfill $B_M^{\text{vol}} = B_0^{\text{vol}}$, the magnetic induction concentration ratio $B_C^{\text{vol}}/B_0^{\text{vol}}$ they achieve is R_2/R_1 . In contrast, short concentrators achieve a stronger concentration ratio, $B_C^{\text{vol}}/B_0^{\text{vol}} > R_2/R_1$, because they fulfill $B_M^{\text{vol}} > B_0^{\text{vol}}$. Numerical calculations for a shell radii ratio $R_2/R_1 = 4$ give a concentration ratio $B_C^{\text{vol}}/B_0^{\text{vol}} \approx 4$ for the case $h/R \rightarrow \infty$ (Figs. 3.12a and b) and $B_C^{\text{vol}}/B_0^{\text{vol}} \approx 10$ for the case $h/R = 0.4$ (Figs. 3.12d and e).

3.2.4 Realizing magnification shells with metamaterials

Metamaterials consisting of alternating ferromagnetic and perfect diamagnetic pieces have been shown in Sec. 3.1.3 to effectively reproduce the properties of magnetic concentrators with extremely large radial component of the permeability and extremely low angular one (Fig. 3.13b). Simplified metamaterials consisting solely of ferromagnetic pieces work at room temperature, but lead to lower concentration ratios than those combining ferromagnetic and perfect diamagnetic materials and leave the applied field slightly distorted (Fig. 3.13c) [86, 83]. Similar results are obtained when discretizing the metamaterial using solely perfect diamagnetic pieces (Fig. 3.13d).

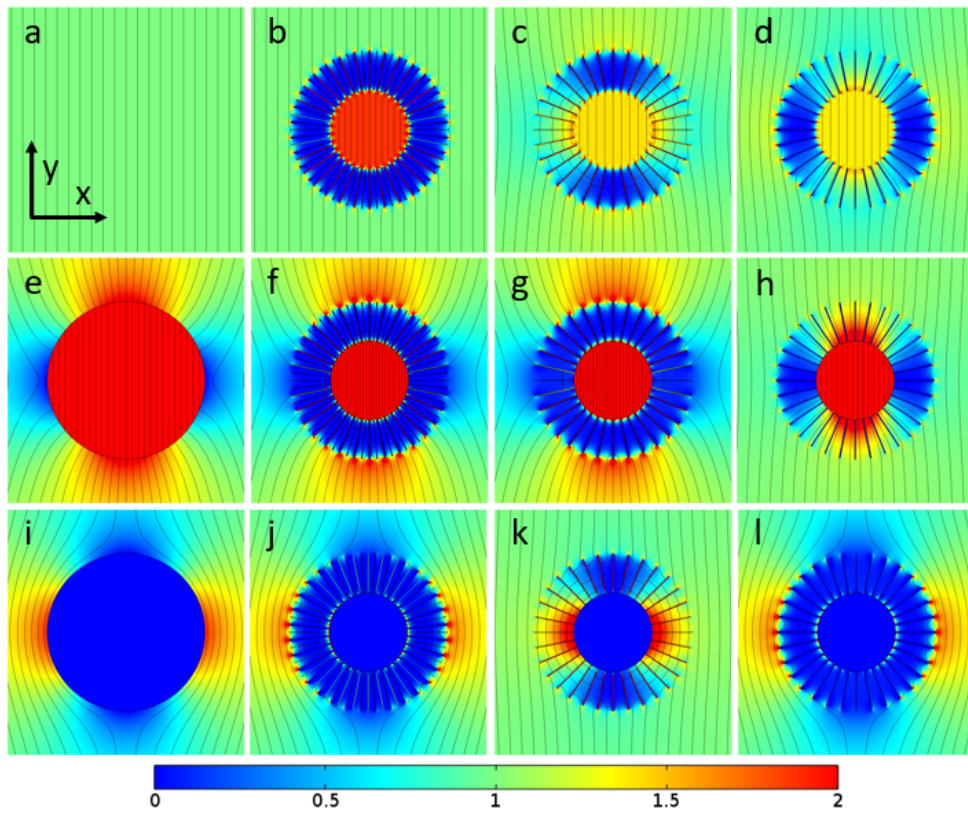


Figure 3.13: Numerical calculations of the magnetic induction field lines and, in colors, $B_y/(\mu_0 H_0)$ for a uniform magnetic field H_0 applied along the y -direction. In (a) empty space. In (b) a long cylindrical shell of internal and external radii R and $2R$, respectively, made of an alternation of 32 ferromagnetic ($\mu = 10^5$) and 32 perfect diamagnetic ($\mu = 10^{-5}$) bars. In (c) the same shell as in (b) without the perfect diamagnetic pieces. In (d) the same as in (b) without the ferromagnetic pieces. In (e) and (i) a long ferromagnetic ($\mu = 10^5$) and a long perfect diamagnetic ($\mu = 10^{-5}$) cylinder of radius $2R$, respectively. In (f), (g) and (h), the shells in (b), (c) and (d) cover a long ferromagnetic ($\mu = 10^5$) cylinder of radius R . In (j), (k) and (l), the shells in (b), (c) and (d) cover a long perfect diamagnetic ($\mu = 10^{-5}$) cylinder of radius R .

Numerical calculations demonstrate that a metamaterial shell alternating both materials also emulates well the properties of a long concentrator with $\mu_{\rho\rho} \rightarrow \infty$ and $\mu_{\varphi\varphi} \rightarrow 0$ surrounding a magnetic material of permeability μ . As an example, Figs. 3.13f and j show how this metamaterial shell magnifies the response of a ferromagnetic and a perfect diamagnetic cylinder, respectively, to make it approximately equivalent to that of a larger cylinder, depicted in Figs. 3.13e and i, respectively. In general, metamaterial devices consisting solely of ferromagnetic or perfect diamagnetic pieces exhibit a worse magnifying performance than those combining both materials. Interestingly, when surrounding a paramagnetic or a ferromagnetic material ($\mu > 1$), the discretization with ferromagnetic pieces emulates the shell much better than the discretization with perfect diamagnetic pieces. When covering diamagnetic materials ($\mu < 1$), it is the other way around. Figures 3.13g, h, k, and l illustrate this effect for the limit cases of a shell covering a ferromagnetic ($\mu \rightarrow \infty$) and a perfect diamagnetic ($\mu \rightarrow 0$) material. When covering a ferromagnetic material, a concentrator consisting of ferromagnetic bars solely (Fig. 3.13g) can barely be distinguished from the concentrator combining ferromagnetic and perfect diamagnetic pieces (Fig. 3.13f). In contrast, a concentrator consisting of perfect diamagnetic bars solely (Fig. 3.13h) is not able to magnify the ferromagnetic material. On the contrary, when covering a perfect diamagnetic material, the discretization with perfect diamagnetic bars is the one leading to a magnified object (Figs. 3.13k and l).

When the hole of the shell is empty, perfect diamagnetic bars are required for avoiding magnetic field lines from following an angular path and leaving the material without having reached the hole (Fig. 3.13c), and ferromagnetic bars are required for attracting the applied magnetic field towards the shell volume (Fig. 3.13d). In contrast, when there is a ferromagnetic material inside the hole, perfect diamagnetic bars are not required because the attraction provided by the inner material and the ferromagnetic bars is enough to guarantee that the magnetic field lines that reach the shell are directed towards the hole (Fig. 3.13g). Therefore, the magnification of ferromagnets does not require superconductors nor cryogenics. The response of a ferromagnetic material cannot be magnified by perfect diamagnetic bars solely because the expulsion of magnetic field lines provided by the diamagnetic shell reduces the attraction of the ferromagnetic core instead of increasing it (Fig. 3.13h). Similar arguments explain why a perfect diamagnetic material cannot be magnified by a shell consisting of ferromagnetic pieces solely (Fig. 3.13k). Finally, when covering a perfect diamagnetic material, perfect diamagnetic bars are enough to guarantee that magnetic induction field lines do not reach the shell volume, which results in a magnification of the diamagnet (Fig. 3.13l). These results provide a strategy for achieving the same response as that resulting from a bulk ferromagnetic or a perfect diamagnetic material using a much lower amount of material.

3.3 Cloaking shells to make magnetic sensors undetectable

Magnetism is measured by magnetic sensors or magnetometers, which can measure the magnetization of a magnetic material, such as a ferromagnet, or the direction and strength of a magnetic field. Because magnetism is present in a wide range of technologies, such as biomedicine, geophysics, or space exploration [97, 98, 99], the development and the improvement of magnetic sensors is an important active line of research. There are several types of magnetic sensors, which can be classified according to the physical principle that underlies their ability to measure. Some of the most employed sensors are pick-up coils, fluxgate sensors [100], magnetoresistive sensors [101, 102], Hall-effect sensors [103], magnetic tunnel junctions [104], and SQUIDS [105].

The extreme anisotropic concentrating shells presented above can be applied as a general tool for enhancing the sensitivity of magnetic sensors, as sensors surrounded by these shells would be able to detect lower magnetic fields than when uncoated [74, 83]. In many cases, there is an analytic relation between the field inside the concentrator and the applied field and it is possible to derive the applied field from measurements performed by the coated sensor. This could benefit applications requiring the detection of tiny magnetic fields, as occurs in a wide range of biomedical techniques, such as in magnetoencephalography or ultra-low-field magnetic resonance imaging [106, 107, 108, 109]. In some cases, however, what limits the sensor applicability is not its sensitivity, but its detectability, which depends on the distortion it creates as a response to the probing field. This distortion may be an important drawback in applications dealing with precise field distributions that require non-invasive sensing, or in applications involving dense packaging of sensors, since the distortion created by each sensor may affect the measurements of the others, for example [110]. If a sensor was covered by a concentrator, not only its sensitivity, but also its distortion would be magnified, as the concentrator would expel the field distortion caused by the sensor towards its exterior. For example, the distortion due to a sensor that includes ferromagnetic parts would be magnified by a concentrator because it would effectively enlarge the enclosed ferromagnetic materials, which results in a larger field attraction (Fig. 3.12).

Our goal in this section is to derive the properties of a magnetic shell able to render a magnetic sensor invisible, so that it is able to detect magnetic fields while being magnetically undetectable [111]. Our ideas are based on the strategy proposed in [112] for cloaking electromagnetic sensors or antennas. After this proposal several cloaks for electromagnetic sensors [112, 113, 114, 115, 116, 117], acoustic sensors [118, 119] and multiphysical field sensors [120] were discussed, but the problem of cloaking magnetic sensors remained unsolved. Opposite to the concentrating shells, the cloaking shell we propose strongly reduces the distortion of a sensor at the cost of decreasing its sensitivity. We show that, under certain conditions, it is possible to exactly cancel a sensor distortion without completely losing its ability to measure the applied field. This contrasts with the case of electromagnetic invisible sensors, which, due to the optical theorem, can only absorb and measure the field if their scattering cross-section is not zero [121].

3.3.1 Cloaking spherical sensors in uniform fields

Magnetic sensors usually benefit from the properties of ferromagnetic materials [98]. For example, magnetoresistive sensors measure the fields thanks to the dependence of the ferromagnets electric resistance on externally-applied magnetic fields. In other cases, as in Hall-effect sensors, ferromagnets are employed to increase the sensor sensitivity; thanks to their ability to attract magnetic fields, ferromagnetic pieces can be properly arranged to magnify the field a sensor receives [122]. Because the distortion caused by magnetic sensors is mainly due to their ferromagnetic parts, our goal of cloaking a magnetic sensor can be redefined as cancelling the distortion created by a ferromagnetic material. For this reason, we model our sensor as a linear, isotropic, and uniform ferromagnetic material with permeability $\mu \rightarrow \infty$.

For simplicity, we start by considering a spherical sensor in the presence of a uniform magnetic field \mathbf{H}_0 . The sphere becomes magnetized in the direction of the applied field, with a uniform magnetization $\mathbf{M}^{\text{FM}} = 3\mathbf{H}_0$ [2]. The distortion it creates is shown in Fig. 3.14a. A first strategy for rendering a spherical sensor undetectable could be that of surrounding the sensor by one of the already known magnetic invisibility cloaks [69, 71, 123]. Such cloaks, however, include an inner perfect diamagnetic layer that prevent any external magnetic field line from entering inside the region it encloses, as shown in Fig. 3.14b. A sensor surrounded by one of these cloaks would be magnetically isolated and unable to measure external fields. Our goal of making a magnetic sensor undetectable requires, therefore, the design of a different kind of cloaking shell. Based on the scattering cancellation cloak presented in [112], the cloaking shell we propose cancels the sphere distortion while enabling the magnetic field to reach the sphere, so that the sensor is still able to detect the applied field, as shown in Fig. 3.14c [84].

Consider a spherical sensor of radius R surrounded by a spherical shell of internal radius $R_1 = R$ and external radius $R_2 > R_1$, with linear, homogeneous, and isotropic relative permeability μ_1 . In this case, the magnetic field everywhere can be obtained from a magnetic scalar potential ϕ that fulfills the Laplace equation and the magneto-static boundary conditions. In this way, one finds that the coated sensor distorts, in general, the applied field. Interestingly, there is a permeability value ($0 < \mu_1 < 1$), which depends on the shell geometry as

$$\mu_1 = 1 - \frac{3}{(R_2/R_1)^3 + 2}, \quad (3.30)$$

that leads to a zero field distortion. This demonstrates that it is possible to render a spherical sensor exactly undetectable. In order for the sensor to be able to measure the applied field, the coated sphere magnetization, which gives a measurement of the field it receives, \mathbf{M}_c^{FM} , must be different from zero. By taking into account the permeability in Eq. (3.30) one finds

$$\mathbf{M}_c^{\text{FM}} = \frac{3(R_2/R_1)^3}{(R_2/R_1)^3 + 2} \mathbf{H}_0. \quad (3.31)$$

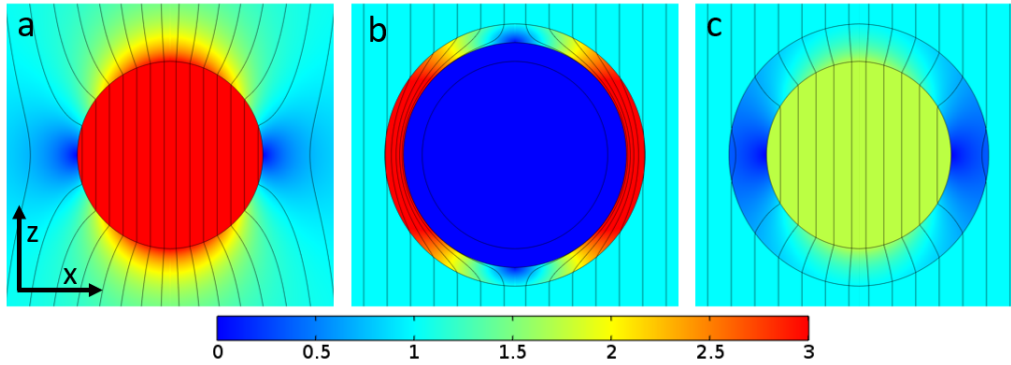


Figure 3.14: Numerical calculations of the magnetic induction field lines and, in colors, $B_z/(\mu_0 H_0)$ for a uniform magnetic field H_0 applied along the z -direction to three objects. In (a) a ferromagnetic ($\mu = 10^5$) sphere of radius R . In (b) same sphere surrounded by a bilayer cloak consisting of an inner perfect diamagnetic layer ($\mu = 10^{-5}$) with internal radius R and external radius $R_1 = 1.2R$ and a second layer of permeability $\mu = 3.55$, internal radius R_1 , and external radius $R_2 = 1.4R$. In (c) same sphere as in (a) surrounded by a shell with internal radius $R_1 = R$, external radius $R_2 = 1.4R$, and permeability $\mu = 0.368$.

As \mathbf{M}_c^{FM} is different from zero for any shell radii ratio R_2/R_1 , the cloaked sensor is still able to receive magnetic field lines (Fig. 3.14c). The magnetization of the coated sphere is lower than that of the bare sphere, indicating that the sensor sensitivity is reduced by the presence of the cloak. The larger the external radius of the shell, $R_2 \rightarrow \infty$, the larger the sensor sensitivity, since \mathbf{M}_c^{FM} tends to \mathbf{M}^{FM} .

In this way, the magnetic sensor is able to detect magnetic fields while being magnetically undetectable. From this apparent asymmetry, a fundamental question arises as to whether magnetostatic reciprocity holds in this situation [124]. The evaluation of the magnetostatic reciprocity condition requires the consideration of two independent magnetic field sources. For example, two dipoles of magnetic moment \mathbf{m}_1 and \mathbf{m}_2 fulfill the reciprocity condition when the field created by the dipole 1 at the position of the dipole 2, $\mathbf{B}_1(\mathbf{r}_2)$, and the field created by the dipole 2 at the position of the dipole 1, $\mathbf{B}_2(\mathbf{r}_1)$, fulfill $\mathbf{m}_2 \cdot \mathbf{B}_1(\mathbf{r}_2) = \mathbf{m}_1 \cdot \mathbf{B}_2(\mathbf{r}_1)$. In order to understand why it is possible to exactly cloak a magnetic sensor without breaking the magnetostatic reciprocity condition, one can regard a cloaked sensor as the superposition of two different configurations. First, the cloaking shell in the presence of the externally applied magnetic field (Fig. 3.15a) and, second, the cloaking shell surrounding a sphere with magnetization \mathbf{M}_c^{FM} (Fig. 3.15b). This shows that the behaviour of the cloaking shell is symmetric, since the field generated by the external magnetic field source can reach the sphere and the field generated by the sphere can reach the external region. It is only when one takes into account the field in the external region due to both magnetic field sources that the external field distortion is equal to zero (Fig. 3.15c).

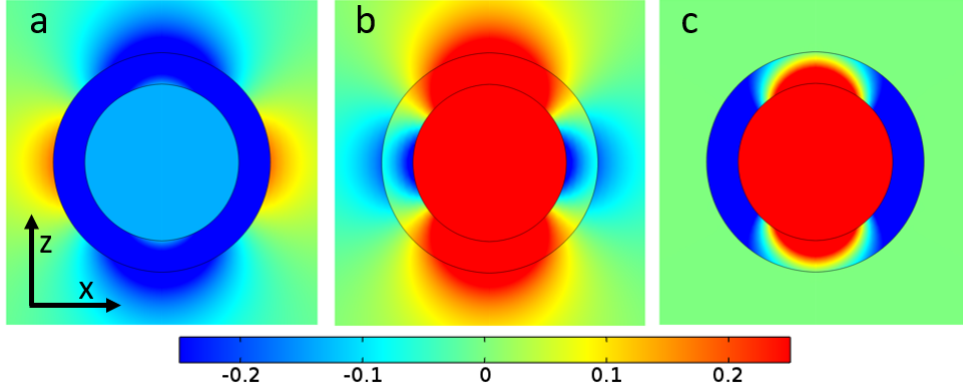


Figure 3.15: (a) Numerical calculations of the field distortion $(B_z/\mu_0 - H_0)/H_0$ when a uniform magnetic field H_0 is applied along the z -direction to a spherical shell of internal radius $R_1 = R$, external radius $R_2 = 1.4R$, and permeability $\mu = 0.368$. (b) Numerical calculations of B_z/μ_0 for a sphere of radius R and magnetization $\mathbf{M}_c^{\text{FM}} = 1.735\mathbf{H}_0$ surrounded by the same spherical shell as in (a). (c) Numerical calculations of the field distortion $(B_z/\mu_0 - H_0)/H_0$ when a uniform magnetic field H_0 applied to the coated sphere in (b). The cloaked sphere in (c) does not distort the external field distribution.

For practical applications it would be more interesting to consider thin cloaking shells, not only in terms of material savings, but also because it can result in simpler metamaterial devices. To this end, it is convenient to study which is the sensitivity of magnetic sensors cloaked by thin spherical shells. Consider that there is a centered air gap between the ferromagnetic sphere and the spherical shell. In this case, the internal radius of the shell is $R_1 > R$ and the external radius is R_2 . The solution of the magnetostatic Maxwell equations gives that the permeability μ_1 to render the ferromagnetic sphere magnetically undetectable is

$$\mu_{1,\text{GAP}} = \frac{-(R_1/R)^6 - 4(R_2/R)^3 + (R_1/R)^3 [(R_2/R)^3 - 5] + 3F}{4[(R_1/R)^3 - 1][(R_2/R)^3 - (R_1/R)^3]}, \quad (3.32)$$

where $F = \sqrt{(R_1/R)^3 [8(R_2/R)^3 + (R_1/R)^3 ((R_1/R)^3 - (R_2/R)^3 + 1)^2]}$. As in the gapless case [$R_1 - R = 0$, Eq. (3.30)], the cloaking shell is diamagnetic ($\mu_{1,\text{GAP}} < 1$) to compensate for the attractive response of the sphere. The magnetization of the ferromagnetic sphere surrounded by this shell is

$$\mathbf{M}_{c,\text{GAP}}^{\text{FM}} = \frac{3(R_1/R)^3 [(R_2/R)^3 + (R_1/R)^3 + 1] - 3F}{2[(R_1/R)^6 + (R_1/R)^3 - 2]} \mathbf{H}_0, \quad (3.33)$$

which is always larger than that of the gapless case [$R_1 - R = 0$, Eq. (3.31)], for fixed radii R and R_2 . In Fig. 3.16, the magnetization $\mathbf{M}_{c,\text{GAP}}^{\text{FM}}$ is plotted as a function of the normalized external radius R_2/R and the normalized air gap $(R_1 - R)/R$. The analysis

of this figure leads to two interesting results. First, the larger the external radius of the shell, the higher the sensitivity of the sensor. This results from the relation between the shell permeability, $\mu_{1,\text{GAP}}$, and the shell geometry. The larger the shell, the less extreme (closer to 1) the permeability $\mu_{1,\text{GAP}}$ is. Therefore, shells with low $R_2/R \rightarrow 1$ exhibit an extremely low permeability and tend to shield the applied field, $\mathbf{M}_{c,\text{GAP}}^{\text{FM}} \rightarrow 0$, while shells with $R_2/R \rightarrow \infty$ exhibit a relative permeability close to 1 and barely reduce the field reaching the sphere, $\mathbf{M}_{c,\text{GAP}}^{\text{FM}} \rightarrow \mathbf{M}^{\text{FM}}$. Second, for a fixed R_2/R , the sensor sensitivity hardly depends on the air gap that is left between the sphere and the shell.

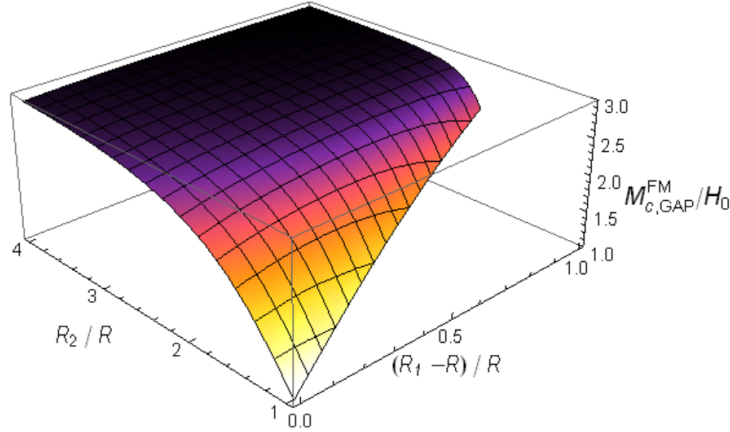


Figure 3.16: Modulus of the magnetization normalized to the applied field H_0 for a ferromagnetic sphere of radius R covered by a spherical shell extending from $R_1 \geq R$ to R_2 with the permeability $\mu_{1,\text{GAP}}$ in Eq. (3.32) plotted as a function of the shell external radius R_2 and the air gap $R_1 - R$, both normalized to R .

3.3.2 Generalization to non-spherical sensors and inhomogeneous fields

Consider now the ferromagnetic sphere of radius R in the presence of an inhomogeneous applied magnetic field. In this situation, the sphere responds to the applied field creating not only a dipolar response, as for uniform fields, but a multipolar one. As an example, Figs. 3.17a and b show how a sphere distorts the field created by a dipolar source. Interestingly, a cloaking shell with permeability μ_1 in Eq. (3.30) (without air gap) or permeability $\mu_{1,\text{GAP}}$ in Eq. (3.32) (with air gap) still cancels the dipolar term of the distortion the sphere creates. Since this is usually the leading term of the distortion (the other terms rapidly decrease with the distance from the material), the distortion of ferromagnetic spheres in inhomogeneous fields can be largely reduced by the proposed cloaking shell, as illustrated in Fig. 3.17c. If the goal is to reduce the distortion even further, one can add more layers to the cloaking device. The permeability of each layer can be designed to cancel a different term of the distortion multipolar expansion. The case of a cloaking shell consisting of two layers that cancel the dipolar and the quadrupolar terms of a sphere distortion is illustrated in Fig. 3.17d [84].

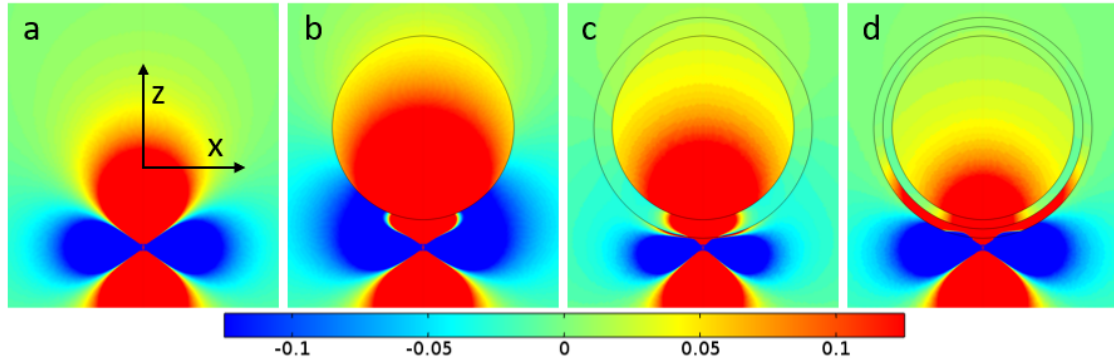


Figure 3.17: Numerical calculations of the normalized magnetic induction $B_z R^3 / (\mu_0 m)$ for a dipole of magnetic moment $\mathbf{m} = m \mathbf{u}_z$ displaced a distance $1.3R$ from the origin of coordinates in the presence of different magnetic materials. In (a) the dipole in empty space, in (b) the dipole in the presence of a centered ferromagnetic ($\mu = 10^5$) sphere of radius R , in (c) same as in (b) with the sphere covered by a spherical shell with internal radius $R_1 = R$, external radius $R_2 = 1.2R$, and permeability $\mu_1 = 0.195$, and in (d) same as in (b) with the sphere surrounded by a bilayer spherical shell with permeability $\mu_{1,b} = 0.0546$ (inner layer, extending from R to $1.1R$) and $\mu_{2,b} = 3.08$ (outer layer, extending from $1.1R$ to $1.2R$).

So far we have only considered spherical sensors, but sensors usually exhibit elongated shapes to provide stronger magnetic field attractions. The response of non-spherical materials is never merely dipolar, not even when the applied field is uniform. Even though the proposed cloaking shells cannot make non-spherical sensors exactly undetectable, they can largely reduce their distortion by cancelling its leading dipolar term [84].

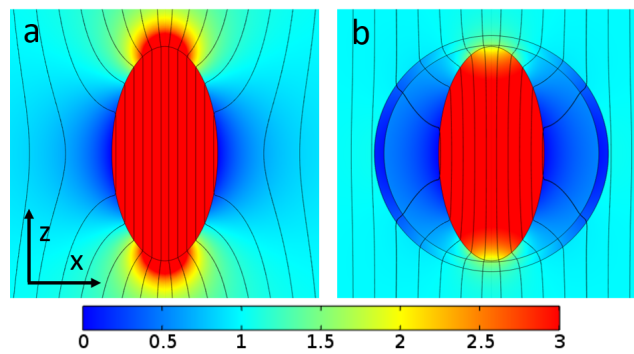


Figure 3.18: Numerical calculations of the magnetic induction field lines and, in colors, $B_z / \mu_0 H_0$ for a uniform magnetic field H_0 applied in the z -direction to (a) an ellipsoid with semiaxes $b/a = 1$ and $c/a = 2$ and permeability $\mu = 10^5$, and (b) the ellipsoid in (a) surrounded by a spherical shell with internal radius $R_1 = 2a$, external radius $R_2 = 2.2a$, and permeability $\mu_1 = 0.138$.

The required shell permeability can be derived by rewriting Eq. (3.32) in terms of the dipolar magnetic moment m it cancels. To this end, the sphere radius R must be substituted by $[m/(4\pi H_0)]^{1/3}$, which results from $m = M^{\text{FM}}V = 4\pi R^3 H_0$, where $M^{\text{FM}} = 3H_0$ is the modulus of the sphere magnetization and V its volume. Following this method, one can obtain, for example, the shell permeability that cancels the dipolar term of the distortion created by an ellipsoid, as illustrated in the example in Fig. 3.18.

3.3.3 Realizing the cloaking shell with metamaterials

The proposed shell for cloaking a sensor is linear, homogeneous, and isotropic, but it requires a precise value of the relative permeability lower than 1. Such diamagnetic permeabilities may not exist in nature, since most natural diamagnetic materials exhibit a relative permeability smaller but close to 1. Interestingly, one can design a magnetic metamaterial that effectively exhibits the required intermediate diamagnetic permeability $0 < \mu < 1$. These metamaterials can be realized by adequate arrangements of superconducting tapes, which behave as materials with $\mu \approx 0$ in magnetostatics [42, 43, 44, 45, 82]. This strategy for obtaining intermediate diamagnetic permeabilities has been experimentally demonstrated using both low-temperature and high-temperature superconductors [43, 82]. Numerical calculations in Fig. 3.19c demonstrate that a metamaterial diamagnetic shell made of perfect diamagnetic loops (Fig. 3.19a) largely reduces the distortion created by a ferromagnetic sphere in a uniform applied field. Compared to the ideal cloaking shell in Fig. 3.19b, the metamaterial shell slightly distorts the field due to its simple and coarse discretization. In a practical realization, the superconducting loops would need to include a cut such that each piece has a simple connected topology. Otherwise, the superconducting pieces would not behave as perfect diamagnetic materials and would not provide the desired cloaking effect [79].

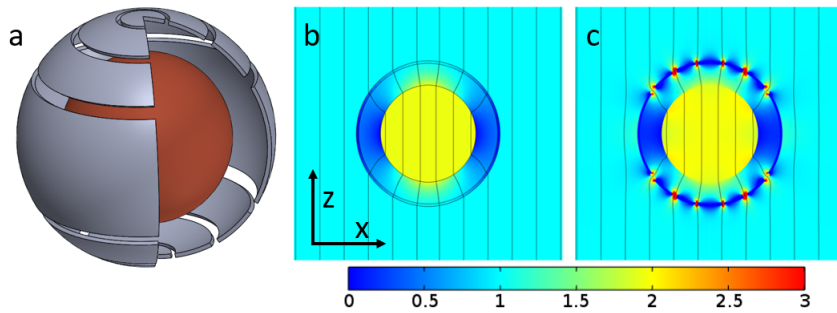


Figure 3.19: (a) Sketch of a ferromagnetic sphere (in red) surrounded by a metamaterial shell made of perfect diamagnetic loops (in gray). (b) Numerical calculations of the magnetic induction field lines and, in colors, $B_z/(\mu_0 H_0)$ for a uniform magnetic field H_0 applied along the z -direction to a ferromagnetic ($\mu = 10^5$) sphere of radius R surrounded by a cloaking shell with internal radius $R_1 = 1.45R$, external radius $R_2 = 1.5R$, and permeability $\mu_1 = 0.059$. (c) Same as in (b) with the shell discretized by the set of perfect diamagnetic ($\mu = 10^{-5}$) loops sketched in (a).

3.4 Chapter summary and conclusions

Transformation optics has been applied to derive the properties of arbitrarily shaped two-dimensional shells that achieve a strong magnetic field concentration inside their holes. Results have been extended to the case of three-dimensional concentrators with spherical geometry by solving Maxwell magnetostatic equations. Numerical calculations have shown that independently of the geometry, the extremely-anisotropic permeability of magnetic concentrators can be realized in practice by metamaterial shells consisting of adequate arrangements of ferromagnetic and perfect diamagnetic materials. For the case of the spherical concentrator, results have been validated experimentally. The possibility of tailoring the shape of the concentrator may benefit applications requiring an efficient use of space. For example, if the goal is to concentrate the field in the region occupied by elongated sensors in order to enhance their sensitivity, it may be convenient to use concentrators with elongated cross-section to achieve a more dense packaging of sensors.

We have demonstrated that concentrators not only concentrate external fields, but also expel towards their exterior the magnetic field generated inside their holes. For the case of two-dimensional concentrators, this property can be used to effectively magnify magnetic objects, so that their magnetic response is equivalent to that of an enlarged material. Both long and short cylindrical concentrators radially enlarge long and short magnetic materials placed inside their holes. Interestingly, when a concentrator surrounds a ferromagnetic (perfect diamagnetic) material, only ferromagnetic (perfect diamagnetic) pieces are required for obtaining the properties of an ideal concentrator with extremely-anisotropic permeability.

In the last part of this chapter, we have derived the properties of a different type of metamaterial shell able to make a magnetic sensor undetectable. This shell cancels the magnetic field distortion created by a magnetic sensor without losing the sensor ability to detect magnetic fields. Sensors are modelled as ferromagnetic materials, since the distortion they create is mainly due to their ferromagnetic parts. The distortion created by spherical sensors in the presence of uniform applied magnetic field can be made exactly zero by a single-layer isotropic and homogeneous spherical shell. When the applied field is non-uniform, the same shell cancels the leading dipolar term of the distortion created by the sensor, but additional layers must be considered if one aims at reducing the distortion further. The distortion created by non-spherical sensors can also be largely reduced by a single or a multilayer spherical shell. Finally, a metamaterial shell consisting of perfect diamagnetic loops has been proposed as a strategy for experimentally realizing the intermediate diamagnetic permeability required for cloaking.

Shaping magnetic fields with negative permeability

Electromagnetic materials exhibiting a negative value of the refractive index, n , show counterintuitive properties that have ignited the development of a wide range of devices for controlling electromagnetic waves [9, 15, 125]. There are not natural materials with a negative index of refraction, but metamaterials have enabled the experimental realization of $n < 0$ from microwaves to optical frequencies [126, 127]. These metamaterials are designed to exhibit both negative permittivity and permeability simultaneously, which results in $n < 0$ [15]. The first experimental demonstration of a metamaterial exhibiting this behaviour was realized in 2000 by Smith et al. and was based on the combination of squared shaped split ring resonators (SRR) and line conducting wires [14]. The SRRs arrangement was shown to provide $\mu < 0$ above its resonant frequency [12, 128], while the lattice of wires possessed a cutoff frequency below which $\varepsilon < 0$ [129]. By choosing the parameters of the wire lattice such that the cutoff frequency was significantly above the SRRs resonant frequency, the composite presented an overlapping region of frequency where both ε and μ were negative, which enabled the realization of the first metamaterials with a negative index of refraction [130, 131].

The experimental realization of a material exhibiting $n < 0$ had a huge impact not only in optics and electromagnetism but also in other communities. Inspired by the unusual properties of materials with negative refractive index, metamaterials with negative constitutive parameters were developed in several areas of physics [32]. For example, there are proposals of materials with negative conductivity for controlling dc electric fields [132], materials with negative bulk modulus and negative mass density for acoustic waves [133, 134, 135], materials with negative compressibility for mechanical waves [136, 137], negative capacitance for electronics [138, 139] and negative thermal expansion coefficients for thermodynamics [140].

For static magnetic fields, metamaterials with a negative value of the magnetic permeability can also be devised [141]. In this chapter, negative-permeability materials are introduced as a novel tool for shaping static magnetic fields. First, we study the properties of materials with $\mu < 0$ and present a method to emulate them. Second, we theoretically and experimentally demonstrate that $\mu < 0$ enables the illusion of transforming the magnetic signature of a magnetic material into that of another one. Finally, we present the analogy of a perfect lens for the case of static magnetic fields, which opens the path towards the creation of magnetic sources at a distance.

4.1 Static negative permeability

Magnetic materials in the presence of static magnetic fields exhibit a permeability value ranging from zero (perfect diamagnetic materials) to effectively infinite (ferromagnetic materials). Even though negative values of the static permeability are not found in naturally occurring materials [142], magnetic metamaterials exhibiting this exotic property can be artificially designed [143]. In this section, we analyse the behaviour of hypothetical materials with negative permeability by extending the solutions of the two magnetostatic Maxwell equations for solid and hollow ellipsoids with positive permeability. Based on the properties of these objects, a method for emulating negative-permeability materials is theoretically proposed and experimentally demonstrated.

4.1.1 Ellipsoids with negative permeability

To study the properties of a material with negative permeability, we choose the general shape of an ellipsoid with the semi-axes a , b and c in x , y and z , respectively, in a uniform field \mathbf{H}_0 applied along the c -axis, as sketched in Fig. 4.1. The ellipsoid relative permeability μ is assumed to be linear, homogeneous, and isotropic. In this situation, the material magnetization and demagnetizing field are uniform and they are related through the demagnetizing factor N as $\mathbf{H}_d = -N\mathbf{M}$, where N is a scalar ranging from 0 (long samples, $c \rightarrow \infty$) to 1 (short samples, $c \rightarrow 0$) [5].

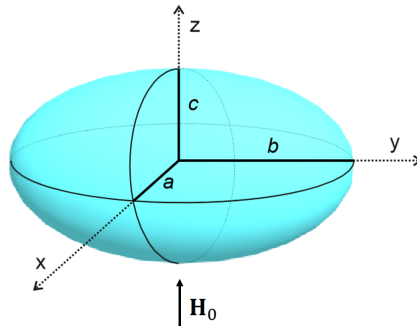


Figure 4.1: Sketch of an ellipsoid with semi-axes a , b and c in a uniform field \mathbf{H}_0 applied along its c -axis.

The behaviour of the ellipsoids can be analysed in terms of the magnetization \mathbf{M} , the magnetic field \mathbf{H} , and the magnetic induction \mathbf{B} in their volume, which are analytically obtained as [1, 2, 4, 144]

$$\mathbf{M} = \frac{\mu - 1}{1 + N(\mu - 1)} \mathbf{H}_0, \quad \mathbf{H} = \frac{1}{1 + N(\mu - 1)} \mathbf{H}_0, \quad \mathbf{B} = \frac{\mu\mu_0}{1 + N(\mu - 1)} \mathbf{H}_0. \quad (4.1)$$

This set of equations shows that all the fields \mathbf{M} , \mathbf{H} and \mathbf{B} are uniform and only depend on the demagnetizing factor and on the material permeability. In Fig. 4.2, \mathbf{M} , \mathbf{H} and \mathbf{B} are plotted as a function of μ for two particularly interesting ellipsoidal geometries: a sphere ($a = b = c$, $N = 1/3$), and a long cylinder in perpendicular field ($a = c$, $b \rightarrow \infty$, $N = 1/2$).

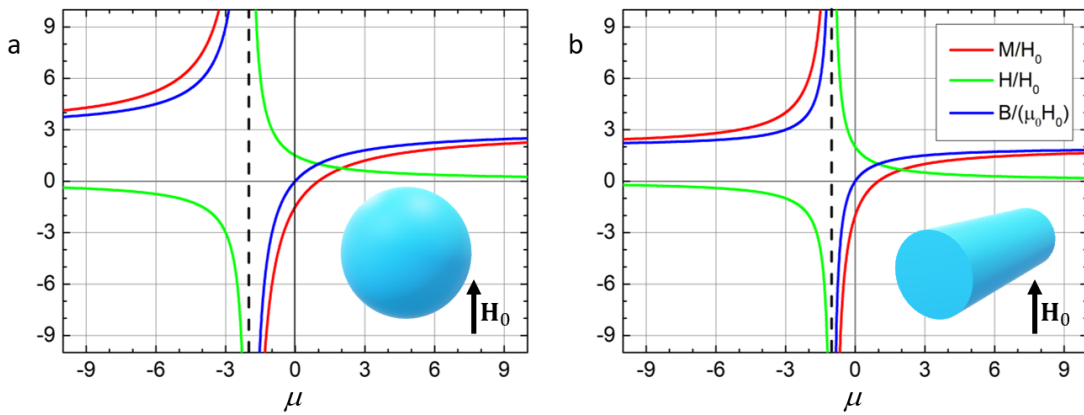


Figure 4.2: Normalized magnetization (in red), magnetic field (in green), and magnetic induction (in blue) as a function of the relative permeability μ when a uniform magnetic field \mathbf{H}_0 is applied to (a) a sphere and (b) a long cylinder.

Materials with negative permeability can be analysed as a natural extension of materials with positive permeability. We start by reviewing how materials with $\mu > 0$ interact with uniform applied magnetic fields. Ferromagnetic materials ($\mu \rightarrow \infty$) exhibit the largest magnetization due to the strong field attraction they provide. The magnetization and the magnetic induction in their volume depend on their geometry as $1/N$: $\mathbf{M}(\mu \rightarrow \infty) = (1/N)\mathbf{H}_0$ and $\mathbf{B}(\mu \rightarrow \infty) = (\mu_0/N)\mathbf{H}_0$. Since $\mathbf{M} = (\mu - 1)\mathbf{H}$ and $\mathbf{B} = \mu\mu_0\mathbf{H}$, $\mathbf{M}(\mu \rightarrow \infty)$ and $\mathbf{B}(\mu \rightarrow \infty)$ can only be finite if the magnetic field in the ferromagnetic volume is zero, $\mathbf{H}(\mu \rightarrow \infty) \rightarrow 0$. As μ is reduced from ∞ to 1, the field attraction decreases and both the modulus of \mathbf{M} and \mathbf{B} are reduced. The modulus of the demagnetizing field ($\mathbf{H}_d = -N\mathbf{M}$) is reduced due to the decrease in \mathbf{M} and, therefore, the modulus of the magnetic field ($\mathbf{H} = \mathbf{H}_0 + \mathbf{H}_d$) is increased. When reaching the air permeability, $\mu = 1$, materials do not attract (nor expel) magnetic fields; $\mathbf{M}(\mu = 1) = 0$, $\mathbf{H}(\mu = 1) = \mathbf{H}_0$, and $\mathbf{B}(\mu = 1) = \mu_0\mathbf{H}_0$. For positive μ -values lower than 1, materials become diamagnetic and repel the applied magnetic field; $\mathbf{M}(0 < \mu < 1)$ has opposite direction to \mathbf{H}_0 and, thus, the modulus of $\mathbf{B}(0 < \mu < 1)$ is lower than $\mu_0 H_0$. In the limit of perfect diamagnetic ellipsoids ($\mu \rightarrow 0$), $\mathbf{B}(\mu \rightarrow 0) \rightarrow 0$.

A further decrease of μ leads us to the region of negative permeability [141]. The main feature one appreciates in Fig. 4.2 for $\mu < 0$ is that there is a negative permeability value that gives a divergence of the magnetic fields. According to the set of equations (4.1), this permeability is $\mu_{\text{DIV}} = (N - 1)/N$; $\mu_{\text{DIV}} = -2$ for the sphere and $\mu_{\text{DIV}} = -1$ for the cylinder. As μ is reduced from 0 to negative values, the fields \mathbf{M} , \mathbf{H} and \mathbf{B} continuously build up (\mathbf{M} and \mathbf{B} in the opposite and \mathbf{H} in the same direction as \mathbf{H}_0) until they become infinite at μ_{DIV} . Because materials with $\mu_{\text{DIV}} < \mu < 0$ are magnetized in the opposite direction to \mathbf{H}_0 , they can be classified as diamagnetic materials. Since the modulus of their magnetization is larger than that of perfect diamagnetic materials, these materials expel magnetic field lines even more strongly than perfect diamagnets (see Figs. 4.3a and c). For μ -values lower than μ_{DIV} the ellipsoids change their behaviour completely and the direction of all the fields is inverted. The modulus of \mathbf{M} , \mathbf{H} and \mathbf{B} decreases with μ and in the limit $\mu \rightarrow -\infty$ their magnitude is the same as in the limit $\mu \rightarrow \infty$. Because materials with $\mu < \mu_{\text{DIV}}$ are magnetized in the direction of the applied field, they can be regarded as paramagnetic materials. The field attraction they provide is even larger than that of ferromagnetic materials (see Figs. 4.3b and d).

To understand how negative-permeability materials behave and why they can produce such strong magnetic responses, it is important to analyse the energy density, $E = (1/2)\mathbf{H} \cdot \mathbf{B}$, in their volume. In linear, homogeneous and isotropic materials, the energy density can be written as $E = (1/2)\mu\mu_0 H^2$, where H is the modulus of the magnetic field. This expression shows that the energy density is positive in the volume occupied by a positive-permeability material and negative in the volume of a material with negative permeability.

Consider an ellipsoid of volume V in a uniform field H_0 . The total magnetic energy the applied field creates in the region occupied by the ellipsoid is $\mathcal{E}_0 = (1/2)\mu_0 V H_0^2$. As shown in Figs. 4.3a and b, the positive-permeability ellipsoids exhibiting the largest field attraction ($\mu \rightarrow \infty$) and repulsion ($\mu \rightarrow 0$) expel all the magnetic energy \mathcal{E}_0 from their volume (materials with $\mu \rightarrow \infty$ because $\mathbf{H} = 0$ and materials with $\mu \rightarrow 0$ because $\mathbf{B} = 0$). This energy is redistributed to the rest of space and is responsible for the distortion of the applied magnetic field. Materials with intermediate positive permeability values also expel some magnetic energy, but their magnetic responses are weaker because they keep part of the energy in their volume. Materials with negative permeability, as shown in Fig. 4.2, show larger magnetic responses than materials with $\mu \rightarrow \infty$ and $\mu \rightarrow 0$. In Fig. 4.3c, a cylinder with $\mu = -1/2$ is shown to expel the applied magnetic induction field lines much further than a cylinder with $\mu \rightarrow 0$ (Fig. 4.3b) and in Fig. 4.3d a cylinder with $\mu = -2$ is shown to attract more lines than a cylinder with $\mu \rightarrow \infty$ (Fig. 4.3a). In terms of energy reorganization, these materials can only achieve these strong magnetic responses if they expel more magnetic energy from their volume than materials with $\mu \rightarrow \infty$ and $\mu \rightarrow 0$; that is, they expel more energy than the energy \mathcal{E}_0 that the applied magnetic field provides.

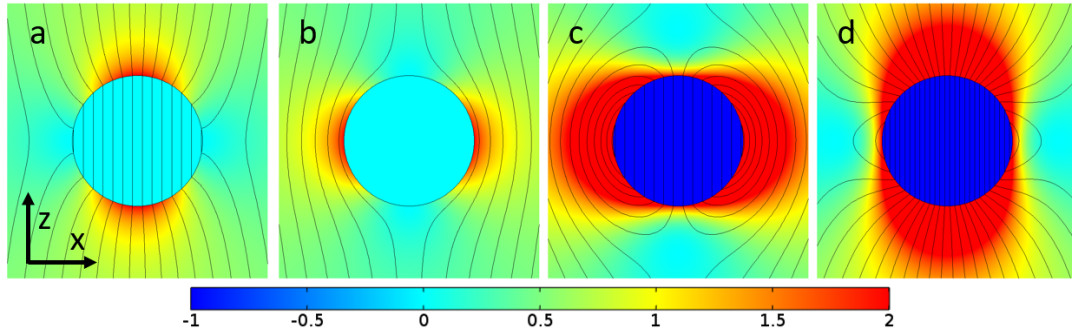


Figure 4.3: Numerical calculations of the magnetic induction field lines and (in colors) the normalized energy density $E/(\mu_0 H_0^2)$ when a uniform magnetic field H_0 is applied along the z -direction to a long cylinder with isotropic relative permeability (a) $\mu = 10^4$, (b) $\mu = 10^{-4}$, (c) $\mu = -1/2$, and (d) $\mu = -2$.

In other words, positive-permeability materials can be regarded as materials that redistribute the magnetic energy \mathcal{E}_0 that the applied magnetic field provides in their volume. The manner in which they redistribute this energy depends on their geometry and permeability. In contrast, negative-permeability materials, do not redistribute the energy \mathcal{E}_0 but a larger amount of energy. Since this energy is not provided by the uniform applied magnetic field, materials with $\mu < 0$ can be understood as active because they themselves are responsible for generating the extra amount of magnetic energy they need to expel [145]. In this sense, the negative energy in the $\mu < 0$ materials volume can be regarded as energy that the material has to generate in order to behave as a material with negative permeability. Active materials and metamaterials have already been introduced for controlling a wide range of fields, including thermal [146], acoustic [147], electric [148, 149], and electromagnetic waves [150, 151, 152, 153]. A strategy on how to create an active negative- μ material for magnetostatic fields based on electric currents will be presented in Sec. 4.1.3

4.1.2 Hollow ellipsoids with negative permeability

Once the behaviour of solid ellipsoids has been described, we can move to the study of hollow bodies. This analysis is relevant because hollow materials with negative permeability may achieve a strong magnetic field concentration inside their hole and lead to novel strategies for concentrating static magnetic fields, for example [75].

Consider a hollow ellipsoid in the presence of a uniform applied magnetic field. Different from the case of a solid ellipsoid [see the set of equations (4.1)], the magnetic fields \mathbf{M} , \mathbf{H} , and \mathbf{B} in the volume of a hollow ellipsoid are not uniform [144]. Consequently, hollow ellipsoids respond to uniform magnetic fields creating, in general, a multipolar magnetic field distribution. Only in the case of hollow spheres and hollow cylinders, the response of the material is merely dipolar and the field distribution everywhere in

space can be easily derived from the magnetostatic Maxwell equations. For this reason, in this section we restrict our study to hollow spheres and cylinders in uniform applied magnetic fields. It was shown in Chapter 3 that metamaterial shells with positive anisotropic magnetic permeability exhibit interesting possibilities for shaping static magnetic fields, such as strong magnetic field concentration or cloaking [69]. Here we extend this analysis to consider negative values of the permeability. In this way, we will be able to explore novel solutions for concentrating and cloaking static magnetic fields.

Consider a sphere with radius R_2 with a centered empty hole of radius R_1 characterized by a homogeneous and anisotropic relative permeability tensor fulfilling (in spherical coordinates r, θ, φ) $\mu_{r\theta} = \mu_{\theta r} = \mu_{r\varphi} = \mu_{\varphi r} = \mu_{\theta\varphi} = \mu_{\varphi\theta} = 0$, $\mu_{\theta} = \mu_{\theta\theta} = \mu_{\varphi\varphi}$, and $\mu_r = \mu_{rr}$. A uniform magnetic field \mathbf{H}_0 is applied in the z -direction. Since there are not free currents involved and the material is homogeneous, the magnetic field can be written in terms of a magnetic scalar potential ϕ that fulfills the Laplace equation everywhere in space [Eq. (2.1)]. The general solution for ϕ inside the hole (INT), in the shell (SHE), and in the external region (EXT) can be written as

$$\phi_s^{\text{INT}} = a_s r \cos\theta, \quad (4.2)$$

$$\phi_s^{\text{SHE}} = \left(\frac{c_s}{r^{(1-\alpha)/2}} + \frac{d_s}{r^{(1+\alpha)/2}} \right) \cos\theta, \quad (4.3)$$

$$\phi_s^{\text{EXT}} = \left(\frac{b_s}{r^2} - H_0 r \right) \cos\theta, \quad (4.4)$$

where $\alpha^2 = 8\mu_{\theta}/\mu_r + 1$ and we have taken into account that the potential must be finite at $r = 0$ and tend to the applied potential, $-H_0 r \cos\theta$, when $r \rightarrow \infty$. The coefficients a_s , b_s , c_s and d_s are obtained by applying the magnetostatic boundary conditions [Eqs. (1.14) and (1.15)]. That is, the angular component of \mathbf{H} and the radial component of \mathbf{B} must be continuous at the material surfaces $r = R_1$ and $r = R_2$. In this way, the coefficients are found to be

$$a_s = \frac{6\mu_r\alpha (R_2/R_1)^{(3+\alpha)/2} H_0}{4\mu_r\mu_{\theta} + \mu_r(1-3\alpha) + 4 - [4\mu_r\mu_{\theta} + \mu_r(1+3\alpha) + 4] (R_2/R_1)^{\alpha}}, \quad (4.5)$$

$$b_s = \frac{-2(2\mu_r\mu_{\theta} - \mu_r - 1) [(R_2/R_1)^{\alpha} - 1] R_2^3 H_0}{4\mu_r\mu_{\theta} + \mu_r(1-3\alpha) + 4 - [4\mu_r\mu_{\theta} + \mu_r(1+3\alpha) + 4] (R_2/R_1)^{\alpha}}, \quad (4.6)$$

$$c_s = \frac{3(\mu_r\alpha + \mu_r + 2) R_2^{(3+\alpha)/2} R_1^{-\alpha} H_0}{4\mu_r\mu_{\theta} + \mu_r(1-3\alpha) + 4 - [4\mu_r\mu_{\theta} + \mu_r(1+3\alpha) + 4] (R_2/R_1)^{\alpha}}, \quad (4.7)$$

$$d_s = \frac{3(\mu_r\alpha - \mu_r - 2) R_2^{(3+\alpha)/2} H_0}{4\mu_r\mu_{\theta} + \mu_r(1-3\alpha) + 4 - [4\mu_r\mu_{\theta} + \mu_r(1+3\alpha) + 4] (R_2/R_1)^{\alpha}}. \quad (4.8)$$

Analogous results are found for a long (along y) cylinder of radius R_2 with a centered long (along y) hole of radius R_1 in a uniform magnetic field \mathbf{H}_0 applied along the cylinder c -axes. The components of the cylinder permeability tensor (in cylindrical coordinates ρ, φ, z) are assumed to be $\mu_{\rho\varphi} = \mu_{\varphi\rho} = \mu_{\rho z} = \mu_{z\rho} = \mu_{\varphi z} = \mu_{z\varphi} = 0$, $\mu_\rho = \mu_{\rho\rho}$, $\varphi = \mu_{\varphi\varphi}$ and $\mu_z = 1$. The general solution for the magnetic scalar potential inside the hole (INT), in the shell (SHE) and in the external region (EXT), is

$$\phi_c^{\text{INT}} = a_c \rho \cos \varphi, \quad (4.9)$$

$$\phi_c^{\text{SHE}} = \left(c_c \rho^k + \frac{d_c}{\rho^k} \right) \cos \varphi, \quad (4.10)$$

$$\phi_c^{\text{EXT}} = \left(\frac{b_c}{\rho} - H_0 \rho \right) \cos \varphi, \quad (4.11)$$

where $k^2 = \mu_\varphi / \mu_\rho$ and the coefficients a_c, b_c, c_c and d_c , obtained from the magnetostatic boundary conditions as before, are

$$a_c = \frac{4\mu_\rho k (R_2/R_1)^{1+k} H_0}{(\mu_\rho k - 1)^2 - (\mu_\rho k + 1)^2 (R_2/R_1)^{2k}}, \quad (4.12)$$

$$b_c = \frac{-(\mu_\rho \mu_\varphi - 1) R_2^2 \left[(R_2/R_1)^{2k} - 1 \right] H_0}{(\mu_\rho k - 1)^2 - (\mu_\rho k + 1)^2 (R_2/R_1)^{2k}}, \quad (4.13)$$

$$c_c = \frac{2(\mu_\rho k + 1) R_2^{1-k} (R_2/R_1)^{2k} H_0}{(\mu_\rho k - 1)^2 - (\mu_\rho k + 1)^2 (R_2/R_1)^{2k}}, \quad (4.14)$$

$$d_c = \frac{2(\mu_\rho k - 1) R_2^{1+k} H_0}{(\mu_\rho k - 1)^2 - (\mu_\rho k + 1)^2 (R_2/R_1)^{2k}}. \quad (4.15)$$

Two important properties for the spherical and the cylindrical shells result from these solutions. First, the magnetic field inside the hole of these shells is always uniform and aligned in the same or in the opposite direction to \mathbf{H}_0 , with magnitude $H_z = -a_{s,c}$ [Eqs. (4.2) and (4.9)]. Therefore, shells showing high values of the coefficient $a_{s,c}$ can be used as magnetic concentrators and shells with low values of $a_{s,c}$ as attenuators or shielding shells. Second, the magnetic field in the external region is, in general, modified with respect to the applied field due to the presence of the shells [Eqs. (4.4) and (4.11)]. The magnetic field created by the shells in their exterior corresponds to the field created by a point dipole with magnetic moment $m_s = 4\pi b_s$ for the spherical shell and to the field of a long dipole with magnetic moment per unit length $m_c = 2\pi b_c$ for the cylindrical shell. Shells with a positive value of the coefficient $b_{s,c}$ attract magnetic induction field lines and can be classified as paramagnetic shells. On the contrary, shells with $b_{s,c} < 0$ expel the magnetic induction field lines and can be regarded as diamagnetic shells. Only the shells exhibiting $b_{s,c} = 0$ do not distort the uniform applied magnetic field.

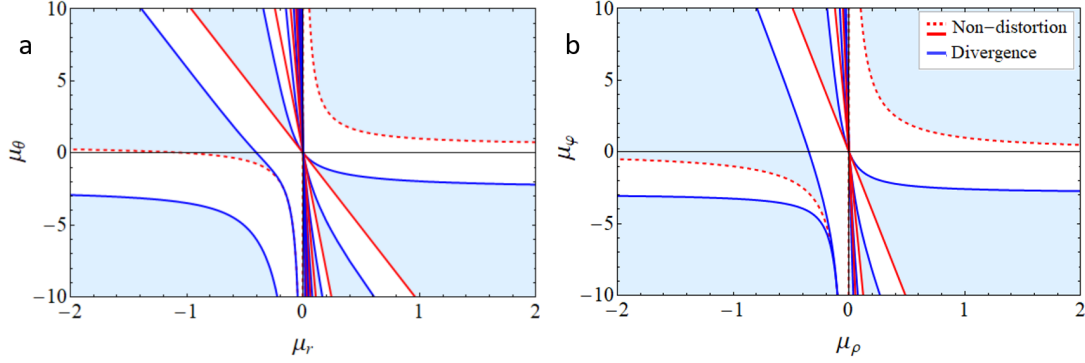


Figure 4.4: Relations between the angular and the radial relative magnetic permeability resulting in non-distortion (red lines) and in field divergences (blue lines) for a spherical shell (a) and a cylindrical shell (b). The solid and dashed red lines indicate if the non-distortion shell is of the first or of the second type, respectively. The chosen shell radii ratio is $R_2/R_1 = 2$ in both cases. The light-blue regions correspond to paramagnetic shells, while the white regions correspond to diamagnetic shells.

Different from the case of isotropic solid spheres and cylinders, for which the fields diverged at a particular negative value of the permeability (Fig. 4.2), when considering anisotropic hollow spheres and cylinders there are infinite permeability values for which the magnetic field diverges. According to Eqs. (4.5)-(4.8) and Eqs. (4.12)-(4.15), the divergences occur when

$$\sqrt{-\alpha^2} \log(R_2/R_1) = 2 \arctan \left(\frac{3\mu_r \sqrt{-\alpha^2}}{4\mu_r \mu_\theta + \mu_r + 4} \right) + 2\pi n, \quad n = 0, 1, 2, \dots, \quad (4.16)$$

$$\sqrt{-k^2} \log(R_2/R_1) = \arctan \left(\frac{-2\mu_\rho \sqrt{-k^2}}{\mu_\rho \mu_\varphi + 1} \right) + \pi n, \quad n = 0, 1, 2, \dots, \quad (4.17)$$

for spherical and cylindrical shells, respectively. The permeability relations resulting from these expressions are plotted as blue lines in Fig. 4.4. Interestingly, there are also infinite anisotropic shells that do not distort the applied magnetic field, which fulfill

$$\mu_\theta = -\frac{\mu_r}{8} \left[\left(\frac{2\pi n}{\log(R_2/R_1)} \right)^2 + 1 \right], \quad n = 1, 2, 3, \dots, \quad (4.18)$$

$$\mu_\theta = \frac{1 + \mu_r}{2\mu_r}, \quad (4.19)$$

and

$$\mu_\varphi = -\mu_\rho \left(\frac{\pi n}{\log(R_2/R_1)} \right)^2, \quad n = 1, 2, 3, \dots, \quad (4.20)$$

$$\mu_\varphi = \frac{1}{\mu_\rho}, \quad (4.21)$$

for spherical and cylindrical shells, respectively.

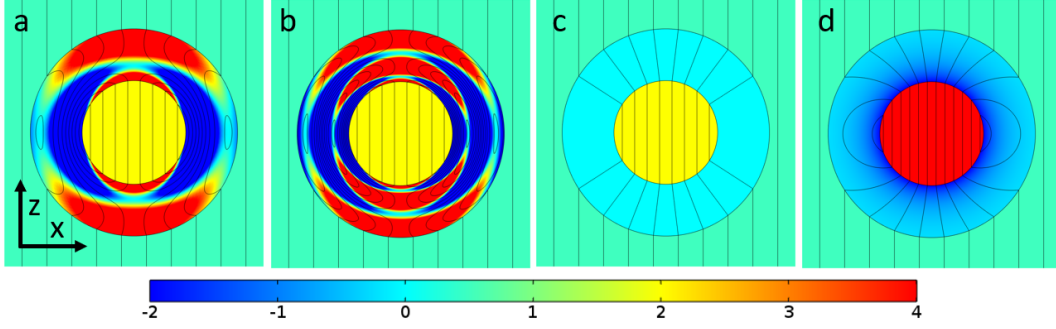


Figure 4.5: Numerical calculations of the magnetic induction field lines and (in colors) the energy density $E/(\mu_0 H_0^2)$ for a uniform field H_0 applied along the z -direction to four long cylindrical shells with internal radius R_1 and external radius $R_2 = 2R_1$. The shells in (a) and (b) are non-distorting shells of the first type, with $\mu_\rho = 0.1$, $\mu_\varphi = -2.05$ (a), and $\mu_\rho = 0.1$, $\mu_\varphi = -8.22$ (b). The shells in (c) and (d) are non-distorting shells of the second type, with $\mu_\rho = 10^4$, $\mu_\varphi = 10^{-4}$ (c), and $\mu_\rho = -2$, $\mu_\varphi = -1/2$ (d).

These non-distorting shells can be classified in two different types according to their ability to concentrate magnetic fields inside their holes.

The first type of non-distorting shells have a radial and angular permeability fulfilling Eq. (4.18) for spherical shells and Eq. (4.20) for cylindrical shells. These permeability relations are plotted in straight red lines in Fig. 4.4 and always involve a positive and a negative component of the permeability. There is an infinite number of these lines, and their slope depends upon a single parameter, n . The magnetic field inside the hole of non-distorting shells of this type does not depend on the shell permeability; it is always fixed to $H_s^{\text{INT}} = \pm H_0 (R_2/R_1)^{3/2}$ for spherical shells and to $H_c^{\text{INT}} = \pm H_0 R_2/R_1$ for cylindrical shells, with positive sign when n is even and negative sign when n is odd. Two examples of this type of cylindrical shells are shown in Figs. 4.5a and b.

The second type of non-distorting shells have a radial and angular permeability fulfilling Eq. (4.19) for spherical shells and Eq. (4.21) for cylindrical shells. These permeability relations are plotted in dashed red lines in Fig. 4.4. The field inside the hole of these shells depends on the radii ratio of the shell and on the permeability as

$$H_s^{\text{INT}} = H_0 (R_2/R_1)^{2-2\mu_\theta}, \quad (4.22)$$

$$H_c^{\text{INT}} = H_0 (R_2/R_1)^{1-\mu_\varphi}, \quad (4.23)$$

for spherical and cylindrical shells, respectively. This indicates that, for a fixed radii ratio R_2/R_1 , the magnetic field concentrating ratio can be made arbitrarily large by decreasing the angular permeability (μ_θ or μ_φ) from ∞ to $-\infty$. Restricting to positive values of both the radial and the angular permeability, the maximum field concentration ratio these shells can achieve is $H^{\text{INT}}/H_0 = R_2/R_1$, both for spherical ($\mu_\theta \rightarrow 1/2, \mu_r \rightarrow \infty$) and cylindrical shells ($\mu_\varphi \rightarrow 0, \mu_\rho \rightarrow \infty$). Actually, these extremely anisotropic shells were presented in Sec. 3.1 as magnetic concentrators.

For negative permeability values, the concentration ratio achieved by non-distorting shells of the second type is always larger than the maximum concentration ratio achieved with positive permeabilities. From energy conservation analysis, one finds that this can only occur if, similar to the case of solid ellipsoids with $\mu < 0$, shells with negative permeability do not only redistribute the energy provided by the applied field but also some extra energy that they actively provide. Consider a cylindrical shell with permeabilities $\mu_\varphi \rightarrow 0$ and $\mu_\rho \rightarrow \infty$ (Fig. 4.5c), which is the non-distorting shell with positive permeability that achieves the largest magnetic field concentration. All the magnetic energy in the volume occupied by the shell (including its hole), $\mathcal{E}_0 = 1/2\mu_0 H_0^2 \pi R_2^2 b_2$ is uniformly redistributed inside the hole. In this way, the energy density in the hole becomes $E^{\text{INT}} = (1/2)\mu_0 H_0^2 (R_2/R_1)^2$ and the energy density in the shell is zero $E^{\text{SHE}} = 0$. As illustrated in the example in Fig. 4.5d, non-distorting shells with negative permeabilities μ_φ and μ_ρ fulfilling Eq. (4.21) achieve larger magnetic field concentrations than shells with $\mu_\varphi \rightarrow 0$ and $\mu_\rho \rightarrow \infty$ because the energy in their volume is negative. Thus, concentration ratios larger than R_2/R_1 can only be achieved by active materials that generate the extra amount of energy that has to be redistributed.

4.1.3 Negative-permeability emulation with active metamaterials

Materials with negative permeability do not occur in nature [142]. Because magnetic metamaterials have enabled the design of novel permeability tensors [74, 79], a possible strategy for achieving $\mu < 0$ could be the construction of a new kind of magnetic metamaterial. In the previous sections we have seen that negative-permeability materials must be understood as active materials because of their ability to generate magnetic energy. Thus, in order to achieve $\mu < 0$, the metamaterials should be able to feed energy into the system. Different from the metamaterials studied in Chapter 3, these active metamaterials cannot be constituted by combinations of passive materials with positive permeability.

In order to understand how active metamaterials exhibiting $\mu < 0$ could be designed, it is interesting to analyse how negative-permeability materials distribute the magnetic induction field lines. Figures 4.3 and 4.5 show that closed magnetic field lines appear when materials with negative- μ are assumed. Because of Ampere's law, closed magnetic field lines can only occur in linear materials if there are free currents in the system. This suggests that negative-permeability materials can be emulated by feeding energy in the form of electric currents. At this point, it is worth recalling that a magnetic material can be substituted by its magnetization currents, which give exactly the same magnetic induction field distribution as the material itself. These magnetization currents, located at the surface and in the volume occupied by the material, can be calculated from the material magnetization using Eqs. (1.11) and (1.12). This property, well-known for materials with positive- μ can be extended to the case of negative- μ .

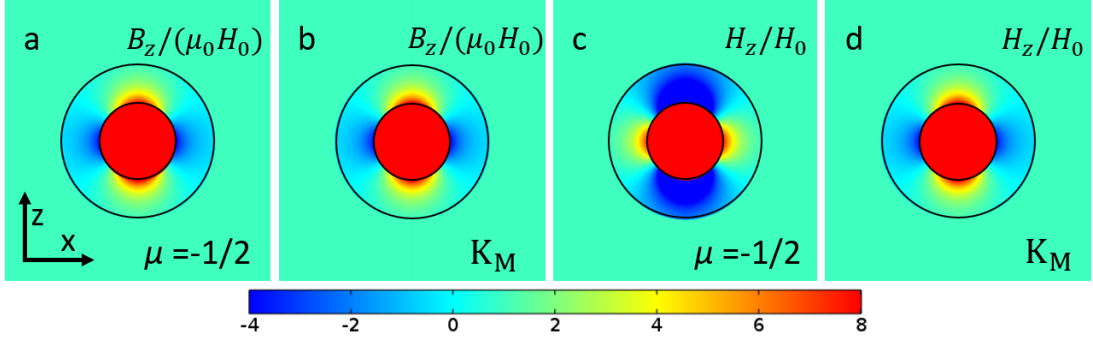


Figure 4.6: Comparison between a negative- μ material and its emulation by currents when a uniform magnetic field H_0 is applied along the z -direction. In (a) and (b) colors correspond to the z -component of the magnetic induction normalized to $\mu_0 H_0$. In (c) and (d) colors show the z -component of the magnetic field normalized to H_0 . In (a) and (c) the field interacts with a spherical shell with internal radius R_1 , external radius $R_2 = 2R_1$ and relative permeability $\mu = -1/2$. In (b) and (d) the spherical shell is substituted by its magnetization currents according to Eqs. (4.24) and (4.25).

In this way, even though negative- μ materials do not exist in magnetostatics, their behaviour can be emulated in practice by a suitably tailored arrangement of currents, which constitute the active metamaterial. These currents can be analytically calculated from the magnetization that the desired material would show in the presence of an applied magnetic field. Since the magnetization of a material depends on the applied magnetic field, the currents have to be readjusted when changing the applied field.

As an example, let us now consider the case of a spherical shell with internal radius R_1 , external radius R_2 , and isotropic permeability $\mu = -1/2$ in a uniform magnetic field $\mathbf{H}_0 = H_0 \mathbf{u}_z$. According to Eq. (4.19), this shell does not distort uniform applied fields and, according to Eq. (4.22), the field inside its hole is $H_s^{\text{INT}} = H_0 (R_2/R_1)^3$ aligned in the same direction as the applied field. This large magnetic field concentration is achieved at the cost of having a negative energy density in the spherical shell volume, which can be externally supplied in the form of electric currents. The calculation of the current density that has to be fed to the shell requires the knowledge of the shell magnetization \mathbf{M} , which can be obtained from the constitutive relation (1.13) and Eqs. (4.2)-(4.8). Since the chosen material is linear, homogeneous, and isotropic its volume magnetization currents \mathbf{J}_M are zero [Eq. (1.11)]. The spherical shell only shows surface magnetization currents \mathbf{K}_M , which flow in its internal ($r = R_1$) and external ($r = R_2$) surfaces as

$$\mathbf{K}_M(r = R_1) = \frac{3}{2} \left(\frac{R_2}{R_1} \right)^3 H_0 \sin\theta \mathbf{u}_\varphi, \quad (4.24)$$

$$\mathbf{K}_M(r = R_2) = -\frac{3}{2} H_0 \sin\theta \mathbf{u}_\varphi. \quad (4.25)$$

These current distributions give exactly the same magnetic induction \mathbf{B} as a spherical shell with $\mu = -1/2$ in the whole space. This is illustrated in Figs. 4.6a and b. In contrast, the magnetic field \mathbf{H} resulting from these currents is not the same as that of the negative- μ material in all space, as shown in Figs. 4.6c and d. On the one hand, when having a magnetic material with $\mu = -1/2$, the magnetic field inside the shell volume is $\mathbf{H} = \mathbf{B}/(\mu\mu_0) = -2\mathbf{B}/\mu_0$ and the magnetic field inside the hole and in the external region is $\mathbf{H} = \mathbf{B}/\mu_0$. On the other hand, when substituting the material by currents, the magnetic field is $\mathbf{H} = \mathbf{B}/\mu_0$ in the whole space and, therefore, it is different from the field resulting from a material with $\mu = -1/2$ in the material volume. The magnetization in the shell region for the case of the negative- μ material, $\mathbf{M} = (\mu - 1)\mathbf{H} = 3\mathbf{B}/\mu_0$, is also different from the magnetization for the current densities, $\mathbf{M} = 0$.

4.1.4 Experimental realization of a negative-permeability material

A negative-permeability material is experimentally realized to demonstrate the presented theory [141]. We choose a spherical shell with isotropic relative magnetic permeability $\mu = -1/2$, internal radius $R_1 = 25\text{mm}$ and external radius $R_2 = 50\text{mm}$. The field distribution in the presence of this shell can be seen in Fig. 4.7a.

The required surface current densities to emulate this material are given by Eqs. (4.24) and (4.25). For practical reasons, these continuous current distributions are converted into two discrete sets of current loops. The intensity that has to be fed to each loop can be calculated as the integral of the surface current density,

$$I(R_a, \theta_i) = \int_{\theta_i - \pi/(2n)}^{\theta_i + \pi/(2n)} K_M(r = R_a) R_a d\theta, \quad (4.26)$$

where θ_i is the azimuth angle of each current loop, $a = 1, 2$ is an index to differentiate between the internal and the external surface, and n indicates the number of current loops on each surface. Numerical calculations show that a discretization into six current loops (Fig. 4.7b) generates a magnetic induction distribution that approximates well the distribution for the ideal continuous current density case (Fig. 4.7a). The loops are placed at $\theta_1 = 15^\circ$, $\theta_2 = 45^\circ$, $\theta_3 = 75^\circ$, $\theta_4 = 105^\circ$, $\theta_5 = 135^\circ$, $\theta_6 = 165^\circ$. Figures 4.8a and b show the analytic field distribution together with the field distribution calculated with the finite-elements method for the discretized case of 6 internal plus 6 external current loops. Only close to the surfaces there is a small discrepancy between the ideal and the discretized cases, which is due to the coarse discretization.

In order to place each current loop at the required position (R_a, θ_i) a 3D-printed non-magnetic plastic support with grooves at the loops locations is designed, as shown in Figs. 4.7c and d. In the experiments, the current is fed to the loops using a common voltage source from a Agilent 6671A power supply. Each loop is connected in series with the adequate load resistor to achieve the required current according to Eq. (4.26). The set of resistors can be seen in the picture of the experimental setup in Fig. 4.7e. The spherical shell is placed in between a pair of Helmholtz coils, which create a uniform

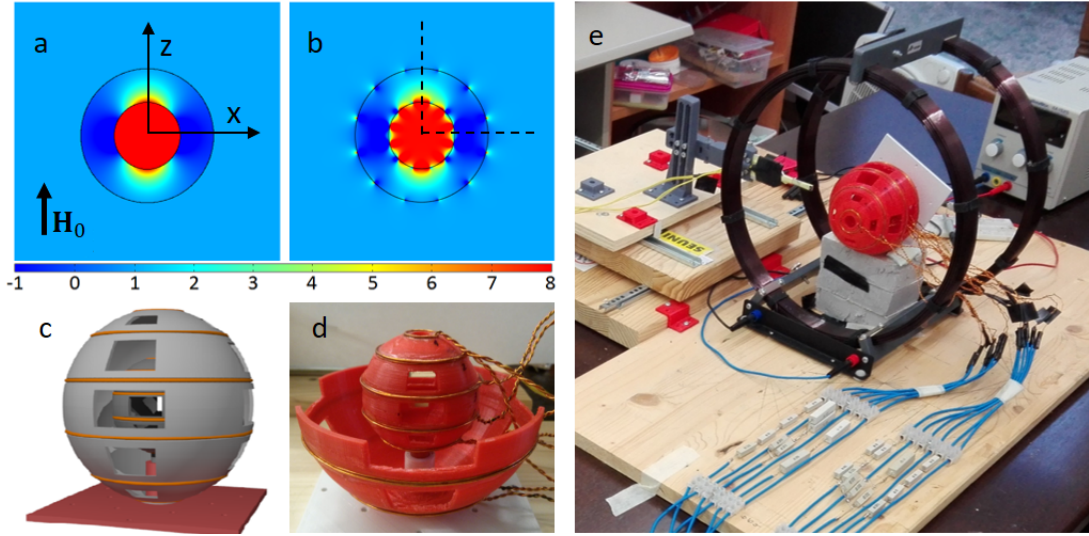


Figure 4.7: Finite-element simulations of the z -component of \mathbf{B} normalized to $B_0 = \mu_0 H_0$ when a magnetic induction \mathbf{B}_0 is applied in the z -direction to a spherical shell with (a) $\mu = -1/2$ and radii ratio $R_2/R_1 = 2$, and (b) the same shell emulated by 6 current loops placed at R_1 and 6 current loops placed at R_2 . Both sets of currents fulfill Eq. (4.26). Dashed lines indicate the measuring lines. Panels (c) and (d) show the three-dimensional sketch and the actual experimental realization, respectively, of the metamaterial spherical shell shown in (b). (e) Picture of the experimental setup with the metamaterial in the middle of a pair of Helmholtz coils.

magnetic field $B_0 = \mu_0 H_0 = 0.0543 \text{ mT}$ (taking into account the contribution of the Earth magnetic field) in the z -direction, along the shell axis. A Hall probe is used to measure the z -component of the magnetic induction along the x -axis (Fig. 4.8a) and along the z -axis (Fig. 4.8b), both indicated with dashed lines in Fig. 4.7b. Results in Figs. 4.8a and b show a very good agreement between the experimental measurements and the numerical calculations for the discretized device. The field inside the hole of the shell is uniform with the expected concentrating ratio of $(R_2/R_1)^3 = 8$ and the external field is not modified by the presence of the shell, in accordance with the theory.

In this way, we have experimentally emulated a spherical shell with $\mu = -1/2$ in a uniform applied magnetic field. If the applied field is changed, our device does not longer act as a spherical shell with $\mu = -1/2$. Because the magnetization currents depend on the applied field magnitude [Eqs. (4.24) and (4.25)], the current of each loop needs to be readjusted in order to keep emulating the same negative- μ material, (4.26). To this end, one could design a feedback loop that automatically adjusts the currents by measuring the magnitude of the applied field [111]. Finally, the discretization used for our device (Figs. 4.7c and d) is only adequate for uniform fields applied perpendicular to the current loops. Uniform fields applied in other directions or fields with other spatial dependences would require more advanced discretization schemes.

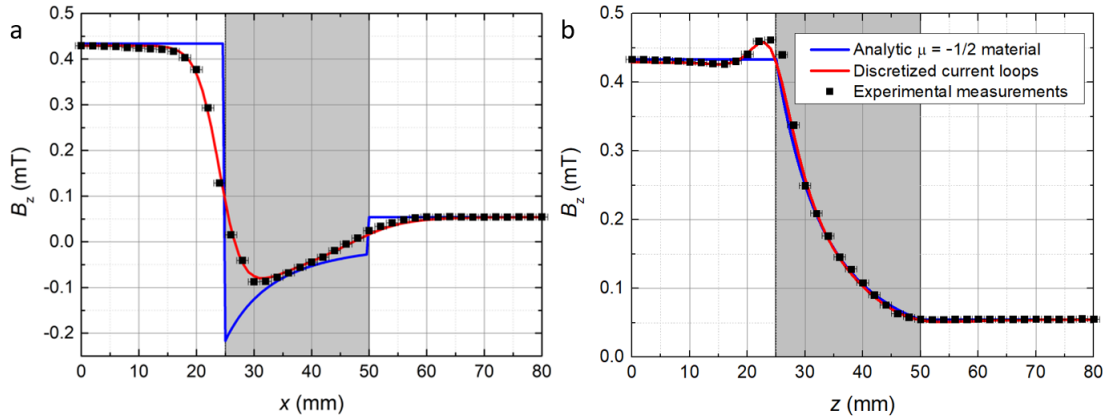


Figure 4.8: Experimental measurements (symbols), finite-element calculation for the discretized set of currents (red line), and analytic results for the ideal material with $\mu = -1/2$ (blue line). The z -component of \mathbf{B} is plotted along (a) the x -axis (with $y = z = 0$), and (b) the z -axis (with $x = y = 0$). The shell region is painted in grey.

4.2 Illusion: disguising an object as another object

The appearance of objects is determined by the way they interact with electromagnetic fields, which depends on their geometry and constitutive parameters. One of the most fascinating applications of transformation optics and metamaterials has been the development of electromagnetic invisibility cloaks [21]. Most of the cloaks that have been proposed can be classified as *transformation cloaks*, which make objects invisible by preventing electromagnetic fields from reaching the objects [7, 10, 20], or as *scattering-cancellation cloaks*, which make object invisible by cancelling their scattering [56, 154]. The goal of cloaks is to create the illusion of empty space, so that electromagnetic fields pass through the cloaked volume as if the object was not there. In 2009, Yun Lai et al. generalized these ideas by introducing the concept of *illusion optics*, which provides a method for making an object of arbitrary shape and electromagnetic properties appear not as empty space (as achieved by invisibility cloaks) but as another object with other shape and properties [26, 155, 156]. Several experiments achieving illusion for electromagnetic waves have been reported, usually involving media with negative values of the permittivity and the permeability [27, 153, 157, 158, 159]. Illusion for other fields, such as illusion thermodynamics have also been proposed [160].

Illusion for static magnetic fields can be regarded as the transformation of the magnetic signature of an object into that of another one. It was introduced as a tool for cancelling, enlarging and overlapping magnets [161], but the development of these ideas was braked because of the lack of negative permeability materials in magnetostatics. The recent proposal of active metamaterials exhibiting an effective $\mu < 0$ [141] has enabled the first experimental realization of magnetic illusion [111]. In this section, we present the theoretical and the experimental demonstration of illusion in magnetostatics.

4.2.1 Derivation of illusion in magnetostatics

Consider an original sphere of radius R_1 and linear, isotropic and homogeneous relative magnetic permeability μ_1 in a uniform magnetic field \mathbf{H}_0 applied along the z -direction, as sketched in Fig. 4.9a. For our goal of achieving illusion, we surround this sphere with a spherical shell with internal radius R_1 , external radius R_2 , and linear, isotropic, and homogeneous relative magnetic permeability μ_2 , which acts as an illusion device (Fig. 4.9b). Illusion is achieved when the magnetic response of the original sphere surrounded by the illusion device is made indistinguishable from the response of a target sphere, with radius R and linear, isotropic, and homogeneous relative magnetic permeability μ (Fig. 4.9c).

On the one hand, the field distribution outside the target sphere is equivalent to the field created by a centered point dipole with magnetic moment pointing towards the z -direction with magnitude [144]

$$m_s = 4\pi \frac{\mu - 1}{\mu + 2} R^3 H_0. \quad (4.27)$$

On the other hand, the magnetic response of the coated sphere can be obtained by solving the magnetostatic Maxwell equations. As in the previous section, since there are not free currents involved, the magnetic field can be found as the gradient of a magnetic scalar potential ϕ that fulfills the Laplace equation. The scalar potential inside the original sphere (MAT: $r \leq R_1$), inside the illusion device (SHE: $R_1 < r < R_2$) and in the external region (EXT: $r \geq R_2$), can be written as

$$\phi_{\text{cs}}^{\text{MAT}} = a_{\text{cs}} r \cos\theta, \quad (4.28)$$

$$\phi_{\text{cs}}^{\text{SHE}} = \left(b_{\text{cs}} r + \frac{c_{\text{cs}}}{r^2} \right) \cos\theta, \quad (4.29)$$

$$\phi_{\text{cs}}^{\text{EXT}} = \left(\frac{d_{\text{cs}}}{r^2} - H_0 r \right) \cos\theta, \quad (4.30)$$

where we have taken into account that the potential must be finite at $r = 0$ and tend to the applied potential, $-H_0 r \cos\theta$, when $r \rightarrow \infty$.

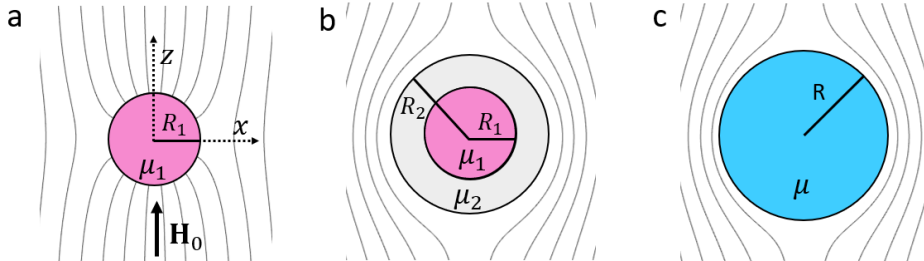


Figure 4.9: Sketch of an example of magnetic illusion. The magnetic signature of an original ferromagnetic sphere (a) covered by a negative-permeability illusion device (b) corresponds to the signature of a larger perfect diamagnetic sphere (c).

The coefficients a_{cs} , b_{cs} , c_{cs} , and d_{cs} can be obtained by applying magnetostatic boundary conditions. Equations (4.30) and (4.31) indicate that, in the external region, the coated sphere creates the same magnetic scalar potential as a point dipole located at the center of the sphere, pointing towards the z -direction with dipolar magnetic moment [144],

$$m_{cs} = 4\pi d_{cs} = 4\pi \frac{(\mu_1 - \mu_2)(2\mu_2 + 1) + (\mu_2 - 1)(\mu_1 + 2\mu_2) (R_2/R_1)^3}{2(\mu_1 - \mu_2)(\mu_2 - 1) + (\mu_2 + 2)(\mu_1 + 2\mu_2) (R_2/R_1)^3} R_2^3 H_0. \quad (4.31)$$

Once the responses of the target and the original coated spheres have been written in terms of two dipoles, the condition for achieving illusion becomes $m_{sc} = m_s$, which reads

$$\frac{(\mu_1 - \mu_2)(2\mu_2 + 1) + (\mu_2 - 1)(\mu_1 + 2\mu_2) (R_2/R_1)^3}{2(\mu_1 - \mu_2)(\mu_2 - 1) + (\mu_2 + 2)(\mu_1 + 2\mu_2) (R_2/R_1)^3} R_2^3 = \frac{\mu - 1}{\mu + 2} R^3. \quad (4.32)$$

Given the original sphere (with radius R_1 and permeability μ_1), Eq. (4.32) provides the required shell properties (R_2 and μ_2) to attain the illusion of a target sphere (with radius R and permeability μ). For a fixed radius R_2 , there are, in general, two possible values of the permeability μ_2 to achieve the illusion. One of them is always negative and the other one can be positive or negative depending on the parameters. Therefore, there are some magnetic illusions that can be attained with shells with positive permeability and others that require negative-permeability.

One can understand why some magnetic illusions cannot be achieved by shells with positive permeability by analysing the magnetic response of both the target sphere and the original coated sphere. Consider an original sphere of positive permeability $\mu_1 > 0$ surrounded by a spherical shell with positive permeability $\mu_2 > 0$. The response of this coated sphere is bounded; for any pair of μ_1 and μ_2 , the response cannot be neither more attractive than that of a ferromagnetic sphere of radius R_2 nor more repulsive than that of a perfect diamagnetic sphere of radius R_2 . Thus, target spheres exhibiting larger magnetic field responses, such as ferromagnetic spheres with radius $R > R_2$, are unattainable with illusion devices with positive permeability. If, instead, one considers illusion devices with negative values of the permeability $\mu_2 < 0$, the response of the coated sphere is unbounded and the illusion of arbitrary target spheres becomes possible.

Two particular cases of magnetic illusion are cloaking and magnification/shrinking of an object [27, 91, 9, 93]. The illusion device properties (μ_2 and R_2) for achieving cloaking, i.e. for making an object magnetically undetectable, are obtained by setting $\mu = 1$ in Eq. (4.32), while the properties for achieving magnification/shrinking, i.e. for modifying the size of an object, are achieved by setting $\mu = \mu_1$ and $R \neq R_1$ in Eq. (4.32). Examples of two cloaking and two magnification illusions for the same original sphere are shown in Figs. 4.10a-c and in Figs. 4.10d-f, respectively. Different from the concentrators with extremely anisotropic positive permeability studied in Chapter 3, which could enlarge magnetic objects in a bounded manner, illusion devices with

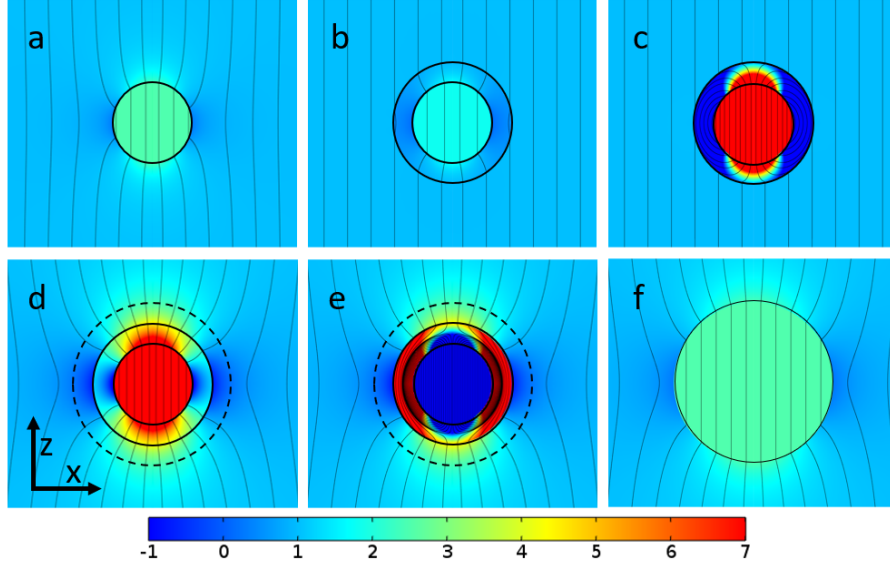


Figure 4.10: Numerical calculations of the magnetic induction field lines and, in colors, $B_z/(\mu_0 H_0)$ for a uniform magnetic field H_0 applied along the z -direction to different objects. In (a) a sphere of radius R_1 and permeability $\mu_1 = 10$. In panels (b), (c), (d) and (e) this same sphere is surrounded by illusion devices extending from R_1 to $R_2 = 1.5R_1$ and permeability (b) $\mu_2 = 0.49$, (c) $\mu_2 = -10.18$, (d) $\mu_2 = -1.51$, and (e) $\mu_2 = -19.34$. The devices in (b) and (c) make the sphere magnetically undetectable, while the devices in (d) and (e) make the sphere undistinguishable from a sphere of magnified radius $R = 2R_1$ and the same permeability $\mu = \mu_1 = 10$ (f). The dashed lines in (d) and (e) indicate the inner border of the region of illusion, $r = R$.

negative permeability offer the possibility of enlarging magnetic objects even beyond the shell. This is the case for the magnification illusions in Figs. 4.10d and e: the illusion devices achieve the same field distribution as that of a magnified object of radius $R > R_2$ (Fig. 4.10f). In these cases, the region of illusion is $r > R$. If, instead, the radius of the illusion device is larger than the radius of the target sphere, $R < R_2$, the region of illusion is the whole external region $r > R_2$.

When the original sphere exhibits an extreme permeability value ($\mu_1 \rightarrow \infty$ or $\mu_1 \rightarrow 0$), Eq. (4.32) gives a single solution for the illusion device permeability μ_2 ,

$$\mu_2(\mu_1 \rightarrow \infty) = \left(\frac{R_2^3 - R_1^3}{2R_1^3 + R_2^3} \right) \frac{(\mu + 2)R_2^3 + 2(\mu - 1)R^3}{(\mu + 2)R_2^3 - (\mu - 1)R^3}, \quad (4.33)$$

$$\mu_2(\mu_1 \rightarrow 0) = \left(\frac{2R_2^3 + R_1^3}{2(R_2^3 - R_1^3)} \right) \frac{(\mu + 2)R_2^3 + 2(\mu - 1)R^3}{(\mu + 2)R_2^3 - (\mu - 1)R^3}. \quad (4.34)$$

Interestingly, the first fractions in Eqs. (4.33) and (4.34) (in parenthesis) correspond to the required shell permeabilities to cancel the magnetic response of a ferromagnetic sphere ($\mu_1 \rightarrow \infty$) [84] and a perfect diamagnetic sphere ($\mu_1 \rightarrow 0$) [82], respectively.

The second term is the same in both equations and does not depend on the original object. In this way one can regard the illusion device permeability as the combination of a term responsible for cancelling the response of the original object and another term responsible for creating the response of the target sphere. This is reminiscent of the first proposal for achieving illusion for electromagnetic waves [26], in which the illusion device consisted of a complementary media that cancelled the original object and a restoring media that created the target. In our case, a single material with μ_2 would simultaneously do both tasks.

4.2.2 Emulating illusion devices with active metamaterials

In the previous section we have seen that some illusions require spherical shells (illusion devices) with negative permeability. As discussed in Sec. 4.1.3, even though there are not naturally occurring materials with $\mu < 0$ in magnetostatics, active metamaterials consisting of sets of electric currents can be used to artificially emulate their behaviour [141]. For an adequate replacement of the spherical shell of negative permeability with currents, one has to take into account that the shell surrounds a magnetic sphere that interacts with both the applied field and the currents fed to the shell volume. As a starting point, we calculate from Eqs. (1.11) and (1.12) the volume \mathbf{J}_M and the surface \mathbf{K}_M magnetization currents of the coated sphere. Since we assume μ_1 and μ_2 to be linear, homogeneous, and isotropic, then $\mathbf{J}_M = 0$. The surface current densities are calculated from the magnetization M_θ , which can be written in terms of the magnetic field as $M_\theta = (\mu_\theta - 1)H_\theta$ [Eq. (1.13)], where H_θ is, in turn, found from the magnetic scalar potential [Eq. (2.1)]. The two surface magnetization currents, flowing at the spherical surfaces $r = R_1$ and $r = R_2$, are

$$\mathbf{K}_{M_1} = \mathbf{K}_M(r = R_1) = (\mu_2 - \mu_1) \left(b_{cs} + \frac{c_{cs}}{R_1^3} \right) \sin(\theta) \mathbf{u}_\varphi, \quad (4.35)$$

$$\mathbf{K}_{M_2} = \mathbf{K}_M(r = R_2) = - \left(b_{cs} + \frac{c_{cs}}{R_2^3} \right) \sin(\theta) \mathbf{u}_\varphi. \quad (4.36)$$

These two current densities create the same magnetic induction field distribution as that of a coated sphere in all space. The current \mathbf{K}_{M_1} can be regarded as the superposition of a current density that substitutes the sphere plus a current density that substitutes the shell. For achieving magnetic illusion, the original sphere is present and, therefore, only the spherical shell must be substituted by currents. In this situation, the spherical shell can be substituted by the current density \mathbf{K}_{M_2} in Eq. (4.36) flowing at $r = R_2$ plus a current density found from Eq. (1.12) as

$$\mathbf{K}'_{M_1} = (\mu_2 - 1) \left(b_{cs} + \frac{c_{cs}}{R_1^3} \right) \sin(\theta) \mathbf{u}_\varphi, \quad (4.37)$$

flowing at $r = R_1$.

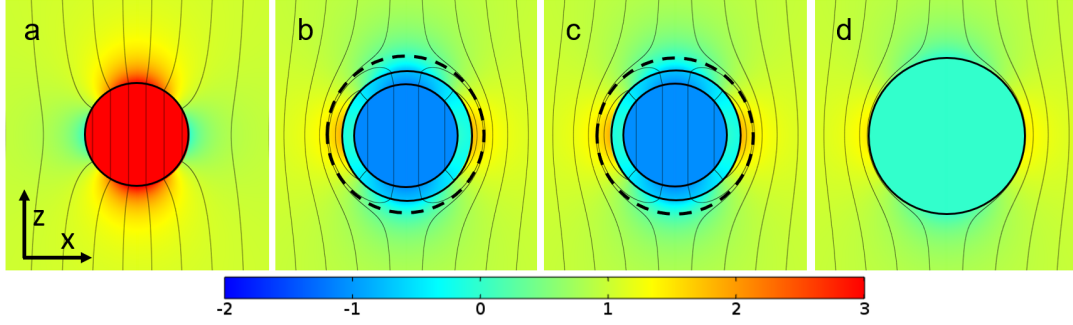


Figure 4.11: Numerical calculations of the magnetic induction field lines and, in colors, $B_z/(\mu_0 H_0)$ for a uniform field H_0 applied along the z -direction. (a) A ferromagnetic sphere with permeability $\mu_1 = 10^4$ and radius R_1 , (b) the same sphere surrounded by an illusion device with permeability $\mu_2 = -0.0942$ extending from R_1 to $R_2 = 1.25R_1$, (c) the sphere in (a) surrounded by the currents \mathbf{K}_{M_2} in Eq. (4.39) for the case $\mu_2 = -0.0942$ and $R_2 = 1.25R_1$, and (d) a diamagnetic sphere with permeability $\mu = 10^{-4}$ and radius $R = 1.5R_1$.

As an example on how magnetic illusion can be achieved with active metamaterials, consider an original ferromagnetic sphere ($\mu_1 \rightarrow \infty$) with radius R_1 . As shown in Fig. 4.11a, this sphere attracts the applied magnetic field lines. Our goal is to transform its magnetic signature into that of a perfect diamagnetic sphere ($\mu \rightarrow 0$) with different radius R , which, as illustrated in Fig. 4.11d, expels the applied magnetic field lines. To this end, the ferromagnetic sphere is surrounded with a spherical shell that acts as the illusion device. According to Eq. (4.33), the required shell permeability to achieve the targeted illusion is

$$\mu_2 = \frac{-2(R^3 - R_2^3)(R_2^3 - R_1^3)}{(R_2^3 + 2R_1^3)(R^3 + 2R_2^3)}. \quad (4.38)$$

Equation (4.38) shows that illusion devices with radius fulfilling $R_1 < R_2 < R$ require negative values of the permeability μ_2 . Thus, an active metamaterial consisting of the current densities in Eqs. (4.36) and (4.37) is needed. Interestingly, for the case $\mu_1 \rightarrow \infty$ the surface current density \mathbf{K}'_{M_1} tends to zero ($b_{cs} \rightarrow -c_{cs}/R_1^3$), and only the current density \mathbf{K}_{M_2} is required. For the particular case of transforming a ferromagnetic sphere into a perfect diamagnetic one, the currents that have to be fed at $r = R_2$ are obtained from Eq. (4.36) as

$$\mathbf{K}_{M_2} = \mathbf{K}_M(r = R_2) = -\frac{3}{2} \left(\frac{R^3 + 2R_1^3}{R_2^3 + 2R_1^3} \right) H_0 \sin\theta \mathbf{u}_\varphi. \quad (4.39)$$

Figure 4.11c shows that the magnetic field distribution in the region of illusion ($r > R$) when a ferromagnetic sphere is surrounded by the current distribution in Eq. (4.39) is exactly the same as the field distribution created by the sphere coated by a $\mu_2 < 0$ shell (Fig. 4.11b) and by the target illusion (Fig. 4.11d).

While illusion optics usually involves materials with cumbersome distributions of permittivity and permeability (often obtained by transformation optics) [26], illusion in magnetostatics only requires a precise arrangement of electric currents. This strategy, reminiscent of the proposals of active metasurfaces for camouflaging objects for electromagnetic waves [152, 153, 156] has some practical advantages. First, there is no need of designing and constructing bulk material structures with precise and complex permeability distributions. Second, the illusion devices are fully controllable; they can be easily turned on and off at will. One can even transform the magnetic signature of an object into different ones by dynamically controlling and tuning the currents. Third, the illusion devices do not lose their properties for intense magnetic fields. The last property is particularly interesting for the case of cloaking. One of the major drawbacks of passive magnetic cloaks [71, 74] is that their constituting materials lose their properties and become non-linear for strong magnetic fields. If one uses active cloaks based on the present strategy this problem can be circumvented. However, the intensity of the applied field also limits the applicability of active devices, since the current densities required to emulate negative-permeability materials in the presence of strong magnetic fields may be unachievable in practice. Another advantage of active cloaks is that, different from the passive cloaking proposals studied in [71, 74, 70], active cloaks do not require superconducting materials and can work at room temperature. A strategy for cloaking without superconductors based on these ideas has recently been proposed [162].

4.2.3 Experimental realization of illusion in magnetostatics

To verify the magnetic illusion theory and to demonstrate its potential, the illusion of transforming the signature of a ferromagnetic sphere ($\mu_1 \rightarrow \infty$) into that of its antagonistic material, a perfect diamagnetic sphere ($\mu \rightarrow 0$) is experimentally realized [111]. For the sake of generality, the target sphere is chosen larger than the original one ($R > R_1$) in order to transform both the material permeability and size (Fig. 4.12).

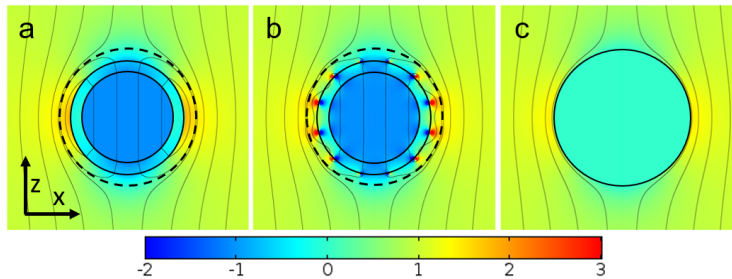


Figure 4.12: Numerical calculations of the magnetic induction field lines and $B_z/(\mu_0 H_0)$ (in colors) for a uniform magnetic field H_0 applied along the z -direction to (a) a ferromagnetic ($\mu_1 = 10^4$) sphere of radius R_1 surrounded by an illusion device with permeability $\mu_2 = -0.0942$ extending from R_1 to $R_2 = 1.25R_1$, (b) the same sphere surrounded by the discretized version of the illusion device in (a), consisting of 6 current loops placed at the surface $r = R_2$, and (c) a diamagnetic ($\mu = 10^{-4}$) sphere of radius $R = 1.5R_1$.

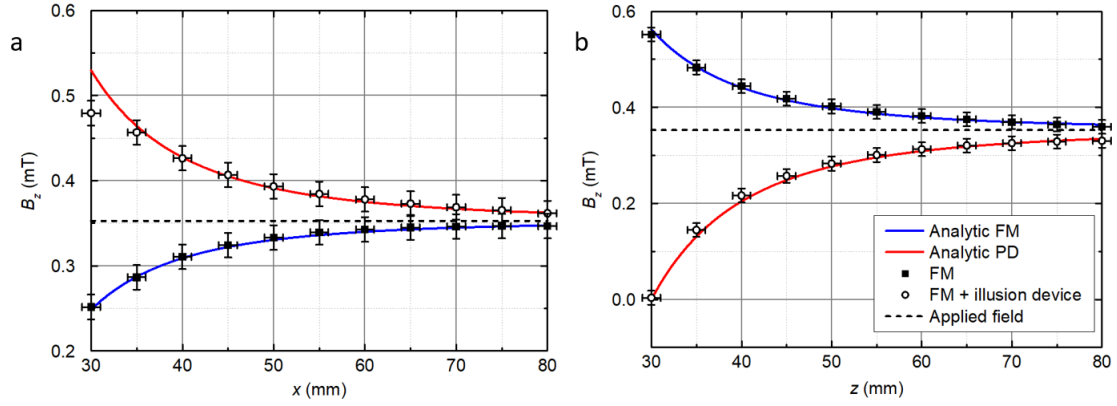


Figure 4.13: Experimental measurements of the z -component of \mathbf{B} for the bare ferromagnetic sphere (solid symbols) and for the ferromagnetic sphere surrounded by the illusion device (open symbols) along the (a) x -axis ($y = z = 0$), and (b) z -axis ($x = y = 0$). The analytic responses of a ferromagnetic (FM) sphere of relative permeability $\mu_1 = 10^4$ and radius $R_1 = 20\text{mm}$ (blue line) and a perfect diamagnetic (PD) sphere of relative permeability $\mu = 10^{-4}$ and radius $R = 30\text{mm}$ (red line) are also plotted.

In the experiments, the original sphere is a solid steel sphere of radius $R_1 = 20\text{mm}$. First, the magnetic response of this sphere is measured to guarantee that it can be qualified as an ideal ferromagnetic sphere. The sphere is placed at the central region of a pair of Helmholtz coils that generate a constant magnetic induction along the z -direction $B_0 = \mu_0 H_0 = 0.353\text{ mT}$ (taking into account the contribution of the Earth magnetic field). The z -component of the magnetic induction is measured with a Hall probe along the x and z axes (Fig. 4.13). Measurements (solid symbols) agree very well with the analytic response of a sphere with permeability $\mu_1 \rightarrow \infty$ (blue lines).

The external radius of the spherical shell (illusion device) is $R_2 = 25\text{mm}$ and the radius of the target illusion is $R = 30\text{mm}$. The required permeability for the shell, obtained from Eq. (4.38), is $\mu_2 = -0.0942$. Equation (4.39) gives the surface current density that emulates this negative-permeability shell. For the practical realization, this current density is converted into a discrete set of current loops. The intensity that has to be fed to each of these loops is calculated from Eq. (4.26). Numerical calculations show that the field distribution in the illusion region ($r > R$) for a discretized illusion device consisting of 6 current loops placed at $R_2 = 25\text{mm}$ and at the azimuthal angles $\theta_1 = 15^\circ$, $\theta_2 = 45^\circ$, $\theta_3 = 75^\circ$, $\theta_4 = 105^\circ$, $\theta_5 = 135^\circ$, and $\theta_6 = 165^\circ$ approximates very well the field distribution resulting from the ideal negative-permeability illusion device (Figs. 4.12a and b). The loops are precisely positioned at the required angles thanks to a 3D-printed non-magnetic plastic former of radius R_2 that has grooves at the appropriate positions, as shown in the inset of Fig. 4.14. The currents are fed using a common voltage source from an Agilent 6671A power supply and a set of load resistors that provide each loop with a different current according to Eq. (4.26). The original

ferromagnetic sphere surrounded by the illusion device is placed in the central region of the Helmholtz coils, as shown in the picture in Fig. 4.14, and the z component of the magnetic induction is measured with a Hall probe along both the z -axes and the x -axes (Fig. 4.13). The good agreement between the measurements (open symbols) and the analytic results for a perfect diamagnetic sphere (red lines) demonstrates that the magnetic signature of a ferromagnetic sphere has been successfully transformed into that of a perfect diamagnetic sphere.

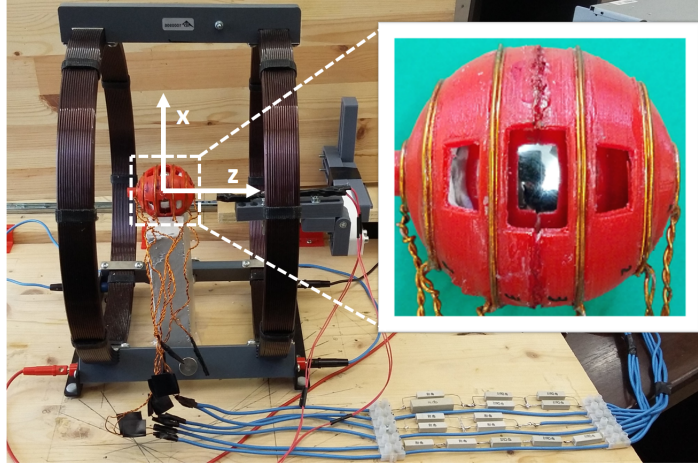


Figure 4.14: Picture of the experimental setup for achieving magnetic illusion. A ferromagnetic sphere is surrounded by a negative- μ metamaterial shell consisting of 6 current loops adequately positioned on a plastic former, as shown in the inset, and is placed in the middle of a pair of Helmholtz coils.

The magnetostatic illusion theory has been developed and experimentally verified for spherical objects in uniform applied fields. It is possible to extend the theory to other geometries and other applied fields, but the experimental realization of the illusion device would be more complex than the one presented above because it would require the emulation of inhomogeneous and/or anisotropic permeability distributions. This sets two practical complications. First, not only surface but also volume current densities could be required and, second, the current densities could show complicate expressions difficult to discretize into a finite set of current loops.

The illusion we have experimentally realized can be considered a *predetermined* illusion, as defined in [163] for the case of active cloaks. Because the currents that emulate the illusion device are specific to the magnitude of the applied magnetic field [Eq. (4.39)], we have first measured the applied magnetic field and then fed the required currents to the loops. If the applied field was changed, the illusion of the target sphere would be lost. By incorporating sets of sensors and feedback loops to the experiment, as in [141], one could achieve magnetic illusion for any uniform applied magnetic field.

4.3 Perfect magnetic lenses: emulating sources remotely

Most of the devices for controlling electromagnetic waves that have been developed using transformation optics and metamaterials have an analogy for the case of static magnetic fields, including magnetic cloaks [70, 71], magnetic concentrators [74] and magnetic wormholes [82]. After the realization of active metamaterials exhibiting a negative value of the permeability in magnetostatics [111] a question arises as to whether it could be possible to devise a magnetic device analogous to a perfect lens, one of the most intriguing devices that negative refraction has brought [17, 164].

John Pendry, based on the ideas of Victor Veselago [15], showed that lenses with $n = -1$ can be used to overcome the diffraction limit, a fundamental limitation on the resolution of conventional lenses, which cannot resolve details finer than the wavelength of the electromagnetic fields. Lenses with $n = -1$, known as *perfect lenses*, exhibit the extraordinary property of sub-wavelength focusing of electromagnetic fields, which makes the perfect reconstruction of an object possible [17, 165, 166, 18]. As shown in Figs. 4.15a and b, flat perfect lenses create perfect images that are exactly the same size as the object [167], while cylindrical and spherical perfect lenses can create magnified images of the objects [168, 169]. Soon after the first theoretical proposals of perfect lenses, sub-wavelength resolution was experimentally demonstrated [170, 171, 172, 173, 174, 175].

Inspired by these ideas, in this section we derive and study the properties of perfect lenses for the case of static magnetic fields: perfect magnetic lenses. We present a cylindrical perfect lens that not only can achieve strong magnetic field concentrations but also, similar to a cylindrical perfect lens for electromagnetic waves, can create magnified images of the magnetic objects placed inside its hole. For example, a perfect magnetic lens surrounding a magnetic dipole creates in its exterior the same magnetic field distribution as that of an image dipole, with different position and magnified dipolar magnetic moment, as sketched in Fig. 4.15c. We will show that, even though magnetostatic Maxwell equations forbid the creation of sources in empty space, the result in Fig. 4.15c can be well approximated in a large region of space. These results could eventually be used to create and to cancel magnetic sources at a distance, something unachievable with magnetic materials with positive permeability.

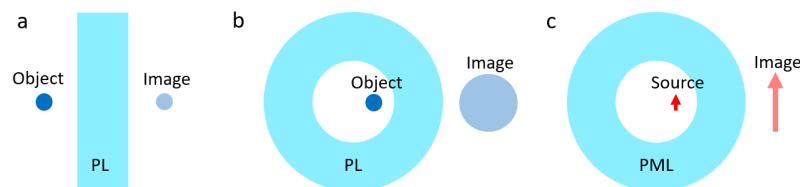


Figure 4.15: Sketch of a flat perfect lens (PL) (a), a cylindrical perfect lens (b), and a cylindrical perfect magnetic lens (PML) (c).

4.3.1 Derivation of a perfect magnetic lens with transformation optics

A cylindrical perfect magnetic lens is derived using transformation optics. By using this technique, one does not only obtain the permeability resulting in a perfect lens but also how the lens transforms a general magnetic field distribution.

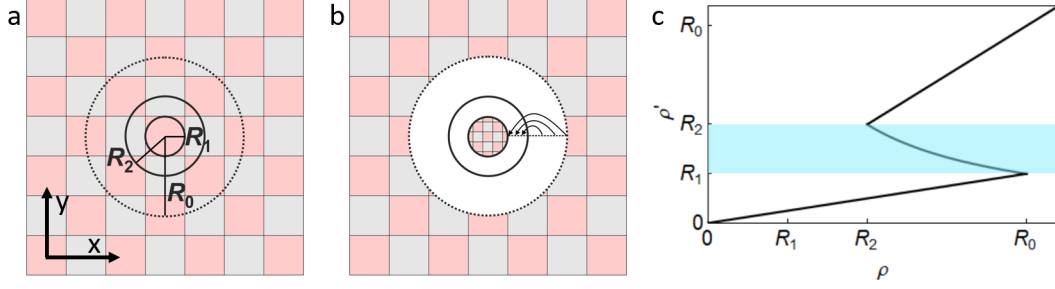


Figure 4.16: Panels (a) and (b) illustrate the space transformation resulting in a perfect magnetic lens when considering magnetic field sources located outside the lens volume, and panel (c) shows the associated radial coordinate transformation. The blue region indicates the perfect magnetic lens region.

We start with the case of having a perfect lens in the presence of an external applied magnetic field. The space transformation is illustrated in Fig. 4.16. Consider a cylindrical shell infinitely long along the z -direction with internal radius R_1 and external radius R_2 and a cylinder of radius $R_0 > R_2$. The space in the region $0 < \rho \leq R_0$ is radially compressed through the transformation

$$\begin{cases} \rho' = \left(\frac{R_1}{R_0}\right) \rho, \\ \varphi' = \varphi, \\ z' = z, \end{cases} \quad \rho \in (0, R_0), \quad (4.40)$$

where ρ, φ and z are the coordinates in the original physical space and ρ', φ' and z' are the coordinates in the transformed virtual space. Simultaneously, the space $R_2 < \rho < R_0$ is folded (arrows in Fig. 4.16b) as

$$\begin{cases} \rho' = R_2 \left(\frac{\rho}{R_2}\right)^k, \\ \varphi' = \varphi, \\ z' = z. \end{cases} \quad \rho \in [R_2, R_0]. \quad (4.41)$$

To guarantee the continuity of the space at $\rho = R_0$, a relation between k and R_0 arises from Eqs. (4.40) and (4.41),

$$R_0 = R_2 \left(\frac{R_1}{R_2}\right)^{1/k}, \quad (4.42)$$

which indicates that k is a negative parameter ranging from $k \rightarrow -\infty$ ($R_0 \rightarrow R_2$) to $k \rightarrow 0^-$ ($R_0 \rightarrow \infty$).

By applying Eqs. (1.19) and (1.20) of the transformation optics theory, we obtain the permeability that a cylindrical shell must have in order to shape the magnetic fields in the same way as the transformed space. Expressed in the cylindrical basis, the obtained relative permeability tensors are,

$$\mu' = \begin{pmatrix} \mu_{\rho\rho} & \mu_{\rho\varphi} & \mu_{\rho z} \\ \mu_{\varphi\rho} & \mu_{\varphi\varphi} & \mu_{\varphi z} \\ \mu_{z\rho} & \mu_{z\varphi} & \mu_{zz} \end{pmatrix} = \begin{pmatrix} 1 & 0 & 0 \\ 0 & 1 & 0 \\ 0 & 0 & \left(\frac{R_1}{R_2}\right)^{2/k-2} \end{pmatrix}, \quad (4.43)$$

in the internal region $\rho' < R_1$,

$$\mu' = \begin{pmatrix} k & 0 & 0 \\ 0 & 1/k & 0 \\ 0 & 0 & \frac{1}{k} \left(\frac{\rho'}{R_2}\right)^{2/k-2} \end{pmatrix}, \quad (4.44)$$

in the cylindrical shell region $R_1 \leq \rho' \leq R_2$, and $\mu' = 1$ in the external region, $\rho' > R_2$, where the space is not transformed.

As discussed in Sec. 3.1.1, the material requirements given by Eqs. (4.43) and (4.44) can be simplified under certain assumptions. If one considers a static magnetic field independent of the z -coordinate and without z -component, the problem has translational symmetry along the z -axis and only the left-upper 2x2 minors of the tensors have physical relevance. In this case, Eq. (4.43) shows that a perfect magnetic lens, different from the proposals for electromagnetic waves [176, 177, 9], does not require magnetic material neither inside the hole nor in the external region. According to Eq. (4.44), the required relative magnetic permeability for achieving a perfect magnetic lens is homogeneous and anisotropic, with radial and angular components $\mu_{\rho\rho} = k$ and $\mu_{\varphi\varphi} = 1/k$, respectively. Since k was defined as a negative parameter, there are infinite possible anisotropic perfect magnetic lenses, all with negative values of both $\mu_{\rho\rho}$ and $\mu_{\varphi\varphi}$. All these lenses exhibit different properties, since they result from different space transformations [Eqs. (4.40)-(4.42)].

The analytic expression for the magnetic field in all regions of space is found from Eq. (1.22) and the space transformations in Eqs. (4.40) and (4.41) as

$$\mathbf{H}'(\rho', \varphi') = \left(\frac{R_1}{R_2}\right)^{1/k-1} \mathbf{H}\left(\left(\frac{R_1}{R_2}\right)^{1/k-1} \rho', \varphi'\right), \quad \rho' \in [0, R_1), \quad (4.45)$$

$$\begin{cases} H'_\rho(\rho', \varphi') = \frac{1}{k} \left(\frac{\rho'}{R_2}\right)^{1/k-1} H_\rho\left(R_2 \left(\frac{\rho'}{R_2}\right)^{1/k}, \varphi'\right), \\ H'_\varphi(\rho', \varphi') = \left(\frac{\rho'}{R_2}\right)^{1/k-1} H_\varphi\left(R_2 \left(\frac{\rho'}{R_2}\right)^{1/k}, \varphi'\right), \end{cases} \quad \rho' \in [R_1, R_2], \quad (4.46)$$

$$\mathbf{H}'(\rho', \varphi') = \mathbf{H}(\rho', \varphi'), \quad \rho' \in (R_2, \infty). \quad (4.47)$$

Equation (4.47) indicates that the field in the external region, $\rho' \in (R_2, \infty)$, is not modified by the presence of the shell. The field distributions inside the shell, $\rho' \in [R_1, R_2]$, and inside the hole, $\rho' \in [0, R_1)$, depend on the applied magnetic field. For example, for the case of a uniform applied magnetic field, \mathbf{H}_0 , one finds using Eq. (4.45) that the field inside the shell hole, H^{INT} , is

$$\mathbf{H}^{\text{INT}} = \left(\frac{R_2}{R_1}\right)^{1-1/k} \mathbf{H}_0. \quad (4.48)$$

Equation (4.48) shows that perfect magnetic lenses concentrate uniform applied magnetic fields inside their holes. The concentration ratio tends to R_2/R_1 for lenses with $k \rightarrow -\infty$ and increases to ∞ as $k \rightarrow 0^-$ because the shell concentrates larger volumes of space inside its hole [Eq. (4.40), Fig. 4.16].

When the applied magnetic field is not uniform, the field distribution inside the hole can also be written in terms of the applied field. Consider now that there is a two-dimensional dipolar magnetic field source located outside the perfect magnetic lens, at $\rho = \rho_0 > R_2$ and $\varphi = \varphi_0$, with dipolar magnetic moment per unit length \mathbf{m}_0 . From Eq. (4.45) one obtains that the field distribution inside the hole is equivalent to that of an image dipole, located at

$$\rho_i = \left(\frac{R_1}{R_2}\right)^{1-1/k} \rho_0, \quad \varphi_i = \varphi_0, \quad (4.49)$$

with a reduced dipolar magnetic moment,

$$\mathbf{m}_i = \left(\frac{R_1}{R_2}\right)^{1-1/k} \mathbf{m}_0. \quad (4.50)$$

The image position is the same for any magnetic field source placed at ρ_0 and φ_0 , but the magnetic strength of the image depends on the considered magnetic field source; only the dipolar magnetic moment is reduced by a factor $(R_1/R_2)^{1-1/k}$.

According to Eqs. (4.45) and (4.49), when a magnetic source is located outside the folding region, $\rho_0 > R_0$, the image appears at $R_1 < \rho_i < \rho_0$, i.e. closer to but not inside the hole. In this case, the lens concentrates the field inside its hole because the reduction of the image strength [Eq. (4.50)] is compensated by the fact that the image appears closer to the hole. Solutions of this kind are also found when assuming positive-permeability materials [178, 74]. In contrast, when the sources are placed within the folding region, $R_2 < \rho_0 < R_0$, the image appears inside the lens hole, at $\rho_i < R_1$. This seems to indicate that the lens is able to create magnetic sources at a distance from its surfaces. The creation of magnetic images in empty space is, however, not possible. Magnetostatic Maxwell equations (1.9) and (1.10) indicate that magnetic field lines can only emanate from actual magnetic sources. This makes it impossible to achieve the same field distribution as if a source was located in empty space ($\rho < R_1$) if no real source is actually placed there. Therefore, the transformation optics results for the cases in

which the folding region contains magnetic sources have only physical validity if actual magnetic sources are placed at the image location. Perfect lenses for electromagnetic waves derived by transformation optics show similar limitations [179]. This result will be analysed further in Sec. 4.3.2

Once we have analysed the behaviour of perfect magnetic lenses with magnetic field sources located in their exterior, we consider the case of having magnetic field sources located inside the hole of the lens. A space transformation different from that in Eqs. (4.40) and (4.41) is required in order to understand how perfect magnetic lenses transform magnetic fields generated inside their holes. Considering a cylindrical shell infinitely long along the z -direction with internal radius R_1 and external radius R_2 and a cylinder of radius $R_0 < R_1$, the space is transformed as illustrated in Fig. 4.17.

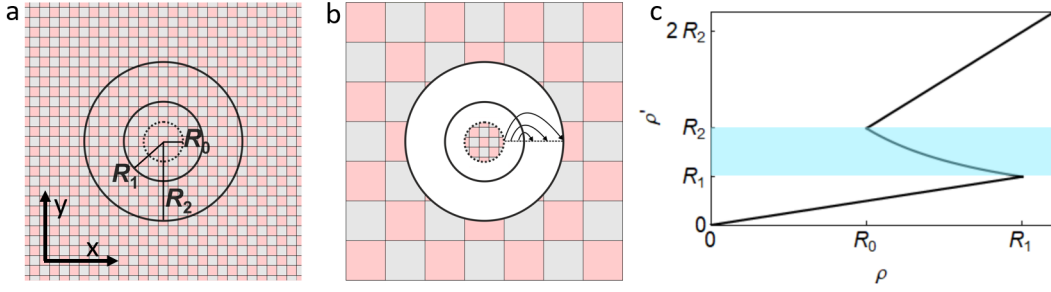


Figure 4.17: Panels (a) and (b) illustrate the space transformation resulting in a perfect magnetic lens with $k = -1$ for the case of having magnetic sources inside the hole of the lens, and panel (c) shows the associated radial coordinate transformation.

The space in the region $R_0 \leq \rho < \infty$ is expanded through

$$\begin{cases} \rho' = \left(\frac{R_2}{R_0}\right) \rho, \\ \varphi' = \varphi, \\ z' = z, \end{cases} \quad \rho \in (R_0, \infty), \quad (4.51)$$

and, simultaneously, the space $R_0 < \rho < R_1$ is folded (arrows in Fig. 4.17b) as

$$\begin{cases} \rho' = R_1 \left(\frac{\rho}{R_1}\right)^k, \\ \varphi' = \varphi, \\ z' = z. \end{cases} \quad \rho \in [R_0, R_1]. \quad (4.52)$$

As above, k is a negative parameter ranging from 0^- to $-\infty$. To guarantee the continuity of the space at $\rho' = R_2$, Eqs. (4.51) and (4.52) give the following relation between k and R_0 ,

$$R_0 = R_1(R_2/R_1)^{1/k}. \quad (4.53)$$

Similar as before, Eqs. (1.19) and (1.20) of the transformation optics theory are applied to obtain the permeability resulting in the presented space transformation. For

simplicity, we limit our study to problems with translational symmetry along z . In this way, we obtain that the permeability in the regions $\rho' > R_2$ and $\rho' < R_1$ must be $\mu = 1$ (air), while in the region $R_1 < \rho' < R_2$ a material with anisotropic relative permeability $\mu_{\rho\rho} = k$ and $\mu_{\varphi\varphi} = 1/k$, which constitutes the perfect magnetic lens, is required.

The analytic expression for the magnetic field in all regions of space is found from Eq. (1.22) and the space transformations in Eqs. (4.51) and (4.52) as

$$\mathbf{H}'(\rho', \varphi') = \mathbf{H}(\rho', \varphi'), \quad \rho' \in [0, R_1), \quad (4.54)$$

$$\begin{cases} H'_\rho(\rho', \varphi') = \frac{1}{k} \left(\frac{\rho'}{R_1}\right)^{1/k-1} H_\rho\left(R_1 \left(\frac{\rho'}{R_1}\right)^{1/k}, \varphi'\right), \\ H'_\varphi(\rho', \varphi') = \left(\frac{\rho'}{R_1}\right)^{1/k-1} H_\varphi\left(R_1 \left(\frac{\rho'}{R_1}\right)^{1/k}, \varphi'\right), \end{cases} \quad \rho' \in [R_1, R_2], \quad (4.55)$$

$$\mathbf{H}'(\rho', \varphi') = \left(\frac{R_2}{R_1}\right)^{1/k-1} \mathbf{H}\left(\left(\frac{R_2}{R_1}\right)^{1/k-1} \rho', \varphi'\right), \quad \rho' \in (R_2, \infty). \quad (4.56)$$

Equation (4.54) indicates that the field inside the hole, $\rho' \in [0, R_1)$, is not modified by the presence of the shell. The field distributions inside the shell, $\rho' \in [R_1, R_2]$, and in the external region, $\rho' \in (R_2, \infty)$, are transformed by the lenses according to Eqs. (4.55) and (4.56), respectively.

As an example, we analyse how a perfect magnetic lens transforms the field created by a magnetic dipole. Consider a long dipole of magnetic moment per unit length \mathbf{m}_0 placed inside the hole of the cylindrical perfect magnetic lens with the permeability in Eq. (4.44). The position of the long dipole in cylindrical coordinates is $\rho = \rho_0 < R_1$ and $\varphi = \varphi_0$, as sketched in Fig. 4.18. Equation (4.56) indicates that the field distribution outside the lens corresponds to the field of an image dipole located at

$$\rho_i = \left(\frac{R_2}{R_1}\right)^{1-1/k} \rho_0, \quad \varphi_i = \varphi_0, \quad (4.57)$$

with a magnified dipolar magnetic moment per unit length

$$\mathbf{m}_i = \left(\frac{R_2}{R_1}\right)^{1-1/k} \mathbf{m}_0. \quad (4.58)$$

These equations show that perfect magnetic lenses achieve a strong expulsion of the magnetic field inside their volume. As occurred when considering sources in the external region, the behaviour of the lens depends on the position of the inner source. If the source is placed outside the folding region, $\rho_0 < R_0$, the field in all the external region is that of an image source, as sketched in Fig. 4.18a. However, if the source is placed in the folding region, $R_0 < \rho_0 < R_1$, the image appears at a distance from the external surface of the lens, at $\rho_i > R_2$ (Fig. 4.18b). As discussed above for the case of external sources, because magnetic field lines can only emanate from magnetic sources, this latter result is not physical unless a magnetic source is actually placed at ρ_i .

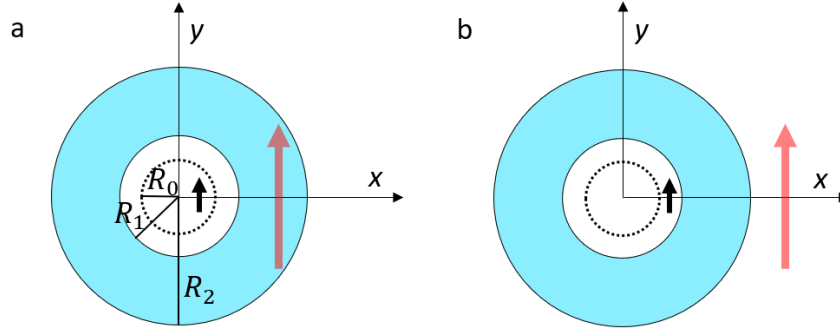


Figure 4.18: Sketch of two cylindrical perfect magnetic lenses of internal radius R_1 and external radius R_2 with a long (along z) magnetic dipole (black arrow) placed inside their holes, at $\rho = \rho_0 < R_1$. The dotted line indicates the folding radius R_0 . In (a) $\rho_0 < R_0$ and the field in the external region corresponds to the field created by an image dipole (red arrow) located inside the lens. In (b) $\rho_0 > R_0$ and the image dipole appears outside the lens. The length of the arrows indicates the strength of the dipolar magnetic moment.

In the following section we investigate further on the behaviour of perfect magnetic lenses and, specially, on the possibility of creating magnetic sources at a distance by solving magnetostatic Maxwell equations.

4.3.2 Study of perfect magnetic lenses with Maxwell equations

Once we have obtained by transformation optics the required magnetic permeability tensors to achieve a cylindrical perfect magnetic lens, we study its magnetic response following a different approach, by solving magnetostatic Maxwell equations. Consider the perfect magnetic lens in Fig. 4.18; a long cylindrical shell with internal radius R_1 , external radius R_2 , radial relative permeability $\mu_{\rho\rho} = k$ and angular relative permeability $\mu_{\varphi\varphi} = 1/k$. A long magnetic dipole with magnetic moment per unit length $(m_x, m_y) = (0, m_0)$ is placed inside the shell hole, at $(x, y) = (\rho_0, 0)$. The magnetic scalar potential created by this dipole can be written as the Fourier series

$$\phi_D = \begin{cases} -\frac{m_0}{2\pi\rho_0} \sum_{n=1}^{\infty} \left(\frac{\rho}{\rho_0}\right)^n \sin(n\varphi), & \rho \leq \rho_0, \\ \frac{m_0}{2\pi\rho_0} \sum_{n=1}^{\infty} \left(\frac{\rho_0}{\rho}\right)^n \sin(n\varphi), & \rho > \rho_0. \end{cases} \quad (4.59)$$

We focus on the particular case of having a magnetic dipolar source inside the shell hole, but a similar procedure can be applied to obtain the field distribution for any other source placed inside the hole or outside the lens. Because there are not free currents involved in the problem, the magnetic field can be obtained as the gradient of a magnetic scalar potential ϕ in all the space. The general solution for the scalar potential inside the hole (INT), in the shell (SHE) and in the external region (EXT) is found to be,

$$\phi_{\text{PL}}^{\text{INT}} = \phi_{\text{D}} + \sum_{n=1}^{\infty} a_n \rho^n \sin(n\varphi), \quad (4.60)$$

$$\phi_{\text{PL}}^{\text{SHE}} = \sum_{n=1}^{\infty} b_n \rho^{n/k} \sin(n\varphi) + \sum_{n=1}^{\infty} \frac{c_n}{\rho^{n/k}} \sin(n\varphi), \quad (4.61)$$

$$\phi_{\text{PL}}^{\text{EXT}} = \sum_{n=1}^{\infty} \frac{d_n}{\rho^n} \sin(n\varphi), \quad (4.62)$$

where we have taken into account that the potential must be finite at $\rho = 0$ and tend to zero when $\rho \rightarrow \infty$. By applying magnetostatic boundary conditions [Eqs. (1.14) and (1.15)] at $\rho = R_1$ and $\rho = R_2$, the potential coefficients are obtained as

$$a_n = 0, \quad (4.63)$$

$$b_n = 0, \quad (4.64)$$

$$c_n = \frac{m}{2\pi\rho_0} \frac{1}{R_1^{(1-1/k)n}} \rho_0^n, \quad (4.65)$$

$$d_n = \frac{m}{2\pi\rho_0} \left(\frac{R_2}{R_1} \right)^{(1-1/k)n} \rho_0^n. \quad (4.66)$$

The study of the derived potentials leads to some general properties of cylindrical perfect magnetic lenses. We focus on two main results. First, the solution for the magnetic scalar potential inside the hole $\phi_{\text{PL}}^{\text{INT}}$ confirms that the lens does not distort the magnetic scalar potential created inside its hole, as we had obtained from transformation optics [Eq. (4.54)]. This property is observed in Fig. 4.19; the fields inside the hole of the lenses in Figs. 4.19b and f are exactly the same as those of the bare dipoles shown in Figs. 4.19a and e, respectively. Second, the magnetic scalar potential in the external region $\phi_{\text{PL}}^{\text{EXT}}$ is found to be equivalent to that created by the image dipole obtained by transformation optics, with dipolar magnetic moment and position given by Eqs. (4.58) and (4.57), respectively. The dipolar strength and the position of these image dipoles are sketched as light red arrows in Figs. 4.19d and h. However, this equivalence is only valid in the region $\rho > \rho_i$; when the image appears outside the lens, $\rho_i > R_2$, the magnetic scalar potential in the region $\rho \in (R_2, \rho_i)$ is not convergent. These results are observed by comparing the field distribution outside the lenses in Figs. 4.19b and f with the field created by the image dipoles in Figs. 4.19c and g, respectively. In Fig. 4.19f the region $\rho \in (R_2, \rho_i)$ is painted in white to indicate that the field diverges.

Perfect lenses with $k = -1$ exhibit an extra property, which can also be noticed in Figs. 4.19b and f. The magnetic scalar potential in the lens volume is equivalent to the field of another image dipole (sketched as a blue arrow in Figs. 4.19d and h). The magnetic moment of this image is $\mathbf{m}_{i2} = -(R_1/\rho_0)^2 \mathbf{m}_0$ and its position is $\rho_{i2} = R_1^2/\rho_0$ and $\varphi_{i2} = \varphi_0$. When this image appears in the material volume, $R_1 < \rho_{i2} < R_2$, the magnetic field in the region $\rho \in (\rho_{i2}, R_2)$ (painted in white in Fig. 4.19f) is not convergent.

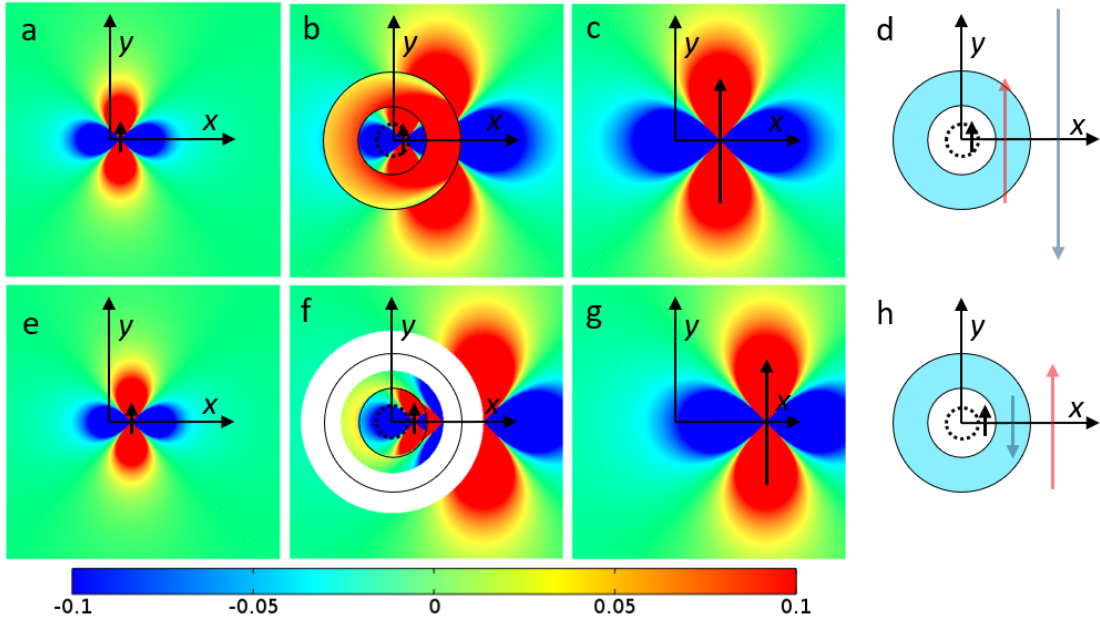


Figure 4.19: Numerical calculations of the normalized magnetic induction $B_y R_1^2 / (\mu_0 m_0)$ for (a) a long dipole (black arrow) of magnetic moment per unit length $(m_x, m_y) = (0, m_0)$ placed at $(x, y) = (\rho_0, 0)$, (b) the dipole in (a) surrounded by a perfect magnetic lens with internal radius $R_1 = 3\rho_0$, external radius $R_2 = 2R_1$, and permeability $\mu_{\rho\rho} = \mu_{\varphi\varphi} = -1$, (c) a dipole of magnetic moment $(0, 4m_0)$ placed at $(4\rho_0, 0)$, (e) a dipole of magnetic moment $(0, m_0)$ placed at $(2\rho_0, 0)$, (f) the dipole in (e) surrounded by the perfect magnetic lens in (b), and (g) a dipole of magnetic moment $(0, 4m_0)$ placed at $(8\rho_0, 0)$. Panels (d) and (h) sketch the original dipole (black arrow) and the image dipoles (red arrow and blue arrow) for the perfect lens (blue region) configurations in (b) and (f), respectively. The dotted line in (b), (d), (f), and (h) indicates the boundary of the folding region, $\rho = R_0 = R_1^2 / R_2$. In (a)-(d), $\rho_0 < R_0$, while in (e)-(h), $R_0 < \rho_0 < R_1$. The white annular regions in (f) indicate that the field diverges.

The annular regions of divergences that appear in perfect magnetic lenses have been previously studied in the quasistatic regime and are known as regions of *anomalous localized resonances* [180, 181, 182]. Interestingly, these divergences make it possible to achieve the field of an image source in the region $\rho > \rho_i$ without the need of placing an extra source at ρ_i . Because the field in the region $\rho \in (R_2, \rho_i)$ is not the field of the image source, an image can appear at $\rho_i > R_2$ without violating magnetostatic Maxwell equations; a cumbersome and strong (infinite) field distribution is adequately generated inside the lens volume in such a way that the field reaching the region $\rho > \rho_i$ is equivalent to the field created by a source placed at ρ_i . These regions of anomalous localized resonances are discussed further in the following section.

4.3.3 Creating and cancelling magnetic sources with perfect lenses

Cylindrical perfect magnetic lenses have been shown to exhibit a linear, homogeneous, and anisotropic magnetic permeability. According to Eq. (4.44), their radial and angular relative permeability fulfill $\mu_{\rho\rho} = k$ and $\mu_{\varphi\varphi} = 1/\mu_{\rho\rho} = 1/k$, respectively. Because k is a negative parameter, the permeability of perfect lenses is always negative. As explained in the previous sections, negative permeability values in magnetostatics can be emulated in practice by active metamaterials consisting of suitably tailored sets of electric currents adequately arranged in space [141, 111]. This strategy is reminiscent of the active perfect magnetic lenses for electromagnetic waves presented in [183, 184], based on two metasurfaces characterized by their impedances that substitute the $n = -1$ material constituting the lens.

As discussed in Sec. 4.1.3, the currents that emulate a material with negative permeability can be found from the material magnetization. In general, a cylindrical perfect magnetic lens with internal radius R_1 and external radius R_2 can be substituted by a volume current density \mathbf{J}_M and two surface current densities, flowing at the surfaces $\rho = R_1$ and $\rho = R_2$. For the next discussion, we focus on perfect magnetic lenses with $k = -1$ because they are isotropic ($\mu_{\rho\rho} = \mu_{\varphi\varphi} = -1$) and their emulation does not require volume currents, $\mathbf{J}_M = 0$.

Consider a long (along z) dipole with magnetic moment per unit length $(m_x, m_y) = (0, m_0)$ located inside the perfect lens hole, at $(x, y) = (\rho_0, 0)$, as depicted in Fig. 4.18. The magnetic scalar potential in all space is given by Eqs. (4.60)-(4.66). The surface current densities required to emulate the lens, $\mathbf{K}_1 = \mathbf{K}_M(\rho = R_1)$ and $\mathbf{K}_2 = \mathbf{K}_M(\rho = R_2)$, are obtained from Eq. (1.12) by writing the magnetization in terms of the magnetic field, $M_\varphi = -2H_\varphi$ [Eq. (1.13)], which is, in turn, obtained from the magnetic scalar potential [Eq. (2.1)]. When the external field corresponds to the field of an image dipole located in the material volume, $\rho_i \leq R_2$ (Fig. 4.18a), the lens can be emulated by

$$\mathbf{K}_1 = \frac{m_0}{\pi\rho_0 R_1} \sum_{n=1}^{\infty} \left(\frac{\rho_0}{R_1}\right)^n n \cos(n\varphi) \mathbf{u}_z = \frac{m_0[-2R_1\rho_0 + (R_1^2 + \rho_0^2)\cos\varphi]}{\pi(R_1^2 + \rho_0^2 - 2\rho_0 R_1 \cos\varphi)^2} \mathbf{u}_z, \quad (4.67)$$

$$\mathbf{K}_2 = \frac{-m_0}{\pi\rho_0 R_2} \sum_{n=1}^{\infty} \left(\frac{R_2\rho_0}{R_1^2}\right)^n n \cos(n\varphi) \mathbf{u}_z = \frac{m_0[2R_1^2 R_2 \rho_0 - (R_1^4 + R_2^2 \rho_0^2)\cos\varphi]}{\pi[R_1^2 + \left(\frac{R_2}{R_1}\right)^2 \rho_0^2 - 2R_2 \rho_0 \cos\varphi]^2} \mathbf{u}_z. \quad (4.68)$$

When surrounding the dipole by these current densities, the field distribution in Fig. 4.19b is exactly recovered. However, when the image appears outside the material volume, $\rho_i > R_2$ (Fig. 4.18b), the magnetic scalar potential diverges at $\rho = R_2$, resulting in a divergence of the current distribution \mathbf{K}_2 ; the sum in Eq. (4.68) is not convergent. In spite of this and even though all the infinite terms of the current distribution in Eq. (4.68) are required for achieving the exact field of the image dipole, one can truncate the sum up to a finite number of terms n_T and obtain a field distribution that approximates well the field of the image dipole at $\rho > \rho_i$. In this case, the surface current densities that approximately emulate a perfect magnetic lens are \mathbf{K}_1 in Eq. (4.67) and

$$\mathbf{K}_2 = \frac{-m_0}{\pi\rho_0 R_2} \sum_{n=1}^{n_T} \left(\frac{R_2 \rho_0}{R_1^2} \right)^n n \cos(n\varphi) \mathbf{u}_z. \quad (4.69)$$

In Fig. 4.20 three field distributions resulting from the current densities in Eqs. (4.67) and (4.69) are shown for the cases $n_T = 5$, $n_T = 10$, and $n_T = 20$. It can be seen that the larger the number of terms n_T the more the field resembles that of the ideal material with $\mu_{\rho\rho} = \mu_{\varphi\varphi} = -1$. The shell does not distort the field of the dipole inside the hole and creates the field of an image dipole of magnetic moment \mathbf{m}_i located at $\rho = \rho_i$ in the region $\rho > \rho_i$ (red arrow in Fig. 4.20d) and the field of another image dipole of magnetic moment \mathbf{m}_{i2} located at $\rho = \rho_{i2}$ in the region $R_1 < \rho < \rho_{i2}$ (blue arrow in Fig. 4.20d).

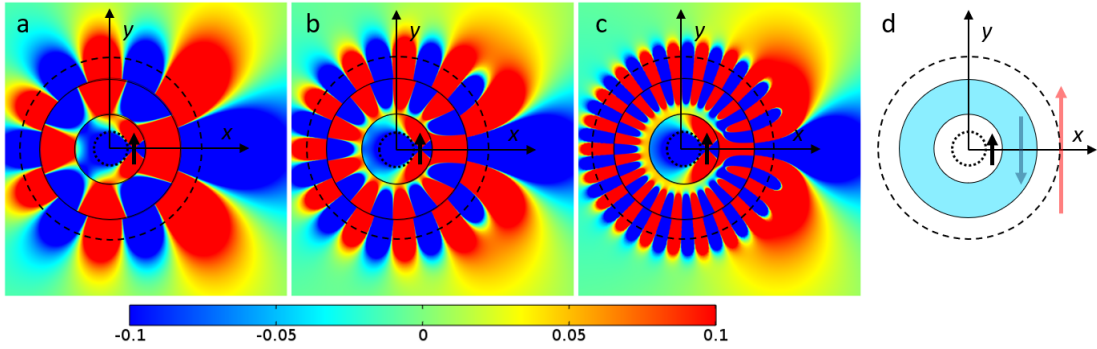


Figure 4.20: In panels (a)-(c), numerical calculations of the normalized magnetic induction $B_y R_1^2 / (\mu_0 m_0)$ resulting from a dipole (black arrow) of magnetic moment per unit length $(m_x, m_y) = (0, m_0)$ placed at $(x, y) = (\rho_0, 0)$ surrounded by the current distributions in Eqs. (4.67) and (4.69) for the case $R_1 = 3/2\rho_0$, $R_2 = 2R_1$ and (a) $n_T = 5$, (b) $n_T = 10$, and (c) $n_T = 20$. In panel (d), a schetch illustrating the dipole images (blue and red arrows) that a perfect lens (blue region, extending from R_1 to R_2) creates when a dipole (black arrow) is placed inside its hole, at $(x, y) = (\rho_0, 0)$. The dotted line indicates the boundary of the folding region, $\rho = R_0 = R_1^2 / R_2$, and the dashed line indicates the position of the external image dipole $\rho_i = \rho_0 (R_2 / R_1)^2$.

The emulation of a perfect magnetic lens by an active metamaterial consisting of electric currents may be used to create magnetic sources at a distance. The two current densities in Eqs. (4.67) and (4.69) surrounding an original dipole are shown to create a dipole remotely in all the region $\rho > \rho_i$ (see Fig. 4.20). Interestingly, if the goal is to create a dipole at a distance the active metamaterial can be simplified. By analysing the field distribution the current \mathbf{K}_1 creates, one finds that this current density has two tasks. First, in the region $\rho < R_1$ it cancels the magnetic field created by the current \mathbf{K}_2 , which guarantees that the field inside the hole is not distorted by the presence of the currents. Second, in the region $\rho > R_1$ it cancels the field created by the original dipole.

This means that the current density \mathbf{K}_2 is the only responsible for creating the two image dipoles; the original dipole and the current density \mathbf{K}_1 are not required for creating a dipole at a distance. Rewriting Eq. (4.69) in terms of the image dipole parameters, \mathbf{m}_i and ρ_i , one finds that the current density that has to be fed to a cylindrical surface of radius R to create a dipole of magnetic moment per unit length $(0, m_D)$ at $(\rho_D, 0)$ is

$$\mathbf{K}_D(\rho = R) = \frac{m_D}{\pi \rho_D R_1} \sum_{n=1}^{\infty} \left(\frac{\rho_D}{R}\right)^n n \cos(n\varphi) \mathbf{u}_z. \quad (4.70)$$

This current density could eventually be used to remotely cancel the field created by a long (along z) small magnet, which can be approximated by a long dipolar source. \mathbf{K}_D can be used to create the field of a magnetic dipole with the same magnetic moment as the magnet that needs to be cancelled but pointing in the opposite direction. An example of the cancellation of a long dipole at a distance is shown in Fig. 4.21.

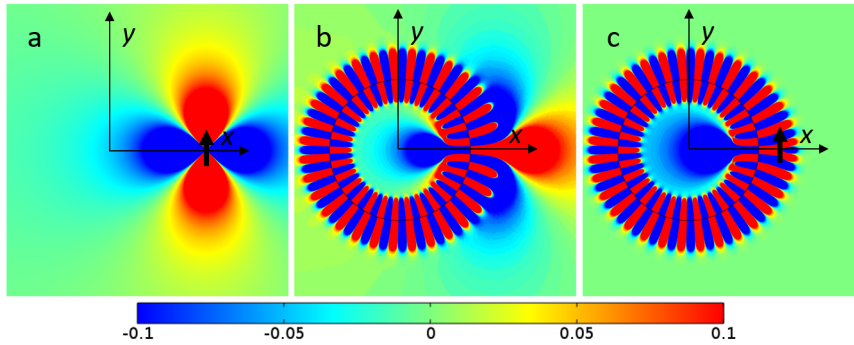


Figure 4.21: Numerical calculations of the normalized magnetic induction $B_y R_1^2 / (\mu_0 m_0)$ for (a) a long dipole (black arrow) of magnetic moment per unit length $(m_x, m_y) = (0, m_0)$ placed at $(x, y) = (x_0, 0)$, (b) the current distribution in Eq. (4.70) for $\rho_D = x_0$, $m_D = -m_0$, $R = 3x_0/4$, and $n_T = 30$, and (c) the dipole in (a) plus the current density in (b).

Similar active metasurfaces can create/cancel other magnetic sources remotely. It is particularly interesting to analyse the case of current wires, since most magnetic field sources can be regarded as combinations of them. For example, the field created by a dipole can be well approximated by the field created by two long straight antiparallel wires placed close to each other.

Consider a straight wire with current I placed inside the hole of a perfect magnetic lens with internal radius R_1 , external radius R_2 and anisotropic permeability $\mu_{\rho\rho} = k$ and $\mu_{\varphi\varphi} = 1/k$. The wire position is $\rho = \rho_0 < R_1$ and $\varphi = \varphi_0$. It can be found both with transformation optics and with Maxwell equations that the lens does not distort the field inside the hole and that the magnetic field in the external region corresponds to the field of an image wire of current I located at $\rho = \rho_i$ and $\varphi = \varphi_i$ [Eq. (4.57)]. Same as for the case of the dipolar source, when $\rho_i > R_2$ there is an annular region of divergent magnetic field between R_2 and ρ_i .

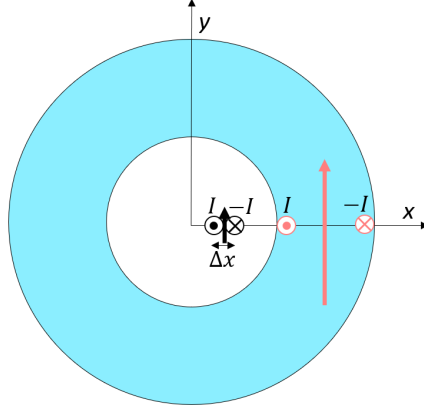


Figure 4.22: Sketch of a cylindrical perfect magnetic lens (blue region) surrounding two antiparallel long wires of current I and $-I$ separated by a distance Δx (shown in black). The resulting image wires are plotted in red. The black and the red arrows illustrate the strength and the position of the dipolar magnetic moment that the original and the image wires create, respectively.

The magnification of the dipolar magnetic moment given by Eq. (4.58) can be understood from this result. Consider two antiparallel straight wires with current I and $-I$ separated by a distance Δx , as shown in black in Fig. 4.22. The field created by these wires can be well approximated as the field of a long dipole with dipolar magnetic moment per unit length $(m_x, m_y) = (0, I\Delta x)$ located at the middle of the two wires (black arrow in Fig. 4.22). When surrounding these two wires by a perfect magnetic lens, the field in the external region corresponds to the field of two antiparallel image wires with current I and $-I$ placed at the positions given by Eq. (4.57) (shown in red in Fig. 4.22). Because the shell effectively increases the distance between the wires by a factor $(R_2/R_1)^{1-1/k}$ and the dipolar magnetic moment is proportional to the distance between the wires, the dipolar moment created by the wires is magnified (red arrow in Fig. 4.22), recovering in this way the result in Eq. (4.58).

Consider the case of an isotropic perfect magnetic lens with $\mu_{\rho\rho} = \mu_{\varphi\varphi} = -1$ surrounding a wire located at $(x, y) = (\rho_0, 0)$. The magnetic field in the shell region is equivalent to that created by two image wires; a wire with current I at $\rho_{i2} = R_1^2/\rho_0$ plus a wire with current $-I$ at $\rho_{i3} = 0$ (see Figs. 4.23b and f and the blue sketches of the wires in Figs. 4.23d and h). The two surface current densities that must be fed at $\rho = R_1$ and $\rho = R_2$ to emulate the perfect magnetic lens with this wire inside the hole are

$$\mathbf{K}_1^W = -\frac{I}{\pi R_1} \left(1 + \sum_{n=1}^{\infty} \left(\frac{\rho_0}{R_1} \right)^n \cos(n\varphi) \right) \mathbf{u}_z = -\frac{I}{\pi R_1} \left(1 - \frac{\rho_0(\rho_0 - R_1 \cos\varphi)}{R_1^2 + \rho_0^2 - 2R_1\rho_0 \cos\varphi} \right) \mathbf{u}_z, \quad (4.71)$$

$$\mathbf{K}_2^W = \frac{I}{\pi R_2} \left(1 + \sum_{n=1}^{\infty} R_1^{-2n} R_2^n \rho_0^n \cos(n\varphi) \right) \mathbf{u}_z. \quad (4.72)$$

Figure 4.23 shows that these two current densities act as a perfect magnetic lens both when the original wire is placed outside the folding region (Figs. 4.23a-d) and when it is placed within the folding region (Figs. 4.23e-h). For the latter, the sum in \mathbf{K}_2^W is truncated to $n_T = 30$ terms because it is not convergent. First, by comparing Figs. 4.23a and b and Figs. 4.23e and f, one observes that the field in the region $\rho < R_1$ is not distorted by the currents. Second, by comparing Figs. 4.23b and c and Figs. 4.23f and g, the field in the exterior of the current densities is found to be equivalent to that of an image wire (sketched in red in Figs. 4.23d and h, respectively) of current I located at $\rho = \rho_i$ in the region $\rho > \rho_i$. Same as for the case of a dipolar magnetic source, the only current density responsible for creating the image wire located at $\rho = \rho_{i2}$ is \mathbf{K}_2^W .

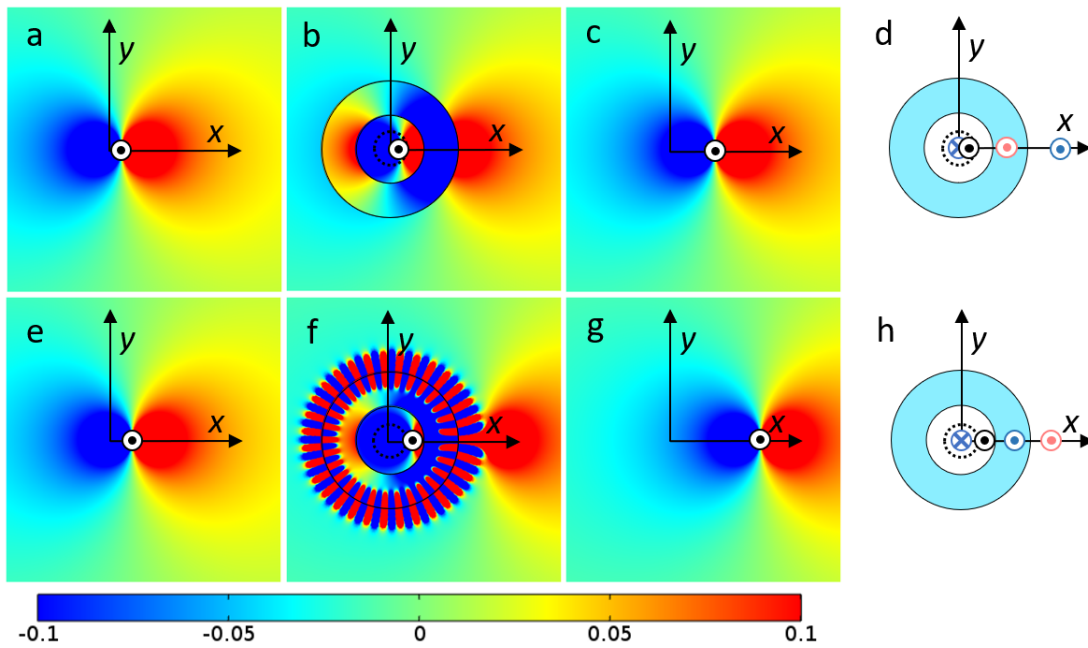


Figure 4.23: In panels (a)-(c) and (e)-(g), numerical calculations of the normalized magnetic induction $B_y R_1 / (\mu_0 I)$ a straight wire of current I (sketched as a black dot) creates in different configurations. In (a) the wire is placed at $(x, y) = (x_0, 0)$. In (b) the wire in (a) is surrounded by the current densities in Eqs. (4.71) and (4.72) for $R_1 = 3x_0$, $R_2 = 2R_1$ and $\rho_0 = x_0$. In (c) the wire is located at $(4x_0, 0)$. In (e) the wire is placed at $(2x_0, 0)$. In (f) the wire in (e) is surrounded by the current densities in Eqs. (4.71) and (4.72) (truncated to $n_T = 30$ terms) for $R_1 = 3x_0$, $R_2 = 2R_1$ and $\rho_0 = 2x_0$. In (g) the wire is placed at $(8x_0, 0)$. Panels (d) and (h) illustrate the creation of images achieved by a perfect magnetic lens with $\mu = -1$ (filled in light blue, extending from R_1 to R_2) when surrounding the wires in (a) and (e), respectively. The dotted lines in (b), (d), (f), and (h) indicate the inner boundary of the folding region $\rho = R_0 = R_1^2 / R_2$. The image wire sketched in red in (d) and (h) give the field distribution in the external region, while the image wires sketched in blue give the field distribution in the shell volume.

4.4 Chapter summary and conclusions

In this chapter, materials with a negative value of the static magnetic permeability have been introduced and studied as a natural extension to the case of positive-permeability materials. Active metamaterials based on currents have been proposed as a way to effectively emulate the properties of negative-permeability materials in practice. These currents are obtained from the material magnetization and depend on the applied magnetic field and on the material geometry and permeability. The theory has been demonstrated by the experimental realization of a spherical shell that produces the same magnetic induction field distribution as that of a spherical shell with $\mu = -1/2$ in a uniform applied field.

After introducing materials with negative static permeability, two applications of these materials have been studied. The first one has been the illusion of transforming the magnetic signature of an object into that of another one. While some particular cases of illusion, like magnetic cloaking for example, had already been achieved with positive-permeability materials, negative permeability makes it possible to disguise an original object as another object. The theory for transforming the magnetic signature of a sphere of arbitrary permeability into another sphere with different permeability and radius has been presented. The extreme transformation of a ferromagnetic sphere into that of its antagonistic material, a perfect diamagnet, has been experimentally realized to verify our ideas. The second application of negative permeability that has been studied is the possibility of creating perfect magnetic lenses, which are able to create magnified images of magnetic sources. Because approximate images may appear in empty space, these lenses could be used to create magnetic sources at a distance, something unachievable with positive permeability. The particular case of creating and cancelling a dipole at a distance has been studied in detail, but the theory could be applied to any magnetic field source. The idea of cancelling magnetic sources at a distance by active metamaterials with negative permeability is a first step towards the realization of a magnetic external cloak. While external cloaks that cancel the scattering of an object at a distance without the need of surrounding the object have already been proposed for electromagnetic waves [132, 185, 186, 187], analogous devices for the case of static magnetic fields have yet to be developed.

To sum up, materials with negative permeability have been shown to exhibit properties beyond those known for positive-permeability materials and can be regarded as a new tool for shaping, controlling, and even for creating static magnetic fields.

The understanding of magnetism and its interaction with magnetic materials has enabled the development of a wide range of technologies that are present in our daily life; magnetism is nowadays found at the basis of electric generators, computers, credit cards, and medical techniques such as magnetic resonance imaging and hyperthermia. In the last decade, the 'toolbox' for controlling static magnetic fields has been enriched thanks to the introduction of magnetic metamaterials and transformation optics, which have enabled the realization of intriguing devices such as magnetic cloaks, concentrators, and hoses. In this thesis, we have extended the results along this line to propose different metamaterial devices to shape magnetic fields in novel ways. We have not only considered the case of passive magnetic metamaterials with positive permeabilities, but also active magnetic metamaterials with negative permeabilities.

Since most magnetic metamaterials consist of arrangements of extreme-permeability materials, we have started by studying in detail the interaction of magnetic fields with perfect diamagnetic materials with $\mu \rightarrow 0$ and ideal ferromagnetic materials with $\mu \rightarrow \infty$. This study has shown that extreme-permeability materials exhibit some interesting features that remain yet to be exploited and could be further developed to achieve new magnetic field configurations. For example, we have demonstrated that one can use perfect diamagnetic materials to overlap the field created by several wires located at different points.

Once the properties of extreme-permeability materials have been discussed, we have presented different devices based on magnetic metamaterials with positive permeability. We have demonstrated that hollow magnetic metamaterials of different geometries with extremely anisotropic permeability (very large in the radial direction and small in the angular one) can achieve a strong concentration of magnetic field inside their holes, a

strong expulsion of the magnetic fields created inside their holes towards their exterior, and the magnification of the magnetic response of magnetic materials placed inside their holes. As another application of magnetic metamaterials, we have shown that isotropic multilayer shells can be used to cloak a magnetic sensor in such a way that it is able to detect the applied magnetic field while being magnetically undetectable.

Inspired by all the possibilities that negative refraction has enabled for the control of light, in the last part of the thesis we have studied the interaction of static magnetic fields with materials with negative permeabilities. Such materials do not naturally occur, but we have demonstrated that they can be emulated in practice as arrangements of free currents. Negative permeability has been applied to demonstrate how to transform the magnetic signature of an object into that of another one (magnetic illusion) and to theoretically derive the analogy of a perfect lens for the case of static magnetic fields. We think that these results are particularly relevant; the introduction of negative static permeability could lead to the realization of devices that have been explored for controlling light but have not yet an analogy in magnetostatics due to the lack of negative permeability media, such as the possibility of making an object undetectable remotely.

All the theoretical results we have presented, which have been derived directly from the magnetostatic Maxwell equations or by applying the transformation optics theory, have been confirmed by numerical calculations. Also, some of the theoretical ideas have been demonstrated with proof-of-principle experiments. We have experimentally verified that an anisotropic spherical shell with positive permeability discretized by a set of ferromagnetic funnels achieves a strong magnetic field concentration inside its hole, that negative permeability media can be effectively emulated by free currents and, finally, that negative permeability enables the illusion of transforming the magnetic signature of a ferromagnetic sphere into that of a larger perfect diamagnetic sphere.

The future work to extend the results presented in this thesis can be divided into two different lines. On the one hand, there are still experimental demonstrations that could be realized to verify some of the proposed theoretical strategies for shaping magnetic fields, such as the magnification ability of magnetic concentrators, the possibility of making a magnetic sensor undetectable, or the realization of a perfect magnetic lens. We are currently working on the latter experimental demonstration. We believe that the experimental realization of a perfect magnetic lens that enables the creation of magnetic sources at a distance could have a remarkable technological impact, specially because it would enable the focusing of strong magnetic fields. On the other hand, one could extend the results presented in this work by considering that actual magnetic materials are, in general, not linear. The consideration of non-linearities is not only important because it could set the limitations of the magnetic devices derived assuming linear media, but also because it could lead to new interesting effects.

Uniqueness theorems in magnetostatics

In this appendix, we demonstrate that the magnetic field distribution in a given volume is uniquely determined by the specification of the magnetic scalar/vector potential or its derivative at its boundaries.

A1 Magnetic scalar potential

Consider a volume V bounded by a surface S . If there are not free currents, $\mathbf{J}_f = 0$, the magnetic field in this volume fulfills $\nabla \times \mathbf{H} = 0$ and can be written in terms of a magnetic scalar potential ϕ as $\mathbf{H} = -\nabla\phi$. Let us assume $\nabla \cdot \mathbf{H} = 0$, so that ϕ fulfills the Laplace equation $\nabla^2\phi = 0$. Here we prove that the specification of the magnetic scalar potential ϕ along the surface S , known as Dirichlet boundary condition, uniquely determines the magnetic scalar potential through the volume V . Similar proofs are derived in [2, 4, 3] for electrostatics.

Suppose that there are two solutions for the magnetic scalar potential, ϕ_1 and ϕ_2 both fulfilling the Laplace equation in the volume V . ϕ_1 and ϕ_2 are specified at the bounding surface S , so that $\phi_1|_S = \phi_2|_S = \phi_S$. In this case, the difference potential, $\phi_3 = \phi_1 - \phi_2$, which also fulfills the Laplace equation, is specified at S as $\phi_3|_S = 0$.

Consider the relation

$$\nabla \cdot (\phi \nabla \phi) = (\nabla \phi)^2 + \phi \nabla^2 \phi. \quad (\text{A1})$$

For the difference magnetic scalar potential ϕ_3 , this expression leads to

$$\int_V (\nabla \phi_3)^2 dV = \int_V \nabla \cdot (\phi_3 \nabla \phi_3) dV = \oint_S \phi_3 \nabla \phi_3 d\mathbf{S} = \oint_S \phi_3 \frac{\partial \phi_3}{\partial n} dS, \quad (\text{A2})$$

where $\partial\phi_3/\partial n$ is the normal derivative of ϕ_3 and we have applied the divergence theorem.

Since we have considered $\phi_3|_S = 0$, we obtain

$$\int_V (\nabla\phi_3)^2 dV = 0, \quad (\text{A3})$$

which can only be satisfied if $\nabla\phi_3 = 0$ everywhere in the volume V . This leads to a constant value of ϕ_3 , which can only fulfill the condition $\phi_3|_S = 0$ if $\phi_3 = \phi_1 - \phi_2$ is zero. Therefore, the solution for the magnetic scalar potential in V is uniquely determined by the specification of the magnetic scalar potential along the surface S .

The magnetic scalar potential in the volume V is also uniquely determined (apart from an additive arbitrary constant) if the normal derivative of ϕ along the bounding surface S is specified. This is known as Neumann boundary condition. As above, assume there are two solutions for the magnetic scalar potential, ϕ_1 and ϕ_2 that fulfilling the Laplace equation in the volume V and that the normal derivative of ϕ_1 and ϕ_2 is specified at the bounding surface S , so that $(\partial\phi_1/\partial n)|_S = (\partial\phi_2/\partial n)|_S$. In this case, the normal derivative of the difference potential, $\phi_3 = \phi_1 - \phi_2$, at S is $(\partial\phi_3/\partial n)|_S = 0$, which according to Eq. (A2) also leads to Eq. (A3). Therefore ϕ_3 must be constant across the volume V . Thus, the solution for the magnetic scalar potential in the volume V is uniquely determined since apart from an additive arbitrary constant ct , ϕ_1 and ϕ_2 are equivalent ($\phi_1 = \phi_2 + ct$).

A2 Magnetic vector potential

Consider now that the volume V bounded by the surface S includes free currents. In this case, the magnetic field cannot be written in terms of a magnetic scalar potential because $\nabla \times \mathbf{H} = \mathbf{J}_f \neq 0$. Here we prove that if the free current density \mathbf{J}_f is specified through the volume V and the magnetic vector potential \mathbf{A} is specified on the surface S , the magnetic induction is uniquely determined through V (Dirichlet boundary condition).

Suppose that the magnetic vector potential is not uniquely determined and there are two solutions \mathbf{A}_1 and \mathbf{A}_2 that fulfill

$$\nabla \times \nabla \times \mathbf{A}_1 = \mu_0 \mu \mathbf{J}_f, \quad (\text{A4})$$

$$\nabla \times \nabla \times \mathbf{A}_2 = \mu_0 \mu \mathbf{J}_f, \quad (\text{A5})$$

through V . The magnetic vector potential at the bounding surface S is specified, so that $\mathbf{A}_1|_S = \mathbf{A}_2|_S = \mathbf{A}_S$. Consider now the difference magnetic vector potential $\mathbf{A}_3 = \mathbf{A}_1 - \mathbf{A}_2$, which fulfills

$$\nabla \times \nabla \times \mathbf{A}_3 = 0, \quad (\text{A6})$$

and $\mathbf{A}_3|_S = 0$. The difference magnetic induction \mathbf{B}_3 is therefore $\mathbf{B}_3 = \mathbf{B}_1 - \mathbf{B}_2 = \nabla \times \mathbf{A}_1 - \nabla \times \mathbf{A}_2$.

Consider now the relation,

$$(\nabla \times \mathbf{U})^2 - \mathbf{U} \cdot \nabla \times \nabla \times \mathbf{U} = \nabla \cdot \mathbf{U} \times (\nabla \times \mathbf{U}). \quad (\text{A7})$$

By setting $\mathbf{U} = \mathbf{A}_3$ and applying the divergence theorem we obtain

$$\int_V (\nabla \times \mathbf{A}_3)^2 dV = \int_V \nabla \cdot (\mathbf{A}_3 \times \mathbf{B}_3) dV = \oint_S \mathbf{A}_3 \times \mathbf{B}_3 d\mathbf{S}. \quad (\text{A8})$$

Since $\mathbf{A}_3|_S = 0$,

$$\int_V (\nabla \times \mathbf{A}_3)^2 dV = 0. \quad (\text{A9})$$

Because $(\nabla \times \mathbf{A}_3)^2$ is positive, this condition can only be satisfied if $\mathbf{B}_3 = \nabla \times \mathbf{A}_3 = 0$ through V . Therefore, the solution for the magnetic induction in V is unique, because $\mathbf{B}_3 = 0$ implies $\mathbf{B}_1 = \mathbf{B}_2$. Since $\nabla \times \mathbf{A}_3 = 0$, the difference magnetic vector potential in the volume V is a uniform field \mathbf{f} , indicating that the solution for the magnetic vector potential in V is uniquely determined except for a field \mathbf{f} that does not contribute to the magnetic field induction distribution ($\mathbf{A}_1 = \mathbf{A}_2 + \mathbf{f}$).

A similar derivation can be made to prove that if the free current density \mathbf{J}_f is specified through a volume V and the magnetic field induction \mathbf{B} is specified on the bounding surface S , the magnetic field induction is also uniquely determined through V and on S .

Bibliography

- [1] L. D. Landau and E. M. Lifshitz, *Electrodynamics of continuous media*. Butterworth-Heinemann, 1984.
- [2] J. D. Jackson, *Classical electrodynamics*. Wiley, 1999.
- [3] D. J. Griffiths, *Introduction to electrodynamics*. Pearson Education, 2014.
- [4] J. A. Stratton, *Electromagnetic Theory*. Hoboken, NJ, USA: John Wiley & Sons, Inc., oct 2015.
- [5] D.-X. Chen, J. Brug, and R. Goldfarb, “Demagnetizing factors for cylinders,” *IEEE Transactions on Magnetics*, vol. 27, pp. 3601–3619, jul 1991.
- [6] J. B. Pendry, A. Aubry, D. R. Smith, and S. A. Maier, “Transformation Optics and Subwavelength Control of Light,” *Science*, vol. 337, pp. 549–552, aug 2012.
- [7] J. B. Pendry, D. Schurig, and D. R. Smith, “Controlling electromagnetic fields,” *Science (New York, N.Y.)*, vol. 312, pp. 1780–2, jun 2006.
- [8] N. B. Kundtz, D. R. Smith, and J. B. Pendry, “Electromagnetic Design With Transformation Optics,” *Proceedings of the IEEE*, vol. 99, pp. 1622–1633, oct 2011.
- [9] H. Chen, C. T. Chan, and P. Sheng, “Transformation optics and metamaterials,” *Nature Materials*, vol. 9, pp. 387–396, may 2010.
- [10] D. Schurig, J. J. Mock, B. J. Justice, S. A. Cummer, J. B. Pendry, A. F. Starr, and D. R. Smith, “Metamaterial electromagnetic cloak at microwave frequencies,” *Science (New York, N.Y.)*, vol. 314, pp. 977–80, nov 2006.
- [11] T. J. Cui, D. R. Smith, and R. Liu, *Metamaterials : theory, design, and applications*. Springer, 2010.

- [12] J. Pendry, A. Holden, D. Robbins, and W. Stewart, "Magnetism from conductors and enhanced nonlinear phenomena," *IEEE Transactions on Microwave Theory and Techniques*, vol. 47, no. 11, pp. 2075–2084, 1999.
- [13] R. Kshetrimayum, "A brief intro to metamaterials," *IEEE Potentials*, vol. 23, pp. 44–46, jan 2005.
- [14] D. R. Smith, W. J. Padilla, D. C. Vier, S. C. Nemat-Nasser, and S. Schultz, "Composite Medium with Simultaneously Negative Permeability and Permittivity," *Physical Review Letters*, vol. 84, pp. 4184–4187, may 2000.
- [15] V. G. Veselago, "The electrodynamics of substances with simultaneously negative values of ϵ and μ ," *Soviet Physics Uspekhi*, vol. 10, pp. 509–514, apr 1968.
- [16] D. R. Smith, J. B. Pendry, and M. C. K. Wiltshire, "Metamaterials and negative refractive index," *Science (New York, N.Y.)*, vol. 305, pp. 788–92, aug 2004.
- [17] J. B. Pendry, "Negative Refraction Makes a Perfect Lens," *Physical Review Letters*, vol. 85, pp. 3966–3969, oct 2000.
- [18] X. Zhang and Z. Liu, "Superlenses to overcome the diffraction limit," *Nature Materials*, vol. 7, pp. 435–441, jun 2008.
- [19] N. I. Zheludev and Y. S. Kivshar, "From metamaterials to metadevices," *Nature Materials*, vol. 11, pp. 917–924, nov 2012.
- [20] U. Leonhardt and T. G. Philbin, "General relativity in electrical engineering," *New Journal of Physics*, vol. 8, pp. 247–247, oct 2006.
- [21] R. Fleury, F. Monticone, and A. Alù, "Invisibility and Cloaking: Origins, Present, and Future Perspectives," *Physical Review Applied*, vol. 4, p. 037001, sep 2015.
- [22] W. Wang, L. Lin, J. Ma, C. Wang, J. Cui, C. Du, and X. Luo, "Electromagnetic concentrators with reduced material parameters based on coordinate transformation," *Optics Express*, vol. 16, p. 11431, jul 2008.
- [23] W. X. Jiang, T. J. Cui, Q. Cheng, J. Y. Chin, X. M. Yang, R. Liu, and D. R. Smith, "Design of arbitrarily shaped concentrators based on conformally optical transformation of nonuniform rational B-spline surfaces," *Applied Physics Letters*, vol. 92, p. 264101, jun 2008.
- [24] M. Rahm, D. Schurig, D. A. Roberts, S. A. Cummer, and J. B. Pendry, "Design of electromagnetic cloaks and concentrators using form-invariant coordinate transformations of Maxwell's equations," *Photonics and Nanostructures - Fundamentals and Applications*, vol. 6, pp. 87–95, apr 2008.

- [25] J. Yang, M. Huang, C. Yang, Z. Xiao, and J. Peng, "Metamaterial electromagnetic concentrators with arbitrary geometries," *Optics Express*, vol. 17, p. 19656, oct 2009.
- [26] Y. Lai, J. Ng, H. Chen, D. Han, J. Xiao, Z.-Q. Zhang, and C. T. Chan, "Illusion Optics: The Optical Transformation of an Object into Another Object," *Physical Review Letters*, vol. 102, p. 253902, jun 2009.
- [27] W. X. Jiang, T. J. Cui, X. M. Yang, H. F. Ma, and Q. Cheng, "Shrinking an arbitrary object as one desires using metamaterials," *Applied Physics Letters*, vol. 98, p. 204101, may 2011.
- [28] Y. Luo, H. Chen, J. Zhang, L. Ran, and J. A. Kong, "Design and analytical full-wave validation of the invisibility cloaks, concentrators, and field rotators created with a general class of transformations," *Physical Review B*, vol. 77, p. 125127, mar 2008.
- [29] H. Chen, X. Luo, H. Ma, and C. Chan, "The Anti-Cloak," *Optics Express*, vol. 16, p. 14603, sep 2008.
- [30] G. Castaldi, I. Gallina, V. Galdi, A. Alù, and N. Engheta, "Cloak/anti-cloak interactions," *Optics Express*, vol. 17, p. 3101, mar 2009.
- [31] M. Wegener, "Metamaterials Beyond Optics," *Science*, vol. 342, pp. 939–940, nov 2013.
- [32] M. Kadic, T. Bückmann, R. Schittny, and M. Wegener, "Metamaterials beyond electromagnetism," *Reports on Progress in Physics*, vol. 76, p. 126501, dec 2013.
- [33] T. Han and C.-W. Qiu, "Transformation Laplacian metamaterials: recent advances in manipulating thermal and dc fields," *Journal of Optics*, vol. 18, p. 044003, apr 2016.
- [34] T. Han, H. Ye, Y. Luo, S. P. Yeo, J. Teng, S. Zhang, and C.-W. Qiu, "Manipulating DC Currents with Bilayer Bulk Natural Materials," *Advanced Materials*, vol. 26, pp. 3478–3483, jun 2014.
- [35] H. Xu, X. Shi, F. Gao, H. Sun, and B. Zhang, "Ultrathin Three-Dimensional Thermal Cloak," *Physical Review Letters*, vol. 112, p. 054301, feb 2014.
- [36] S. Narayana and Y. Sato, "Heat Flux Manipulation with Engineered Thermal Materials," *Physical Review Letters*, vol. 108, p. 214303, may 2012.
- [37] S. Guenneau, C. Amra, and D. Veynante, "Transformation thermodynamics: cloaking and concentrating heat flux," *Optics Express*, vol. 20, p. 8207, mar 2012.

- [38] J. Yang, M. Huang, C. Yang, and G. Cai, “A Metamaterial Acoustic Concentrator With Regular Polygonal Cross Section,” *Journal of Vibration and Acoustics*, vol. 133, p. 061016, dec 2011.
- [39] Y. Chen, H. Liu, M. Reilly, H. Bae, and M. Yu, “Enhanced acoustic sensing through wave compression and pressure amplification in anisotropic metamaterials,” *Nature Communications*, vol. 5, p. 5247, dec 2014.
- [40] T. Frenzel, M. Kadic, and M. Wegener, “Three-dimensional mechanical metamaterials with a twist,” *Science (New York, N.Y.)*, vol. 358, pp. 1072–1074, nov 2017.
- [41] D. Powell, “Core Concept: Mechanical metamaterials bend the rules of everyday physics,” *Proceedings of the National Academy of Sciences of the United States of America*, vol. 115, pp. 2545–2547, mar 2018.
- [42] B. Wood and J. B. Pendry, “Metamaterials at zero frequency,” *Journal of Physics: Condensed Matter*, vol. 19, p. 076208, feb 2007.
- [43] F. Magnus, B. Wood, J. Moore, K. Morrison, G. Perkins, J. Fyson, M. C. K. Wiltshire, D. Caplin, L. F. Cohen, and J. B. Pendry, “A d.c. magnetic metamaterial,” *Nature Materials*, vol. 7, pp. 295–297, apr 2008.
- [44] C. Navau, D.-X. Chen, A. Sanchez, and N. Del-Valle, “Magnetic properties of a dc metamaterial consisting of parallel square superconducting thin plates,” *Applied Physics Letters*, vol. 94, p. 242501, jun 2009.
- [45] Y. Mawatari, C. Navau, and A. Sanchez, “Two-dimensional arrays of superconducting strips as dc magnetic metamaterials,” *Physical Review B*, vol. 85, p. 134524, apr 2012.
- [46] P. G. de Gennes, *Superconductivity of metals and alloys*. Advanced Book Program, Perseus Books, 1999.
- [47] M. Cyrot and D. Pavuna, *Introduction to Superconductivity and High-Tc Materials*. World Scientific, jul 1992.
- [48] C. P. Poole, *Superconductivity*. Academic Press, 2007.
- [49] B. D. B. D. Cullity and C. D. C. D. Graham, *Introduction to magnetic materials*. IEEE/Wiley, 2009.
- [50] J. M. D. Coey, *Magnetism and Magnetic Materials*. Cambridge: Cambridge University Press, 2010.
- [51] R. W. Ziolkowski, “Propagation in and scattering from a matched metamaterial having a zero index of refraction,” *Physical Review E*, vol. 70, p. 046608, oct 2004.

- [52] I. Liberal and N. Engheta, “Near-zero refractive index photonics,” *Nature Photonics*, vol. 11, pp. 149–158, mar 2017.
- [53] I. Liberal and N. Engheta, “The rise of near-zero-index technologies,” *Science*, vol. 358, no. 6370, 2017.
- [54] M. Silveirinha and N. Engheta, “Tunneling of Electromagnetic Energy through Subwavelength Channels and Bends using ϵ -Near-Zero Materials,” *Physical Review Letters*, vol. 97, p. 157403, oct 2006.
- [55] B. Edwards, A. Alù, M. E. Young, M. Silveirinha, and N. Engheta, “Experimental Verification of Epsilon-Near-Zero Metamaterial Coupling and Energy Squeezing Using a Microwave Waveguide,” *Physical Review Letters*, vol. 100, p. 033903, jan 2008.
- [56] B. Edwards, A. Alù, M. G. Silveirinha, and N. Engheta, “Experimental Verification of Plasmonic Cloaking at Microwave Frequencies with Metamaterials,” *Physical Review Letters*, vol. 103, p. 153901, oct 2009.
- [57] N. Engheta, “Pursuing Near-Zero Response,” *Science*, vol. 340, pp. 286–287, apr 2013.
- [58] A. Alù, M. G. Silveirinha, A. Salandrino, and N. Engheta, “Epsilon-near-zero metamaterials and electromagnetic sources: Tailoring the radiation phase pattern,” *Physical Review B*, vol. 75, p. 155410, apr 2007.
- [59] M. Silveirinha and N. Engheta, “Design of matched zero-index metamaterials using nonmagnetic inclusions in epsilon-near-zero media,” *Physical Review B*, vol. 75, p. 075119, feb 2007.
- [60] I. Liberal and N. Engheta, “Manipulating thermal emission with spatially static fluctuating fields in arbitrarily shaped epsilon-near-zero bodies,” *Proceedings of the National Academy of Sciences of the United States of America*, vol. 115, pp. 2878–2883, mar 2018.
- [61] I. Liberal, Y. Li, and N. Engheta, “Magnetic field concentration assisted by epsilon-near-zero media,” *Philosophical Transactions of the Royal Society A: Mathematical, Physical and Engineering Sciences*, vol. 375, p. 20160059, mar 2017.
- [62] M. G. Silveirinha, “Trapping light in open plasmonic nanostructures,” *PHYSICAL REVIEW A*, vol. 89, p. 23813, 2014.
- [63] I. Liberal, A. M. Mahmoud, and N. Engheta, “Geometry-invariant resonant cavities,” *Nature communications*, vol. 7, p. 10989, mar 2016.
- [64] I. Liberal and N. Engheta, “Nonradiating and radiating modes excited by quantum emitters in open epsilon-near-zero cavities,” *Science Advances*, vol. 2, p. e1600987, oct 2016.

- [65] I. Liberal and N. Engheta, “Zero-index structures as an alternative platform for quantum optics.,” *Proceedings of the National Academy of Sciences of the United States of America*, vol. 114, pp. 822–827, jan 2017.
- [66] I. Liberal, A. M. Mahmoud, Y. Li, B. Edwards, and N. Engheta, “Photonic doping of epsilon-near-zero media.,” *Science (New York, N.Y.)*, vol. 355, pp. 1058–1062, mar 2017.
- [67] I. R. Ciric, “A New Scalar Potential Modeling Technique for Magnetic Fields Due to Arbitrary Distributions of Electric Current,” *IEEE Magnetism Letters*, vol. 4, pp. 0500104–0500104, 2013.
- [68] I. R. Ciric, “Scalar Potential Formulations for Magnetic Fields Produced by Arbitrary Electric Current Distributions in the Presence of Ferromagnetic Bodies,” *IEEE Transactions on Magnetism*, vol. 50, pp. 1–6, jan 2014.
- [69] A. Sanchez, C. Navau, J. Prat-Camps, and D.-X. Chen, “Antimagnets: controlling magnetic fields with superconductor–metamaterial hybrids,” *New Journal of Physics*, vol. 13, p. 093034, sep 2011.
- [70] S. Narayana and Y. Sato, “DC Magnetic Cloak,” *Advanced Materials*, vol. 24, pp. 71–74, jan 2012.
- [71] F. Gömöry, M. Solovyov, J. Souc, C. Navau, J. Prat-Camps, and A. Sanchez, “Experimental realization of a magnetic cloak.,” *Science (New York, N.Y.)*, vol. 335, pp. 1466–1468, mar 2012.
- [72] L. Kroon and K. Järrendahl, “Neutral shielding and cloaking of magnetic fields using isotropic media,” *Journal of Physics: Condensed Matter*, vol. 29, p. 035801, jan 2017.
- [73] W. Jiang, Y. Ma, J. Zhu, G. Yin, Y. Liu, J. Yuan, and S. He, “Room-temperature broadband quasistatic magnetic cloak,” *NPG Asia Materials*, vol. 9, pp. e341–e341, jan 2017.
- [74] C. Navau, J. Prat-Camps, and A. Sanchez, “Magnetic Energy Harvesting and Concentration at a Distance by Transformation Optics,” *Physical Review Letters*, vol. 109, p. 263903, dec 2012.
- [75] F. Sun and S. He, “Create a uniform static magnetic field over 50 T in a large free space region,” tech. rep., 2013.
- [76] F. Sun and S. He, “Dc magnetic concentrator and omnidirectional cascade cloak by using only one or two homogeneous anisotropic materials of positive permeability,” *Progress In Electromagnetics Research*, vol. 142, pp. 683–699, 2013.

- [77] F. Sun and S. He, “Static magnetic field concentration and enhancement using magnetic materials with positive permeability,” *Progress In Electromagnetics Research*, vol. 142, pp. 579–590, 2013.
- [78] K. Liu, W. Jiang, F. Sun, and S. He, “Experimental realization of strong dc magnetic enhancement with transformation optics,” *Progress In Electromagnetics Research*, vol. 146, pp. 187–194, 2014.
- [79] C. Navau, J. Prat-Camps, O. Romero-Isart, J. Cirac, and A. Sanchez, “Long-Distance Transfer and Routing of Static Magnetic Fields,” *Physical Review Letters*, vol. 112, p. 253901, jun 2014.
- [80] F. Sun and S. He, “Transformation inside a null-space region and a dc magnetic funnel for achieving an enhanced magnetic flux with a large gradient,” *Progress In Electromagnetics Research*, vol. 146, pp. 143–153, 2014.
- [81] O. Gargiulo, S. Oleschko, J. Prat-Camps, M. Zanner, and G. Kirchmair, “Fast flux control of 3D transmon qubits using a magnetic hose,” *Preprint arXiv:1811.10875*, nov 2018.
- [82] J. Prat-Camps, C. Navau, and A. Sanchez, “A Magnetic Wormhole,” *Scientific Reports*, vol. 5, p. 12488, dec 2015.
- [83] C. Navau, R. Mach-Batlle, A. Parra, J. Prat-Camps, S. Laut, N. Del-Valle, and A. Sanchez, “Enhancing the sensitivity of magnetic sensors by 3D metamaterial shells,” *Scientific Reports*, vol. 7, p. 44762, dec 2017.
- [84] R. Mach-Batlle, C. Navau, and A. Sanchez, “Invisible magnetic sensors,” *Applied Physics Letters*, vol. 112, p. 162406, apr 2018.
- [85] F. Sun and S. He, “Static magnetic field concentration and enhancement using magnetic materials with positive permeability,” *Progress In Electromagnetics Research*, vol. 142, pp. 579–590, 2013.
- [86] J. Prat-Camps, C. Navau, and A. Sanchez, “Experimental realization of magnetic energy concentration and transmission at a distance by metamaterials,” *Applied Physics Letters*, vol. 105, p. 234101, dec 2014.
- [87] J. Prat-Camps, C. Navau, and A. Sanchez, “Quasistatic Metamaterials: Magnetic Coupling Enhancement by Effective Space Cancellation,” *Advanced Materials*, vol. 28, pp. 4898–4903, jun 2016.
- [88] J. Zhang, Y. Luo, H. Chen, and B.-I. Wu, “Cloak of arbitrary shape,” *Journal of the Optical Society of America B*, vol. 25, p. 1776, nov 2008.
- [89] A. Nicolet, F. Zolla, and S. Guenneau, “Electromagnetic analysis of cylindrical cloaks of an arbitrary cross section,” *Optics Letters*, vol. 33, p. 1584, jul 2008.

- [90] J. Yang, M. Huang, C. Yang, Z. Xiao, and J. Peng, "Metamaterial electromagnetic concentrators with arbitrary geometries," *Optics Express*, vol. 17, p. 19656, oct 2009.
- [91] T. Yang, H. Chen, X. Luo, and H. Ma, "Superscatterer: Enhancement of scattering with complementary media," *Optics Express*, vol. 16, p. 18545, oct 2008.
- [92] X. Zang and C. Jiang, "Two-dimensional elliptical electromagnetic superscatterer and superabsorber," *Optics Express*, vol. 18, p. 6891, mar 2010.
- [93] R. F. Wang, Z. L. Mei, X. Y. Yang, X. Ma, and T. J. Cui, "Switchable invisibility cloak, anticloak, transparent cloak, superscatterer, and illusion for the Laplace equation," *Physical Review B*, vol. 89, p. 165108, apr 2014.
- [94] H.-X. Xu, G.-M. Wang, K. Ma, and T. J. Cui, "Superscatterer Illusions Without Using Complementary Media," *Advanced Optical Materials*, vol. 2, pp. 572–580, jun 2014.
- [95] G. D. Bai, Z. Zhang, F. Yang, and Z. L. Mei, "Magnification device for Laplace equation by using homogeneous and isotropic media with positive values," *Journal of Physics D: Applied Physics*, vol. 48, p. 325104, aug 2015.
- [96] Du-Xing Chen, E. Pardo, and A. Sanchez, "Radial magnetometric demagnetizing factor of thin disks," *IEEE Transactions on Magnetics*, vol. 37, no. 6, pp. 3877–3880, 2001.
- [97] J. Lenz and S. Edelstein, "Magnetic sensors and their applications," *IEEE Sensors Journal*, vol. 6, pp. 631–649, jun 2006.
- [98] P. Ripka and M. Janosek, "Advances in Magnetic Field Sensors," *IEEE Sensors Journal*, vol. 10, pp. 1108–1116, jun 2010.
- [99] M. Díaz-Michelena, Díaz-Michelena, and Marina, "Small Magnetic Sensors for Space Applications," *Sensors*, vol. 9, pp. 2271–2288, mar 2009.
- [100] P. Ripka, "Advances in fluxgate sensors," *Sensors and Actuators A: Physical*, vol. 106, pp. 8–14, sep 2003.
- [101] T. McGuire and R. Potter, "Anisotropic magnetoresistance in ferromagnetic 3d alloys," *IEEE Transactions on Magnetics*, vol. 11, pp. 1018–1038, jul 1975.
- [102] P. Freitas, F. Silva, N. Oliveira, L. Melo, L. Costa, and N. Almeida, "Spin valve sensors," *Sensors and Actuators A: Physical*, vol. 81, pp. 2–8, apr 2000.
- [103] R. S. Popovic, *Hall effect devices*. Institute of Physics Pub, 2004.

- [104] J. S. Moodera, L. R. Kinder, T. M. Wong, and R. Meservey, “Large Magnetoresistance at Room Temperature in Ferromagnetic Thin Film Tunnel Junctions,” *Physical Review Letters*, vol. 74, pp. 3273–3276, apr 1995.
- [105] D. Drung, C. Assmann, J. Beyer, A. Kirste, M. Peters, F. Ruede, and T. Schurig, “Highly Sensitive and Easy-to-Use SQUID Sensors,” *IEEE Transactions on Applied Superconductivity*, vol. 17, pp. 699–704, jun 2007.
- [106] C. D. Gratta, V. Pizzella, F. Tecchio, and G. L. Romani, “Magnetoencephalography - a noninvasive brain imaging method with 1 ms time resolution,” *Reports on Progress in Physics*, vol. 64, pp. 1759–1814, dec 2001.
- [107] R. McDermott, A. H. Trabesinger, M. Muck, E. L. Hahn, A. Pines, and J. Clarke, “Liquid-State NMR and Scalar Couplings in Microtesla Magnetic Fields,” *Science*, vol. 295, pp. 2247–2249, mar 2002.
- [108] D. Robbes, C. Dolabdjian, S. Saez, Y. Monfort, G. Kaiser, and P. Ciureanu, “Highly sensitive uncooled magnetometers: State of the art. Superconducting magnetic hybrid magnetometers, an alternative to SQUIDS?,” *IEEE Transactions on Applied Superconductivity*, vol. 11, pp. 629–634, mar 2001.
- [109] D. Robbes, “Highly sensitive magnetometers—a review,” *Sensors and Actuators A: Physical*, vol. 129, pp. 86–93, may 2006.
- [110] S. Tumanski, “Induction coil sensors—a review,” *Measurement Science and Technology*, vol. 18, pp. R31–R46, mar 2007.
- [111] R. Mach-Batlle, A. Parra, S. Laut, N. Del-Valle, C. Navau, and A. Sanchez, “Magnetic Illusion: Transforming a Magnetic Object into Another Object by Negative Permeability,” *Physical Review Applied*, vol. 9, p. 034007, mar 2018.
- [112] A. Alù and N. Engheta, “Cloaking a Sensor,” *Physical Review Letters*, vol. 102, p. 233901, jun 2009.
- [113] A. Alù and N. Engheta, “Cloaking a receiving antenna or a sensor with plasmonic metamaterials,” *Metamaterials*, vol. 4, pp. 153–159, aug 2010.
- [114] J. C. Soric, R. Fleury, A. Monti, A. Toscano, F. Bilotti, and A. Alu, “Controlling Scattering and Absorption With Metamaterial Covers,” *IEEE Transactions on Antennas and Propagation*, vol. 62, pp. 4220–4229, aug 2014.
- [115] A. Monti, J. Soric, M. Barbuto, D. Ramaccia, S. Vellucci, F. Trotta, A. Alù, A. Toscano, and F. Bilotti, “Mantle cloaking for co-site radio-frequency antennas,” *Applied Physics Letters*, vol. 108, p. 113502, mar 2016.
- [116] A. Greenleaf, Y. Kurylev, M. Lassas, and G. Uhlmann, “Cloaking a sensor via transformation optics,” *Physical Review E*, vol. 83, p. 016603, jan 2011.

- [117] P.-Y. Chen and A. Alù, “Mantle cloaking using thin patterned metasurfaces,” *Physical Review B*, vol. 84, p. 205110, nov 2011.
- [118] X. Zhu, B. Liang, W. Kan, X. Zou, and J. Cheng, “Acoustic Cloaking by a Superlens with Single-Negative Materials,” *Physical Review Letters*, vol. 106, p. 014301, jan 2011.
- [119] R. Fleury, D. Sounas, and A. Alù, “An invisible acoustic sensor based on parity-time symmetry,” *Nature Communications*, vol. 6, p. 5905, dec 2015.
- [120] T. Yang, X. Bai, D. Gao, L. Wu, B. Li, J. T. L. Thong, and C.-W. Qiu, “Invisible Sensors: Simultaneous Sensing and Camouflaging in Multiphysical Fields,” *Advanced Materials*, vol. 27, pp. 7752–7758, dec 2015.
- [121] F. Monticone and A. Alù, “Metamaterial, plasmonic and nanophotonic devices,” *Reports on Progress in Physics*, vol. 80, p. 036401, mar 2017.
- [122] P. Leroy, C. Coillot, V. Mosser, A. Roux, and G. Chanteur, “Use of Magnetic Concentrators to Highly Improve the Sensitivity of Hall Effect Sensors,” *Sensor Letters*, vol. 5, pp. 162–166, mar 2007.
- [123] J. Zhu, W. Jiang, Y. Liu, G. Yin, J. Yuan, S. He, and Y. Ma, “Three-dimensional magnetic cloak working from d.c. to 250 kHz,” *Nature communications*, vol. 6, p. 8931, nov 2015.
- [124] J. Prat-Camps, P. Maurer, G. Kirchmair, and O. Romero-Isart, “Circumventing Magnetostatic Reciprocity: A Diode for Magnetic Fields,” *Physical Review Letters*, vol. 121, p. 213903, nov 2018.
- [125] S. A. Ramakrishna, “Physics of negative refractive index materials,” *Reports on Progress in Physics*, vol. 68, pp. 449–521, feb 2005.
- [126] N. Kaina, F. Lemoult, M. Fink, and G. Lerosey, “Negative refractive index and acoustic superlens from multiple scattering in single negative metamaterials,” *Nature*, vol. 525, pp. 77–81, sep 2015.
- [127] Z. J. Wong, Y. Wang, K. O’Brien, J. Rho, X. Yin, S. Zhang, N. Fang, T.-J. Yen, and X. Zhang, “Optical and acoustic metamaterials: superlens, negative refractive index and invisibility cloak,” *Journal of Optics*, vol. 19, p. 084007, aug 2017.
- [128] T. J. Yen, “Terahertz Magnetic Response from Artificial Materials,” *Science*, vol. 303, pp. 1494–1496, mar 2004.
- [129] J. B. Pendry, A. J. Holden, D. J. Robbins, and W. J. Stewart, “Recent citations Low frequency plasmons in thin-wire structures,” tech. rep., 1998.
- [130] R. A. Shelby, D. R. Smith, and S. Schultz, “Experimental Verification of a Negative Index of Refraction,” *Science*, vol. 292, pp. 77–79, apr 2001.

-
- [131] C. G. Parazzoli, R. B. Gregor, K. Li, B. E. C. Koltenbah, and M. Tanielian, “Experimental Verification and Simulation of Negative Index of Refraction Using Snell’s Law,”
- [132] F. Yang, Z. L. Mei, X. Y. Yang, T. Y. Jin, and T. J. Cui, “A Negative Conductivity Material Makes a dc Invisibility Cloak Hide an Object at a Distance,” *Advanced Functional Materials*, vol. 23, pp. 4306–4310, sep 2013.
- [133] J. Li and C. T. Chan, “Double-negative acoustic metamaterial,” *Physical Review E*, vol. 70, p. 055602, nov 2004.
- [134] Y. Ding, Z. Liu, C. Qiu, and J. Shi, “Metamaterial with Simultaneously Negative Bulk Modulus and Mass Density,” *Physical Review Letters*, vol. 99, p. 093904, aug 2007.
- [135] S. H. Lee, C. M. Park, Y. M. Seo, Z. G. Wang, and C. K. Kim, “Composite Acoustic Medium with Simultaneously Negative Density and Modulus,” *Physical Review Letters*, vol. 104, p. 054301, feb 2010.
- [136] Z. G. Nicolaou and A. E. Motter, “Mechanical metamaterials with negative compressibility transitions,” *Nature Materials*, vol. 11, pp. 608–613, jul 2012.
- [137] J. Qu, A. Gerber, F. Mayer, M. Kadic, and M. Wegener, “Experiments on Metamaterials with Negative Effective Static Compressibility,” *Physical Review X*, vol. 7, p. 041060, dec 2017.
- [138] A. I. Khan, K. Chatterjee, B. Wang, S. Drapcho, L. You, C. Serrao, S. R. Bakaul, R. Ramesh, and S. Salahuddin, “Negative capacitance in a ferroelectric capacitor,” *Nature Materials*, vol. 14, pp. 182–186, feb 2015.
- [139] P. Zubko, J. C. Wojdeł, M. Hadjimichael, S. Fernandez-Pena, A. Sené, I. Luk’yanchuk, J.-M. Triscone, and J. Íñiguez, “Negative capacitance in multidomain ferroelectric superlattices,” *Nature*, vol. 534, pp. 524–528, jun 2016.
- [140] K. Takenaka, “Negative thermal expansion materials: technological key for control of thermal expansion,” *Science and technology of advanced materials*, vol. 13, p. 013001, feb 2012.
- [141] R. Mach-Batlle, A. Parra, J. Prat-Camps, S. Laut, C. Navau, and A. Sanchez, “Negative permeability in magnetostatics and its experimental demonstration,” *Physical Review B*, vol. 96, p. 094422, sep 2017.
- [142] O. Dolgov, D. Kirzhnits, and V. Losyakov, “On the admissible values of the static magnetic permeability,” *Solid State Communications*, vol. 46, pp. 147–149, apr 1983.

- [143] R. Mach-Batlle, A. Parra, S. Laut, C. Navau, N. Del-Valle, and A. Sanchez, “Cloak, anticloak, magnification and illusion in magnetostatics,” in *2017 11th International Congress on Engineered Materials Platforms for Novel Wave Phenomena (Metamaterials)*, pp. 301–303, IEEE, aug 2017.
- [144] C. F. Bohren and D. R. Huffman, eds., *Absorption and Scattering of Light by Small Particles*. Weinheim, Germany: Wiley-VCH Verlag GmbH, apr 1998.
- [145] F. Castles and P. S. Grant, “Active metamaterials with negative static dielectric susceptibility,” apr 2017.
- [146] D. M. Nguyen, H. Xu, Y. Zhang, and B. Zhang, “Active thermal cloak,” *Applied Physics Letters*, vol. 107, p. 121901, sep 2015.
- [147] B.-I. Popa and S. A. Cummer, “Non-reciprocal and highly nonlinear active acoustic metamaterials,” *Nature Communications*, vol. 5, p. 3398, dec 2014.
- [148] J. P. Barrett and S. A. Cummer, “Roadmap to electrically self-tuning metamaterials: Design and experimental validation,” in *2014 International Conference on Electromagnetics in Advanced Applications (ICEAA)*, pp. 341–342, IEEE, aug 2014.
- [149] Q. Ma, F. Yang, T. Y. Jin, Z. L. Mei, and T. J. Cui, “Open active cloaking and illusion devices for the Laplace equation,” *Journal of Optics*, vol. 18, p. 044004, apr 2016.
- [150] A. Greenleaf, Y. Kurylev, M. Lassas, and G. Uhlmann, “Full-Wave Invisibility of Active Devices at All Frequencies,” *Communications in Mathematical Physics*, vol. 275, pp. 749–789, aug 2007.
- [151] Y. Yuan, B.-I. Popa, and S. A. Cummer, “Zero loss magnetic metamaterials using powered active unit cells,” *Optics Express*, vol. 17, p. 16135, aug 2009.
- [152] M. Selvanayagam and G. V. Eleftheriades, “An Active Electromagnetic Cloak Using the Equivalence Principle,” *IEEE Antennas and Wireless Propagation Letters*, vol. 11, pp. 1226–1229, 2012.
- [153] M. Selvanayagam and G. V. Eleftheriades, “Experimental Demonstration of Active Electromagnetic Cloaking,” *Physical Review X*, vol. 3, p. 041011, nov 2013.
- [154] P.-Y. Chen, J. Soric, and A. Alù, “Invisibility and Cloaking Based on Scattering Cancellation,” *Advanced Materials*, vol. 24, pp. OP281–OP304, nov 2012.
- [155] N. Xiang, Q. Cheng, H. B. Chen, J. Zhao, W. X. Jiang, H. F. Ma, and T. J. Cui, “Bifunctional metasurface for electromagnetic cloaking and illusion,” *Applied Physics Express*, vol. 8, p. 092601, sep 2015.

- [156] S. Vellucci, A. Monti, A. Toscano, and F. Bilotti, “Scattering Manipulation and Camouflage of Electrically Small Objects through Metasurfaces,” *Physical Review Applied*, vol. 7, p. 034032, mar 2017.
- [157] C. Li, X. Meng, X. Liu, F. Li, G. Fang, H. Chen, and C. T. Chan, “Experimental Realization of a Circuit-Based Broadband Illusion-Optics Analogue,” *Physical Review Letters*, vol. 105, p. 233906, dec 2010.
- [158] W. X. Jiang and T. J. Cui, “Radar illusion via metamaterials,” *Physical Review E*, vol. 83, p. 026601, feb 2011.
- [159] Q. Ma, Z. L. Mei, S. K. Zhu, T. Y. Jin, and T. J. Cui, “Experiments on Active Cloaking and Illusion for Laplace Equation,” *Physical Review Letters*, vol. 111, p. 173901, oct 2013.
- [160] X. He and L. Wu, “Illusion thermodynamics: A camouflage technique changing an object into another one with arbitrary cross section,” *Applied Physics Letters*, vol. 105, p. 221904, dec 2014.
- [161] F. Sun and S. He, “Transformation magneto-statics and illusions for magnets,” *Scientific Reports*, vol. 4, p. 6593, may 2015.
- [162] W. Jiang, Y. Ma, and S. He, “Static Magnetic Cloak without a Superconductor,” *Physical Review Applied*, vol. 9, p. 054041, may 2018.
- [163] D. A. B. Miller, “On perfect cloaking,” *Optics Express*, vol. 14, p. 12457, dec 2006.
- [164] R. A. Shelby, D. R. Smith, and S. Schultz, “Experimental verification of a negative index of refraction,” *Science (New York, N.Y.)*, vol. 292, pp. 77–9, apr 2001.
- [165] S. A. Ramakrishna, J. B. Pendry, D. Schurig, D. R. Smith, and S. Schultz, “The asymmetric lossy near-perfect lens,” *Journal of Modern Optics*, vol. 49, pp. 1747–1762, aug 2002.
- [166] J. B. Pendry and S. A. Ramakrishna, “Focusing light using negative refraction,” *Journal of Physics: Condensed Matter*, vol. 15, pp. 6345–6364, sep 2003.
- [167] J. B. Pendry and S. A. Ramakrishna, “Near-field lenses in two dimensions,” *Journal of Physics: Condensed Matter*, vol. 14, pp. 8463–8479, sep 2002.
- [168] J. Pendry, “Perfect cylindrical lenses,” *Optics Express*, vol. 11, p. 755, apr 2003.
- [169] S. Anantha Ramakrishna and J. B. Pendry, “Spherical perfect lens: Solutions of Maxwell’s equations for spherical geometry,” *Physical Review B*, vol. 69, p. 115115, mar 2004.

- [170] A. Grbic and G. V. Eleftheriades, “Overcoming the Diffraction Limit with a Planar Left-Handed Transmission-Line Lens,” *Physical Review Letters*, vol. 92, p. 117403, mar 2004.
- [171] N. Fang, H. Lee, C. Sun, and X. Zhang, “Sub-Diffraction-Limited Optical Imaging with a Silver Superlens,” *Science*, vol. 308, pp. 534–537, apr 2005.
- [172] Z. Liu, H. Lee, Y. Xiong, C. Sun, and X. Zhang, “Far-Field Optical Hyperlens Magnifying Sub-Diffraction-Limited Objects,” *Science*, vol. 315, pp. 1686–1686, mar 2007.
- [173] I. I. Smolyaninov, Y.-J. Hung, and C. C. Davis, “Magnifying Superlens in the Visible Frequency Range,” *Science*, vol. 315, pp. 1699–1701, mar 2007.
- [174] R. Merlin, “Radiationless Electromagnetic Interference: Evanescent-Field Lenses and Perfect Focusing,” *Science*, vol. 317, pp. 927–929, aug 2007.
- [175] V. V. Cheianov, V. Fal’ko, and B. L. Altshuler, “The focusing of electron flow and a Veselago lens in graphene p-n junctions.,” *Science (New York, N.Y.)*, vol. 315, pp. 1252–5, mar 2007.
- [176] M. Tsang and D. Psaltis, “Magnifying perfect lens and superlens design by coordinate transformation,” *Physical Review B*, vol. 77, p. 035122, jan 2008.
- [177] M. Yan, W. Yan, and M. Qiu, “Cylindrical superlens by a coordinate transformation,” *Physical Review B*, vol. 78, p. 125113, sep 2008.
- [178] Q.-G. Lin, “Theoretical development of the image method for a general magnetic source in the presence of a superconducting sphere or a long superconducting cylinder,” *Physical Review B*, vol. 74, p. 024510, jul 2006.
- [179] L. Bergamin and A. Favaro, “Negative index of refraction, perfect lenses and transformation optics - some words of caution.,” in *2010 URSI International Symposium on Electromagnetic Theory*, pp. 760–763, IEEE, aug 2010.
- [180] N. A. Nicorovici, R. C. McPhedran, and G. W. Milton, “Optical and dielectric properties of partially resonant composites,” *Physical Review B*, vol. 49, pp. 8479–8482, mar 1994.
- [181] G. W. Milton, N.-A. P. Nicorovici, R. C. McPhedran, and V. A. Podolskiy, “A proof of superlensing in the quasistatic regime, and limitations of superlenses in this regime due to anomalous localized resonance,” *Proceedings of the Royal Society A: Mathematical, Physical and Engineering Sciences*, vol. 461, pp. 3999–4034, dec 2005.
- [182] G. W. Milton, N.-A. P. Nicorovici, R. C. McPhedran, K. Cherednichenko, and Z. Jacob, “Solutions in folded geometries, and associated cloaking due to anomalous resonance,” *New Journal of Physics*, vol. 10, p. 115021, nov 2008.

-
- [183] R. Fleury, D. L. Sounas, and A. Alù, “Negative Refraction and Planar Focusing Based on Parity-Time Symmetric Metasurfaces,” *Physical Review Letters*, vol. 113, p. 023903, jul 2014.
- [184] F. Monticone, C. A. Valagiannopoulos, and A. Alu, “Parity-Time Symmetric Nonlocal Metasurfaces: All-Angle Negative Refraction and Volumetric Imaging,” *Physical Review X*, vol. 6, p. 041018, oct 2016.
- [185] H. Chen and C. T. Chan, ““Cloaking at a distance” from folded geometries in bipolar coordinates,” *Optics Letters*, vol. 34, p. 2649, sep 2009.
- [186] F. G. Vasquez, G. W. Milton, and D. Onofrei, “Active Exterior Cloaking for the 2D Laplace and Helmholtz Equations,” *Physical Review Letters*, vol. 103, p. 073901, aug 2009.
- [187] Y. Lai, H. Chen, Z.-Q. Zhang, and C. T. Chan, “Complementary Media Invisibility Cloak that Cloaks Objects at a Distance Outside the Cloaking Shell,” *Physical Review Letters*, vol. 102, p. 093901, mar 2009.

List of publications by Rosa Mach-Batlle

1. C. Navau, R. Mach-Batlle, A. Parra, J. Prat-Camps, S. Laut, N. Del-Valle, and A. Sanchez
"Enhancing the sensitivity of magnetic sensors by 3D metamaterial shells", *Scientific Reports* **7**, 44762 (2017).
2. R. Mach-Batlle, A. Parra, J. Prat-Camps, S. Laut, C. Navau, and A. Sanchez
"Negative permeability in magnetostatics and its experimental demonstration", *Physical Review B* **96**, 094422 (2017).
3. R. Mach-Batlle, A. Parra, S. Laut, C. Navau, N. Del-Valle and A. Sanchez,
"Cloak, anticloak, magnification and illusion in magnetostatics", 2017 11th International Congress on Engineered Materials Platforms for Novel Wave Phenomena (Metamaterials), Marseille, 2017, pp. 301-303.
4. R. Mach-Batlle, A. Parra, S. Laut, N. Del-Valle, C. Navau, and A. Sanchez
"Magnetic illusion: transforming a magnetic object into another object by negative permeability", *Physical Review Applied* **9**, 034007 (2018).
5. R. Mach-Batlle, C. Navau, and A. Sanchez
"Invisible magnetic sensors", *Applied Physics Letters* **112**, 162406 (2018).
6. S. Laut, R. Mach-Batlle, C. Navau, and A. Sanchez
"Single-layer quasistatic magnetic cloak at aimed wave phases", *In preparation*.
7. R. Mach-Batlle, M. Bason, N. Del-Valle, J. Prat-Camps
"Deep focusing of magnetic fields with negative permeability", *In preparation*.